

THE SOLUTION FOR THE PROPAGATION  
OF SOUND IN CYLINDRICAL TUBES  
AND TOROIDAL WAVEGUIDES  
WITH DRIVEN WALLS

FINAL REPORT

The Jamie Whitten  
National Center for  
Physical Acoustics



*The*  
*University of Mississippi*

DISTRIBUTION STATEMENT A

Approved for public release;  
Distribution Unlimited

DTIC QUALITY INSPECTED

**THE SOLUTION FOR THE PROPAGATION  
OF SOUND IN CYLINDRICAL TUBES  
AND TOROIDAL WAVEGUIDES  
WITH DRIVEN WALLS**

**FINAL REPORT**

**for**

**CONTRACT #N00014-90-J-4068**

Submitted to:

Phillip Abraham ONR 1132SM  
Office of Naval Research  
800 North Quincy Street  
Arlington, VA 22217-5660

Submitted by:

Christopher C. Lawrenson and F. Douglas Shields  
National Center for Physical Acoustics  
The University of Mississippi  
University, Mississippi 38677

NCPA Internal Tracking Number: DS0396-01

March 1996

DISTRIBUTION STATEMENT A

Approved for public release;  
Distribution Unlimited

19960326 084

# REPORT DOCUMENTATION PAGE

*Form Approved  
OMB No. 0704-0188*

Public reporting burden for this collection of information is estimated to average 1 hour per response, including the time for reviewing instructions, searching existing data sources, gathering and maintaining the data needed, and completing and reviewing the collection of information. Send comments regarding this burden estimate or any other aspect of this collection of information, including suggestions for reducing this burden, to Washington Headquarters Services, Directorate for Information Operations and Reports, 1215 Jefferson Davis Highway, Suite 1204, Arlington, VA 22202-4302, and to the Office of Management and Budget, Paperwork Reduction Project (0704-0188), Washington, DC 20503.

1. AGENCY USE ONLY (Leave blank)	2. REPORT DATE	3. REPORT TYPE AND DATES COVERED	
	18 Mar 1996	Final 01 Jul 92 - 29 Sept 95	
4. TITLE AND SUBTITLE  The Solution for the Propagation of Sound in Cylindrical Tubes and Toroidal Waveguides with Driven Walls			5. FUNDING NUMBERS  PE 61153N G N00014-90-J-4068 TA 4324851 04/05
6. AUTHOR(S)  Christopher C. Lawrenson and F. Douglas Shields			
7. PERFORMING ORGANIZATION NAME(S) AND ADDRESS(ES)  University of Mississippi National Center for Physical Acoustics University, MS 38677			8. PERFORMING ORGANIZATION REPORT NUMBER  DS0396-1
9. SPONSORING/MONITORING AGENCY NAME(S) AND ADDRESS(ES)  Phillip Abraham ONR 1132SM Office of Naval Research 800 North Quincy Street Arlington, VA 22217-5660			10. SPONSORING/MONITORING AGENCY REPORT NUMBER
11. SUPPLEMENTARY NOTES  Ph.D. dissertation of Christopher C. Lawrenson			
12a. DISTRIBUTION/AVAILABILITY STATEMENT  Approved for public release: Distribution unlimited		12b. DISTRIBUTION CODE	
13. ABSTRACT (Maximum 200 words)  Our EPSCoR grant was used to support Mr. Christopher Lawrenson in his doctoral research. A copy of his dissertation is enclosed. Mr. Lawrenson presented a paper on his work at the 1994 meeting of the Acoustical Society of America, for which he received a financial award for the best student paper in engineering acoustics. Mr. Lawrenson was also awarded a scholarship to the Physical Acoustics Summer School which is sponsored by ONR in the summer of 1994. He has written a paper on his dissertation work that has been accepted for publication in the Journal of the Acoustical Society of America.  Dr. Lawrenson is now employed by the Macrosonuxs Company of Richmond, Virginia.			
14. SUBJECT TERMS  Propagation of sound, driven walls, lossless fluid, viscous and thermally conducting fluid			15. NUMBER OF PAGES  200
			16. PRICE CODE
17. SECURITY CLASSIFICATION OF REPORT  UNCLASSIFIED	18. SECURITY CLASSIFICATION OF THIS PAGE  UNCLASSIFIED	19. SECURITY CLASSIFICATION OF ABSTRACT  UNCLASSIFIED	20. LIMITATION OF ABSTRACT

THE SOLUTION FOR THE PROPAGATION OF SOUND  
IN CYLINDRICAL TUBES AND TOROIDAL WAVEGUIDES  
WITH DRIVEN WALLS

A Dissertation  
Presented for the  
Doctor of Philosophy  
Degree  
The University of Mississippi

Christopher C. Lawrenson  
December, 1994

Copyright © **Christopher C. Lawrenson**, 1994  
All rights reserved

## DEDICATION

This dissertation is dedicated to my wife

Leigh

# Acknowledgements

I would like to acknowledge those whose help made this work possible. I wish to thank Dr. Doug Shields who patiently guided me along the way like a parent teaching his child to walk. I am grateful to Dr. Dwynn Lafleur for his informative discussions and willingness to explain simple concepts over and over until I finally understood. Many thanks go to Frank Lacy, whose amazing understanding of electronics still leaves me speechless. Thanks also go to Sean Cordry for the many years of friendship and study-sessions; Keith Olree for listening; Matt Miley for his innovative ideas; my predecessors, Tim Ruppel and Daniel Warren, for being there before me; Jeff Schindall, Carl Frederickson, Jim Belcher, Jay Lightfoot, Ken Markewicz, David Craig, and Chris Hobbs, for their friendship; Robin Cleveland for the great discussions at PASS-94; the MiFFL gang for the wonderful distraction.

I wish to extend my gratitude to the National Center for Physical Acoustics for allowing me the opportunity to practice my trade, and to the Office of Naval Research for the EPSCoR grant which funded this work.

I wish to thank my parents for their support and friendship (this time I'm first, Dad!). I am grateful to my son, Michael, who always seems to show me that you do not have to know a lot to be smart. Most of all, I wish to thank my wife, Leigh.

## ABSTRACT

This dissertation is a theoretical and experimental study of sound in tubes with driven (or active) walls. Two geometries are considered: (1) a cylindrical tube of infinite length, and (2) a toroidal waveguide.

For sound propagation in the first geometry, two cases are theoretically considered. The first case is that of a lossless fluid, and the second is a viscous and thermally conducting fluid. The derivation of the latter case closely follows Lord Rayleigh's derivation of sound propagation in a rigid tube. Theoretical results for the particle velocity components of both cases are presented along with the three modes of propagation found in the second case.

For sound propagation in the second geometry, the cases of rigid and driven wall toroids with lossless fluids are presented, along with methods for including losses in the system. Theoretical results for the pressure inside the toroid with various driving conditions and parameters are shown.

Experimental measurements of the sound pressure levels in a toroid are presented and compared to theoretical results. To make some of these measurements, it was necessary to develop a device we are calling an *acoustitron*. Results show that the physical system is well represented by the theory presented in this work.

# Contents

<b>Introduction</b>	<b>1</b>
<b>1 Theory of the Straight Tube</b>	<b>8</b>
1.1 The Wave Equation . . . . .	9
1.2 A Lossless Fluid Filled Tube with Driven Walls . . . . .	11
1.2.1 Theory . . . . .	11
1.2.2 Results . . . . .	13
1.3 Viscid and Thermally Conducting Fluid Filled Tube with Driven Walls	22
1.3.1 Derivation of the General Equation . . . . .	22
1.3.2 Solution for the Temperature Equation . . . . .	27
1.3.3 Solution for the Velocity Equation . . . . .	29
1.3.4 Application of the Driven Wall Boundary Condition . . . . .	33
1.3.5 Theoretical Results for an Air Filled Tube . . . . .	39
1.4 Chapter Summary . . . . .	57
<b>2 Theory of the Toroidal Waveguide</b>	<b>58</b>
2.1 General Theory for the Lossless Toroid . . . . .	60

3.3.3	Pressure Distribution in the Acoustitron with a Delta Function	
Driver	.....	119
3.3.4	Sound Pressure Measurements Inside the Acoustitron	122
3.3.5	Traveling Waves in the Acoustitron	148
<b>4</b>	<b>Conclusions</b>	<b>153</b>
4.0.6	Summary	153
4.0.7	Extensions of this Work	155
<b>Bibliography</b>		<b>156</b>
<b>A</b>	<b>Useful Relations of State Variables</b>	<b>162</b>
<b>B</b>	<b>Digital Delay Circuit Diagrams</b>	<b>164</b>
<b>C</b>	<b>Software and Hardware Information</b>	<b>169</b>
<b>Vita</b>		<b>171</b>

# List of Tables

0.1	Papers on straight tubes with rectangular cross-sections . . . . .	5
0.2	Papers on straight tubes with circular cross-sections . . . . .	6
0.3	Papers on curved tubes with rectangular and circular cross-sections .	7
1.1	Thermal properties are for air at 27°C at atmospheric pressure. ( <i>Source:</i> "Table of Thermal Properties of Gases," National Bureau of Standards Circular 564, Issue Date: November 1, 1955.) . . . . .	39
1.2	Outline of velocity amplitude figures. . . . .	40
3.1	Dimensions and configuration of the acoustitron. . . . .	97
3.2	Piezoelectric properties of EDO Corporation EC-70 piezoelectric driving element, equivalent to DOD-STD-1376A(SH) Type V. Note that the values given are nominal; actual production values vary $\pm 10\%$ . ( <i>Source:</i> EDO Corporation, Acoustics Division, Salt Lake City, Utah.)	99
3.3	Experimentally determined parameters from measurements made on both the acoustitron (Tygon®) and PVC torus, along with manufacturers information. The value for attenuation measured at the resonance frequency given in the table excludes the tube effect. . . . .	117

# List of Figures

0.1 Simple design for a tube with active walls. In this example, three driving elements are attached to a short section of tube of radius $a$ .	3
1.1 The cylindrical tube.	12
1.2 Normalized axial velocity amplitude for a lossless fluid filled tube as a function of the dimensionless wave number $ka$ and propagation speed $c_w/c$ . Plot made for $r = a/2$ .	14
1.3 Normalized radial velocity amplitude for a lossless fluid filled tube as a function of the dimensionless wave number $ka$ and propagation speed $c_w/c$ . Plot made for $r = a/2$ .	15
1.4 Normalized axial velocity amplitude for a lossless fluid filled tube as a function of the dimensionless radial position $r/a$ and propagation speed $c_w/c$ . Plot made for $ka = 1$ .	18
1.5 Normalized axial velocity amplitude for a lossless fluid filled tube as a function of the dimensionless radial position $r/a$ and propagation speed $c_w/c$ . Plot made for $ka = 8$ .	19

1.6 Normalized radial velocity amplitude for a lossless fluid filled tube as a function of the dimensionless radial position and propagation speed $c_w/c$ . Plot made for $ka = 1$ .	20
1.7 Normalized radial velocity amplitude for a lossless fluid filled tube as a function of the dimensionless radial position and propagation speed $c_w/c$ . Plot made for $ka = 8$ .	21
1.8 Normalized radial velocity amplitude as a function of the dimensionless wave number $ka$ and propagation speed $c_w/c$ in an air filled tube. Plot made for $r = a/2$ .	42
1.9 Normalized axial velocity amplitude as a function of the dimensionless wave number $ka$ and propagation speed $c_w/c$ in an air filled tube. Plot made for $r = a/2$ .	43
1.10 Plot of the magnitude $D$ given by Eq. (1.86) for $c_w = c$ in an air filled tube.	44
1.11 Normalized acoustic mode radial velocity amplitude for tube filled with various types of fluid. Plot made for $ka = 1$ and $r = a/2$ .	45
1.12 Normalized acoustic mode radial velocity amplitude for tube filled with various types of fluid. Plot made for $ka = 1$ and $r = a/2$ .	46
1.13 Normalized radial velocity amplitude of the acoustic mode as a function of the dimensionless radial position $r/a$ and propagation speed $c_w/c$ in an air filled tube. Plot made for $ka = 1$ . Note that at $c_w = c$ the amplitude of motion is zero for all values of $r \leq a$ .	47

1.14 Normalized radial velocity amplitude of the vorticity mode as a function of the dimensionless radial position $r/a$ and propagation speed $c_w/c$ in an air filled tube. Plot made for $ka = 1$ . . . . .	48
1.15 Normalized radial velocity amplitude of the entropy mode as a function of the dimensionless radial position $r/a$ and propagation speed $c_w/c$ in an air filled tube. Plot made for $ka = 1$ . . . . .	49
1.16 Normalized total radial velocity amplitude as a function of the dimensionless radial position $r/a$ and propagation speed $c_w/c$ in an air filled tube. Plot made for $ka = 1$ . Note that for $c_w = c$ the amplitude at the wall is such that $ v/V_0  = 1$ as required by the boundary condition. . . . .	50
1.17 Normalized total radial velocity amplitude as a function of the dimensionless radial position $r/a$ and propagation speed $c_w/c$ in an air filled tube. Plot made for $ka = 8$ . . . . .	51
1.18 Normalized axial velocity amplitude of the acoustic mode as a function of the dimensionless radial position $r/a$ and propagation speed $c_w/c$ in an air filled tube. Plot made for $ka = 1$ . . . . .	52
1.19 Normalized axial velocity amplitude of the vorticity mode as a function of the dimensionless radial position $r/a$ and propagation speed $c_w/c$ in an air filled tube. Plot made for $ka = 1$ . . . . .	53
1.20 Normalized axial velocity amplitude of the entropy mode as a function of the dimensionless radial position $r/a$ and propagation speed $c_w/c$ in an air filled tube. Plot made for $ka = 1$ . . . . .	54

1.21 Normalized total axial velocity amplitude as a function of the dimensionless radial position $r/a$ and propagation speed $c_w/c$ in an air filled tube. Plot made for $ka = 1$ .	55
1.22 Normalized total axial velocity amplitude as a function of the dimensionless radial position $r/a$ and propagation speed $c_w/c$ in an air filled tube. Plot made for $ka = 1$ .	56
2.1 The Toroidal Waveguide.	59
2.2 Toroid with inner and outer driven walls and upper and lower rigid walls.	65
2.3 Theoretical complex pressure inside a toroid as a function of angular position driven with a single driving element. The driving element is located at $\theta = 0$ . The driving frequency differs from the first characteristic frequency by 0.07%. Only the first thirty terms in the sum have been used.	71
2.4 Theoretical complex pressure inside a toroid as a function of angular position driven with a single driving element. The driving element is located at $\theta = 0$ . The driving frequency differs from the second characteristic frequency by 0.07%. Only the first thirty terms in the sum have been used.	72
2.5 Theoretical complex pressure inside a toroid as a function of angular position driven with a single driving element. The driving element is located at $\theta = 0$ . The driving frequency is halfway between the first and second characteristic frequency. Only the first thirty terms in the sum have been used.	73

2.6 Theoretical complex pressure inside a toroid as a function of angular position driven with a single driving element. The driving element is located at $\theta = 0$ . The driving frequency is a quarter of the way between the first and the second characteristic frequency. Only the first thirty terms in the sum have been used. . . . .	74
2.7 Sound pressure amplitude inside a toroid as a function of frequency for various values of $\Omega \geq 1$ at $\theta = 0$ . Values of $m$ used range from -30 to 30. . . . .	80
2.8 Sound pressure amplitude inside a toroid as a function of frequency for various values of $\Omega \leq 1$ at $\theta = 0$ . Values of $m$ used range from -30 to 30. . . . .	81
2.9 Theoretical values of the magnitude of the pressure at $\theta = -3.30, -1.73, 0.16$ , and $1.41$ radians. The frequencies at the circled intersections are those for the case of $\Omega/\Omega_0 = 0.9$ that yield traveling waves. . . . .	82
2.10 Elastic tube considered in derivation of absorption coefficient. The figure on the left is the open section of tube shown on the right. Vectors are shown indicating the direction of the elastic force ( $F_e$ ) and the force due to the pressure ( $F_p$ ) are shown. . . . .	91
3.1 The acoustitron. . . . .	98

3.2 Diagram of the digital delay circuit used to drive the acoustitron. The user can control the time delay between successive outputs, as well as which output is the first in the output sequence. In general, there will be a discontinuity between the first and last outputs of the circuit which will fix the position of the microphone to a specific position in the acoustitron. By allowing the user to vary the location of the "break" in the driving wall, the microphone can be "moved" around the tube to any of thirty-two "positions" . . . . .	100
3.3 Flowchart of computer programs used to operate the DSP. . . . .	103
3.4 The toroidal coordinate system. . . . .	104
3.5 Location of four positions from which velocity amplitude measurements were taken using the LDV. Position A was the driving element. . . . .	108
3.6 Velocity amplitude of driver and wall measured at four different positions. Data was taken with a 1 volt driving signal. . . . .	109
3.7 Displacement of driver and wall measured at four different positions. The theoretical displacement of the driving element based on piezoelectric properties is also shown. Data was taken with a 1 volt driving signal. . . . .	111

3.8 Examples of decay measured for the case of (a) a traveling wave in the acoustitron and (b) a standing wave produced by a single driving element. For the standing wave case, the driving frequency was twelve times the fundamental frequency and the microphone was located approximately opposite the driving element. Therefore the number of cycles in the first step is about six, and the remainder of the steps is exactly twelve. The driving frequency used in both cases was about 3900 Hz. . . . . 114

3.9 Measured values of absorption coefficient in the acoustitron along with theoretical curves from Eq. (2.102) based on the measured value of absorption at the resonance frequency. The frequencies plotted as circles correspond to traveling waves inside the acoustitron. Standing wave values are plotted as squares. . . . . 115

3.10 Measured values of absorption coefficient in the PVC torus along with theoretical curves from Eq. (2.102) based on the measured value of absorption at the resonance frequency. The frequencies plotted as circles correspond to characteristic frequencies. . . . . 116

3.11 Displacement of a driving element (square markers) and the tube wall (circular markers) while driving the acoustitron at traveling wave frequencies. The measured microphone voltage (diamond markers) is also shown. The resonance in the motion of the tube wall is indicated by the arrow. . . . . 118

3.12 Normalized microphone voltage levels for driver element positions ranging from  $-\pi \leq \phi \leq 0$ ; the normalized data point is indicated by the square marker. The solid curve is that given by Eq. (2.45). The microphone was located at  $\phi = 0$ , and data points were spaced in increments of  $10^\circ$ . The driving frequency was 841.5 Hz. . . . . 120

3.13 Normalized microphone voltage levels for driver element positions ranging from  $-\pi \leq \phi \leq 0$ ; the normalized data point is indicated by the square marker. The solid curve is that given by Eq. (2.45). The microphone was located at  $\phi = 0$ , and data points were spaced in increments of  $10^\circ$ . The driving frequency was 1122.0 Hz. . . . . 121

3.14 Measured values of the sound pressure levels inside the acoustitron for values of  $\Omega/\Omega_0 \geq 1.0$ . The driving voltage was 16.72 volts rms. . . . . 123

3.15 Measured values of the sound pressure levels inside the acoustitron for values of  $\Omega/\Omega_0 \leq 1.0$ . The driving voltage was 16.72 volts rms. . . . . 124

3.16 Comparison of theoretical and experimental values of the normalized sound pressure amplitude in the acoustitron as a function of frequency for  $\Omega/\Omega_0 = 0.75$ . The normalization pressure is that for  $\Omega = \Omega_0$ . . . . . 126

3.17 Comparison of theoretical and experimental values of the normalized sound pressure amplitude in the acoustitron as a function of frequency for  $\Omega/\Omega_0 = 0.80$ . The normalization pressure is that for  $\Omega = \Omega_0$ . . . . . 127

3.18 Comparison of theoretical and experimental values of the normalized sound pressure amplitude in the acoustitron as a function of frequency for  $\Omega/\Omega_0 = 0.85$ . The normalization pressure is that for  $\Omega = \Omega_0$ . . . . . 128



3.27 Comparison of predicted to measured values of the sound pressure level inside the acoustitron for $\Omega/\Omega_0 = 0.80$ . . . . .	138
3.28 Comparison of predicted to measured values of the sound pressure level inside the acoustitron for $\Omega/\Omega_0 = 0.85$ . . . . .	139
3.29 Comparison of predicted to measured values of the sound pressure level inside the acoustitron for $\Omega/\Omega_0 = 0.90$ . . . . .	140
3.30 Comparison of predicted to measured values of the sound pressure level inside the acoustitron for $\Omega/\Omega_0 = 0.95$ . . . . .	141
3.31 Comparison of predicted to measured values of the sound pressure level inside the acoustitron for $\Omega/\Omega_0 = 1.00$ . . . . .	142
3.32 Comparison of predicted to measured values of the sound pressure level inside the acoustitron for $\Omega/\Omega_0 = 1.05$ . . . . .	143
3.33 Comparison of predicted to measured values of the sound pressure level inside the acoustitron for $\Omega/\Omega_0 = 1.10$ . . . . .	144
3.34 Comparison of predicted to measured values of the sound pressure level inside the acoustitron for $\Omega/\Omega_0 = 1.15$ . . . . .	145
3.35 Comparison of predicted to measured values of the sound pressure level inside the acoustitron for $\Omega/\Omega_0 = 1.20$ . . . . .	146
3.36 Comparison of predicted to measured values of the sound pressure level inside the acoustitron for $\Omega/\Omega_0 = 1.25$ . . . . .	147

3.37 Theoretical comparison of the complex pressure at two arbitrary positions (labeled A and B) inside the acoustitron. The graph shows the magnitude $ p $ and the phase difference $\Delta\varphi_{trvl}$ of the pressure at both positions as functions of angular phase velocity. The line labeled as $\Delta\varphi_{trvl}$ is the phase difference corresponding to the propagation time determined by $\Omega$ . The values of $\Omega/\Omega_0$ that yield traveling waves are indicated by circles. . . . .	150
3.38 Experimental values of the magnitude of the pressure at four different positions inside the acoustitron. The frequencies that yield traveling waves are indicated by circles, where $\Omega/\Omega_0 = 0.9$ . . . . .	151
3.39 Comparison of theoretical (solid lines) and experimental (empty circles) results for combinations of frequency and angular phase velocity that yield traveling waves in the acoustitron. . . . .	152
B.1 Analog-to-digital circuit. . . . .	165
B.2 Main circuit. . . . .	166
B.3 Digital-to-analog circuit. . . . .	167
B.4 Amplifier circuit. . . . .	168

# List of Symbols

---

<i>Symbol</i>	<i>Meaning</i>
'	Denotes the homogeneous part of the solution
"	Denotes the particular part of the solution
$A$	Area of cross-section
$A_0$	Coefficient for the vorticity mode
$A_1$	Coefficient for the acoustic mode
$A_2$	Coefficient for the entropy mode
$A_l$	Coefficient for the Fourier sum of the driven wall boundary
$A_m$	Coefficient for $\Phi$ for a given angular wave number
$A_r$	Coefficient for the radial solution of $\Phi$
$A_z$	Coefficient for the axial solution of $\Phi$
$A_\theta$	Coefficient for the azimuthal solution of $\Phi$
$a$	Radius of the cylindrical tube
	Inside radius of the toroidal waveguide
$a'$	Radius of cylindrical tube measured to the midpoint of the wall

$B_1$	Coefficient for the particular solution of the velocity (acoustic mode)
$B_2$	Coefficient for the particular solution of the velocity (entropy mode)
$B_m$	Coefficient for $\Phi$ for a given angular wave number
$B_r$	Coefficient for the radial solution of $\Phi$
$B_z$	Coefficient for the axial solution of $\Phi$
$B_\theta$	Coefficient for the azimuthal solution of $\Phi$
$b$	Outside radius of the toroidal waveguide
$C_0$	Coefficient for the vorticity mode
$C_1$	Coefficient for the acoustic mode
$C_2$	Coefficient for the entropy mode
$C_p$	Specific heat at constant pressure
$c_T$	Isothermal speed of sound
$C_v$	Specific heat at constant volume
$c$	Intrinsic speed of sound in the bulk medium
$\bar{c}$	Complex speed of sound
$c_w$	Speed at which the wave propagates in the driven wall
$d_{31}$	Ratio of strain and applied field in the axial direction
$d_{33}$	Ratio of strain and applied field in the radial direction
$D$	Dimensionless function, defined by Eq. (1.86)
	Displacement of tube
$D_s$	Static displacement of driving element
$F_e$	Force due to stretching of elastic walls
$F_s$	Force due to sound pressure

$f$	Frequency
$f(\theta)$	Function describing the angular dependence of the driving wall
$h$	Height of toroidal duct
$i$	$\sqrt{-1}$
$\text{Im}()$	Imaginary part of the bracketed term
$J_m$	Bessel function of order $m$
$J'_m$	First derivative with respect to $r$ of the Bessel function of order $m$
$J''_m$	Second derivative with respect to $r$ of the Bessel function of order $m$
$J'''_m$	Third derivative with respect to $r$ of the Bessel function of order $m$
$k$	Wave number in the fluid
	Force constant
$\bar{k}$	Complex wave number in the fluid
$k_z$	Axial wave number in the fluid
$k_r$	Radial wave number in the fluid
$k_w$	Wave number of the driven wall
$LDV$	Laser Doppler Vibrometer
$l_e$	Entropy skin depth
$l_v$	Vorticity skin depth
$m$	Variable, used in Chapter 1
	Angular wave number (an integer), used in Chapter 2
$n$	Integer
$\mathcal{P}$	Complex pressure function, defined by Eq. (1.31)
$p$	Pressure

	Integer, used in Section 2.1.1
$p_e$	Pressure due to elastic force
$Q_0$	Function corresponding to the vorticity mode
$Q_1$	Function corresponding to the acoustic mode
$Q_2$	Function corresponding to the entropy mode
$r$	Radial coordinate
$\Delta r$	Change in radius
$\text{Re}()$	Real part of bracketed term
$S$	Perimeter length of cross-section
$s$	Entropy per unit mass
SPL	Sound pressure level
$T$	Temperature, used in Chapter 1 Thickness, used in Section 2.4.2
$\mathcal{T}$	Dimensionless temperature term, defined by Eq. (1.38)
$T_0$	Ambient temperature
$t$	Time
$U$	Potential energy
$\mathbf{u}$	Velocity vector
$V$	Voltage amplitude
$V_0$	Velocity amplitude of the driven wall
$v$	Radial component of velocity
$w$	Axial component of velocity
$x$	Length

$\bar{x}$	Complex variable
$\Delta x$	Change in length
$Y$	Young's modulus
$Y_m$	Neumann function of order $m$
$Y'_m$	First derivative with respect to $r$ of the Neumann function of order $m$
$Y''_m$	Second derivative with respect to $r$ of the Neumann function of order $m$
$Y'''_m$	Third derivative with respect to $r$ of the Neumann function of order $m$
$Z$	Impedance
$z$	Axial coordinate

### Greek

$\alpha$	Coefficient of expansion
	Absorption coefficient
$\alpha_{\text{CW}}$	Absorption coefficient in tube due to compliant wall
$\alpha_{\text{CW}}^R$	Measured absorption coefficient at the resonant frequency (excluding $\alpha_w$ )
$\alpha_w$	Absorption coefficient in tube due to thermoviscous effects at the wall
$\beta$	Variable, defined by Eq. (2.9)
$\gamma$	Ratio of specific heats
$\Delta_m$	Function, defined by Eq. (2.40)
$\delta$	Delta function
$\epsilon$	Constant equal to difference of the ratio of outside to inside radius of a toroid and unity
$\zeta_1$	Coefficient for the acoustic mode

$\zeta_2$	Coefficient for the entropy mode
$\theta$	Angular coordinate
$\kappa$	Thermal conductivity
$\lambda_1$	Characteristic root corresponding to the acoustic mode
$\lambda_2$	Characteristic root corresponding to the entropy mode
$\mu$	Viscosity
$\xi_0$	Coefficient for the vorticity mode
$\xi_1$	Coefficient for the acoustic mode
$\xi_2$	Coefficient for the entropy mode
$\pi$	Pi
$\rho$	Density
$\rho_0$	Ambient density
$\rho_w$	Density of tube wall
$\sigma$	Condensation
$\Phi$	Velocity potential
$\Omega$	Angular phase velocity
$\Omega_0$	Angular phase velocity corresponding to $c$ in the fluid
$\omega$	Angular frequency
$\omega_0$	Resonant angular frequency

# Introduction

The propagation of sound in tubes and ducts has been so thoroughly studied that one might think that all the problems of importance have been solved. This, however, is not the case. These studies, like many in other fields of physics, have been limited by the level of technology available at the time. For example, Kirchhoff [1] first derived the solution for sound propagation in viscous and thermally conducting fluid filled tubes in 1868. However, his results could not be verified by experiment. It was not until many years later that advances in transducer technology and electronics allowed such verification [2].

When working with sound propagation in tubes, the evaluation of any general solution involves specifying the boundary conditions at the tube wall. Such conditions require the specification of the motion and temperature of the wall as functions of time and position. In the cases treated until now, motion and temperature were controlled by the physical properties of the wall and the fluid. Kirchhoff and others following him [2-5], found that in order to match boundary conditions with such walls it was necessary to include thermal and viscous (vorticity) waves in addition to acoustic waves in the boundary layer. (For an excellent source of information

on the effects of entropy and vorticity fluctuations on sound propagation in tubes under various conditions, see Anderson [6].) There is also an extensive area of study involving sound propagation in tubes filled with incompressible fluids [7–13]. In such cases the effects of viscosity and thermal conductivity on the sound are insignificant compared to that due to the motion of the wall.

An outline of various papers dealing with sound propagation in tubes is shown in Tables 0.1–0.3. Straight tubes, curved tubes, and combinations of both types have been studied for various wall conditions. Examples include rigid and porous walls for gas filled tubes, and elastic walls of various thicknesses for liquid filled tubes. The common factor in all these works is that only rigid and passive absorbing walls are considered.

This dissertation studies both theoretically and experimentally a case not previously treated—the case where a traveling wave is generated in the boundary layer and propagated with a controllable velocity and wave number. It is now possible to construct waveguides with such walls due to the development of digitally controlled signal processors. For a steady state wave in an infinitely long tube, the speed of the wave in the fluid will equal the speed of the wave in the wall. Of course an infinitely long tube is not possible; however, a torus containing an integral number of wavelengths can approximate such a tube.

In 1989, Ruppel [14] constructed a planar array of active surface elements to form a surface with independently controllable frequency and wave number. He used this surface to cancel obliquely incident acoustic plane waves by matching the normal components of the sound particle velocity and the velocity of the driven surface. He also demonstrated that such a surface could, in the absence of incident sound, produce

a plane wave steered in a direction determined by the wave number of the surface. This idea has been extended to waveguides with active walls.

The configuration considered here is a waveguide whose walls are moving with a vibratory motion normal to the surface with a controllable frequency and wave number. The wall motion is excited by a digital circuit capable of taking a single input signal and sending it sequentially to multiple outputs with a specific time delay between outputs. If the outputs are used to drive transducers in the walls of the waveguide, the wall will move with the motion approximated by the equation

$$r = a + \Delta r \cos \left( \frac{\omega \Delta t_0 z}{d} - \omega t \right), \quad (0.1)$$

where  $\Delta t_0$  is the delay between outputs,  $d$  is the spacing between transducers in the wall,  $z$  is the distance in the axial direction, and  $\omega$  is the angular frequency of vibration (see Fig. 0.1, for example). The quantity  $k_w$ , the wave number of the wall, is given by

$$k_w = \frac{\omega \Delta t_0}{d}. \quad (0.2)$$

Such a circuit was built and used to make measurements inside a toroidal tube.

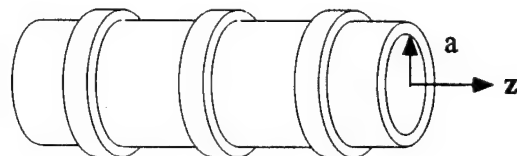


Figure 0.1: Simple design for a tube with active walls. In this example, three driving elements are attached to a short section of tube of radius  $a$ .

In Chapter 1, the theoretical solution for sound propagation in an infinitely long tube with active walls is presented. Both the case of the ideal fluid, as well as the viscous and thermally conducting fluid are considered. Theoretical results of the velocity components for both cases are shown.

In Chapter 2, the theoretical solution for sound propagation in a toroidal wave-guide with both rigid and driven walls is derived for the case of an ideal fluid. Two methods for including losses in the theory are presented.

In Chapter 3, experimental measurements are presented for sound pressure levels in various toroidal tubes. Comparisons to theory are made for cases presented in Chapter 2.

Table 0.1: Papers on straight tubes with rectangular cross-sections

Cross-Sectional Shape	Boundary Conditions	Sources of Attenuation	Reference	Special Considerations
rectangular	porous lining	passive lining	Morse [15] Beranek [16]	Lowest order mode
			Scott [17]	Axial sound propagation in the lining of the wall
			Bokor [18]	Experimental verification of Scott's results
	rigid walls, shear boundary layer	uniform and shear flow	Hersh <i>et al.</i> [19]	Plane wave propagation both upstream and downstream Compares numerical solution to perturbation solution
	porous lining, shear boundary layer	passive lining and shear flow	Kurze <i>et al.</i> [20]	Linear and non-linear duct lining material Effect of high sound levels on attenuation
			Tack <i>et al.</i> [21] Savkar [22]	Plane waves in subsonic flow upstream and downstream Subsonic flows both upstream and downstream Estimation of attenuation by turbulent scattering Subsonic flow velocities both upstream and downstream Waveguide modes based on Ritz-Galerkin technique

Table 0.2: Papers on straight tubes with circular cross-sections

Cross-Sectional Shape	Boundary Conditions	Sources of Attenuation	Reference	Special Considerations
rigid wall	viscosity and thermal conduction	Kirchhoff [1] Rayleigh [3] Weston [4]		Axisymmetric mode
thin elastic wall and a liquid medium	N/A	Shields <i>et al.</i> [2] Tijdeman [5] Jacobi [7]		Experimental verification of Kirchhoff's results Comprehensive review of past work Frequency is proportional to diameter of tube Axisymmetric modes
circular	finite thickness elastic wall and a liquid medium	Lin <i>et al.</i> [8] El-Raheb [9] El-Raheb [10]		Considers rotary inertia and transverse shear Axisymmetric modes Takes into account rotary inertia and transverse shear Asymmetric modes
	porous lining	Fay [11] Del Grossi [12] Kumar [13]		Axisymmetric modes
	porous lining	Morse [15] Mollov <i>et al.</i> [23] Scott [17] Ko [24]		Lowest order mode Graphical solution of Morse's results Axial sound propagation in the lining of the wall Effect of Mach number, boundary layer thickness, flow-resistance, lining thickness and duct geometry on attenuation
	porous lining and axial vibration in lining	Doak <i>et al.</i> [25] Harel <i>et al.</i> [26]		Plane waves as well as higher order modes Subsonic and supersonic flow both upstream and downstream
	porous lining and shear boundary layer	Sovian [27] Eversman [28]		Wavelength much greater than tube radius Subsonic flow both upstream and downstream

Table 0.3: Papers on curved tubes with rectangular and circular cross-sections

Cross-Sectional Shape	Boundary Conditions	Sources of Attenuation	Reference	Special Considerations
rectangular	rigid walls	N/A	Osborne [29]	Modes higher than the fundamental
			El-Raheb [30]	
			Rostafinski [31]	Wavelengths much larger than tube radius
	layered inhomogeneous medium in between walls	Grigor'yan [33] Grigor'yan [34]	Rostafinski [32]	First four modes are studied Wide range of duct widths and curvature considered Characteristics of motion in the bend are compared with propagation of waves in a straight duct
			Normal modes	
			Lowest normal mode	
circular	porous lining	passive lining	Ko <i>et al.</i> [35]	Wavelengths much larger than tube radius Effects of aspect ratio, bend angle and acoustic impedance on the sound attenuation
	rigid and porous lining	passive lining and uniform flow	Cummings [36]	Compares measured results in circular tube to calculations made for rectangular tube Lowest order mode
	rigid wall	N/A	El-Raheb <i>et al.</i> [37]	Green function or surface element method used in 3-D Comparison made to square cross-section for range that includes transverse resonance
	rigid wall and porous lining	passive lining and uniform flow	Cummings [36]	Compares measured results in circular tube to calculations made for rectangular tube Lowest order mode

# Chapter 1

## Theory of the Straight Tube

When working with sound propagation in tubes, the evaluation of any general solution involves specifying the boundary conditions at the tube wall. For liquids, where the walls of the tube are compliant, the wave motions in the wall and liquid are coupled together and are dependent upon the physical properties of the liquid and the wall [7–13]. The expansion of the wall in reaction to a pressure increase in the liquid lowers the effective bulk modulus of the liquid. The result is that the sound speed of the lowest order mode drops below the speed in the infinite medium. For gases, the tube wall impedance is generally much greater than that of the gas inside so that the wall is effectively rigid. For this case the lowest order mode of propagation corresponds to the speed of sound in the infinite medium.

In his great work on acoustics, Lord Rayleigh [3] (Section 348–350) derives the exact solution for sound propagation in a rigid tube first solved by Kirchhoff [1]. His approach to the problem is to combine the four basic equations of acoustics into a single differential equation in terms of temperature, from which the velocity

components can be derived. His solution for the components of velocity consists of three terms, each corresponding to a mode of propagation: the *acoustic mode*, the *vorticity mode*, and the *temperature or entropy mode*. The acoustic mode is the dominant mode and is what we refer to as sound. The vorticity mode is a shear wave traveling in the  $z$  direction above a plate moving back and forth in the  $x-y$  plane. The entropy mode is due to heat flow out of the fluid and into the conducting wall of the tube. This approach differs from that of Pierce [38], who solves the problem by considering the general field to be a linear superposition of individual modal fields that are uncoupled except at the boundaries. These modes are decomposed through dispersion relations, which relate the square of the wave number to the frequency. This is referred to as *modal theory*. In this chapter, Rayleigh's approach will be used to derive the exact solution for the viscous tube and then apply a driven wall boundary condition. (This derivation is adapted from lecture notes prepared by Raspert [39].)

## 1.1 The Wave Equation

Throughout this paper, solutions for the particle velocity and pressure of sound in cylindrical coordinates will be used. It is therefore convenient to now solve for the general solution of the wave equation in such a coordinate system.

The wave equation in terms of the velocity potential is given by

$$\nabla^2 \Phi = \frac{1}{c^2} \frac{\partial^2 \Phi}{\partial t^2}. \quad (1.1)$$

The velocity potential is related to the particle velocity and pressure by  $\mathbf{u} = \nabla \Phi$

and  $p = -\rho_0(\partial\Phi/\partial t)$ , respectively. (For the derivation of the wave equation from the basic linear equations of acoustics, see Pierce [38].) In cylindrical coordinates,

$$\frac{1}{r} \frac{\partial}{\partial r} \left( r \frac{\partial \Phi}{\partial r} \right) + \frac{1}{r^2} \frac{\partial^2 \Phi}{\partial \theta^2} + \frac{\partial^2 \Phi}{\partial z^2} = \frac{1}{c^2} \frac{\partial^2 \Phi}{\partial t^2}. \quad (1.2)$$

Assuming a solution of the form

$$\Phi = R(r)\Theta(\theta)Z(z) \exp(-i\omega t) \quad (1.3)$$

and separating variables yields three equations (each a function of one of the coordinates):

$$\frac{1}{\Theta} \frac{d\Theta}{d\theta} = -m^2, \quad (1.4)$$

$$\frac{1}{Z} \frac{dZ}{dz} = -k_z^2, \quad (1.5)$$

$$\frac{1}{r} \frac{dR}{dr} + \frac{dR}{dr} + \left( \frac{\omega^2}{c^2} - k_z^2 - \frac{m^2}{r^2} \right) R = 0, \quad (1.6)$$

where  $k_z$  and  $m$  are constants. The solution to Eq. (1.6) is

$$R(r) = A_r J_m(k_r r) + B_r Y_m(k_r r) \quad (1.7)$$

where

$$k_r^2 = \frac{\omega^2}{c^2} - k_z^2. \quad (1.8)$$

The solutions to Eqs. (1.4) and (1.5) can be written in terms of sines and cosines or

in terms of exponential functions, i.e.,

$$\Theta(\theta) = A_\theta e^{im\theta} + B_\theta e^{-im\theta}, \quad (1.9)$$

$$Z(z) = A_z e^{ik_z z} + B_z e^{-ik_z z}, \quad (1.10)$$

or

$$\Theta(\theta) = A_\theta \cos(m\theta) + B_\theta \sin(m\theta), \quad (1.11)$$

$$Z(z) = A_z \cos(k_z z) + B_z \sin(k_z z). \quad (1.12)$$

These expressions for  $R(r)$ ,  $\Theta(\theta)$ , and  $Z(z)$  when substituted into Eq. (1.3) give the general solution for the velocity potential in cylindrical coordinates.

## 1.2 A Lossless Fluid Filled Tube with Driven Walls

### 1.2.1 Theory

Before solving for the viscous fluid filled tube, it is useful to start out with the simple case of an infinitely long tube filled with a lossless fluid, i.e., viscosity and thermal conductivity will be ignored. The desired solution is obtained by applying a driven wall boundary condition to Eq. (1.3).

Let the radius of the tube be  $a$  with the axis oriented in the  $z$  direction as shown in Fig. 1.1. Azimuthal symmetry is assumed, which requires that the velocity potential have no  $\theta$  dependence, so that  $m = 0$ . Since  $r = 0$  is contained in the region of interest, and the Neumann function becomes infinite at  $r = 0$ ,  $B_r$  must equal zero

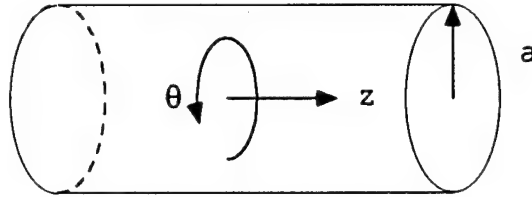


Figure 1.1: The cylindrical tube.

in Eq. (1.7). The general velocity potential for the acoustic wave traveling in the  $+z$  direction is then,

$$\Phi = A_r J_0(k_r r) e^{i(k_z z - \omega t)}. \quad (1.13)$$

Using this solution to solve for the radial and axial components of the particle velocity yields

$$v(r, z, t) = -A_r \left( \frac{\omega^2}{c^2} - k_z^2 \right)^{\frac{1}{2}} J_1 \left( r \sqrt{\frac{\omega^2}{c^2} - k_z^2} \right) e^{i(k_z z - \omega t)}, \quad (1.14)$$

$$w(r, z, t) = i k_z A_r J_0 \left( r \sqrt{\frac{\omega^2}{c^2} - k_z^2} \right) e^{i(k_z z - \omega t)}. \quad (1.15)$$

In order to solve for  $A_r$  and  $k_z$ , it is necessary apply the boundary condition at the wall. Let the wall be driven at a frequency  $\omega$  with a wave number  $k_w$ . At  $r = a$ , the radial velocity  $v$  is

$$v(a, z, t) = V_0 e^{i(k_w z - \omega t)}. \quad (1.16)$$

This boundary condition requires that the axial wave number  $k_z$  be equal to the axial wall wave number  $k_w$ . Solving for  $A_r$  in Eq. (1.14) yields the steady-state solution for the components of particle velocity amplitude (where  $v$  and  $w$  are now instantaneous

velocity amplitudes)

$$\frac{v}{V_0} = \frac{J_1 \left( kr \sqrt{1 - (c/c_w)^2} \right)}{J_1 \left( ka \sqrt{1 - (c/c_w)^2} \right)}, \quad (1.17)$$

and

$$\frac{w}{V_0} = \frac{-i}{\sqrt{(c_w/c)^2 - 1}} \frac{J_0 \left( kr \sqrt{1 - (c/c_w)^2} \right)}{J_1 \left( ka \sqrt{1 - (c/c_w)^2} \right)}, \quad (1.18)$$

where the wave number  $k$  has been introduced, which is defined as

$$k \equiv \omega/c, \quad (1.19)$$

and the wall wave velocity is

$$c_w = \omega/k_w. \quad (1.20)$$

### 1.2.2 Results

Figure 1.2 shows the ratio of the amplitude of the axial particle velocity to the amplitude of the wall vibration at a value of  $r = a/2$  as a function of  $ka$  and  $c_w$ . (The breaks in the ridges are due to the finite grid in the calculations.) When  $c_w$  corresponds to the propagation speed for a rigid wall mode, driving the wall with a finite amplitude produces an infinite amplitude axial wave. Figure 1.3 is the corresponding plot for the component of the particle velocity in the radial direction.

For sound propagation in fluid cylinders with rigid walls, there are only certain combinations of phase velocity and angular frequency allowed. These are referred to as modes of the system (see Jacobi [7] for example). Comparing Fig. 1.2 to the propagation modes for a fluid cylinder of the same dimensions with rigid walls, one

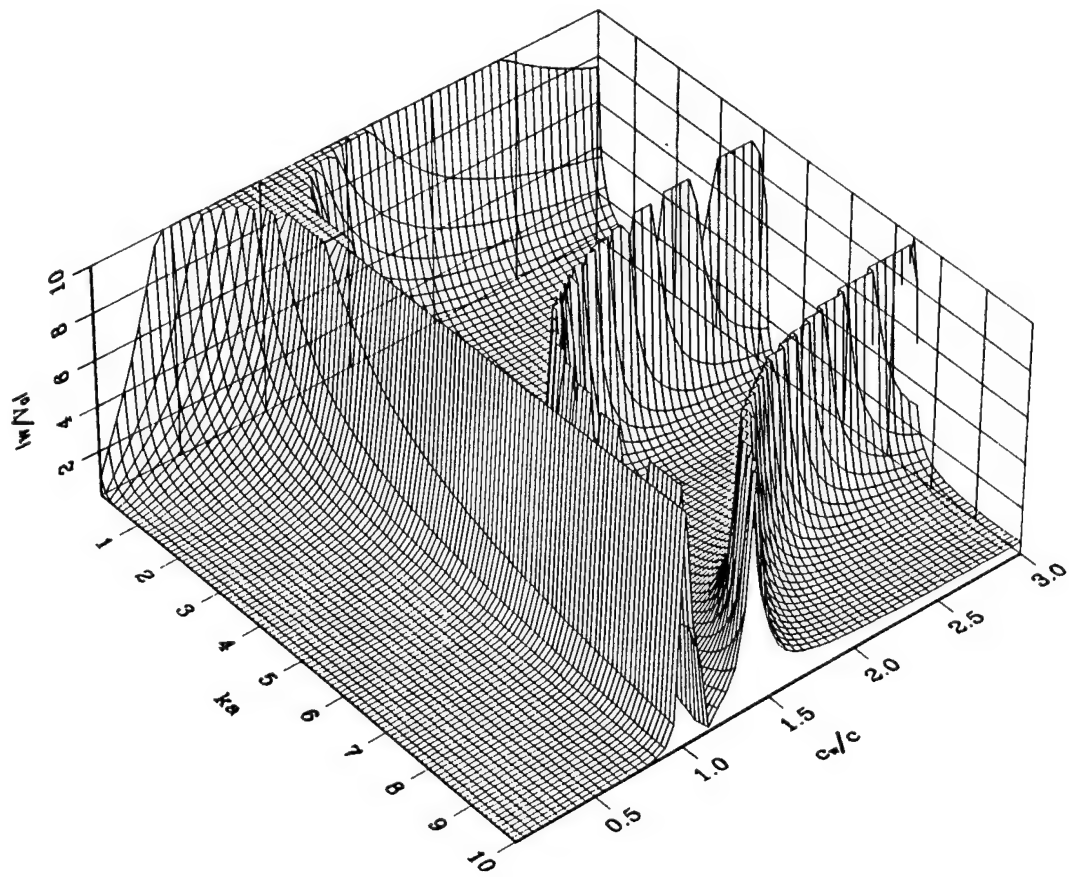


Figure 1.2: Normalized axial velocity amplitude for a lossless fluid filled tube as a function of the dimensionless wave number  $ka$  and propagation speed  $c_w/c$ . Plot made for  $r = a/2$ .

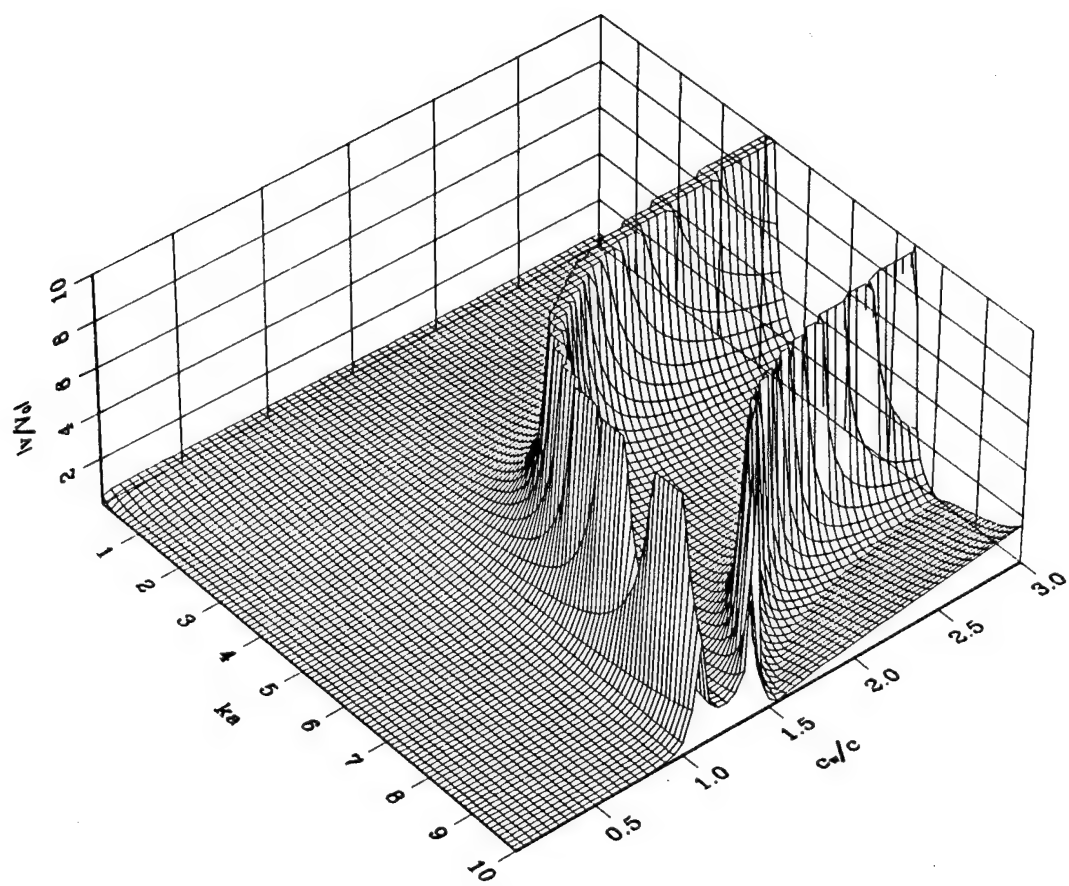


Figure 1.3: Normalized radial velocity amplitude for a lossless fluid filled tube as a function of the dimensionless wave number  $ka$  and propagation speed  $c_w/c$ . Plot made for  $r = a/2$ .

finds that the three ridges correspond to the first three symmetric modes of the rigid wall fluid cylinder. The ridge that follows  $c_w/c = 1$  corresponds to the (0,0) mode (which is the plane wave mode), the next ridge is the (0,1) mode and the third is the (0,2) mode. Inspection of Fig. 1.3 shows that there is very little plane wave component in the radial velocity at  $c_w = c$ , so that the propagating plane wave is primarily a longitudinal wave.

For the case of a fluid filled tube with rigid walls, the only modes that propagate are those that satisfy the condition that in Eq. (1.14)

$$v|_{r=a} = 0. \quad (1.21)$$

For the driven wall tube, however, there is no such restriction, so that waves of any combination of wave number and frequency can be produced. When the driving conditions of the tube correspond to cases of these rigid tube modes, the axial velocity amplitude is infinite because the denominator of Eq. (1.18) is zero. This is also true for the radial velocity when  $0 < r < a$  except for the case of  $c_w = c$ , where

$$\lim_{c_w \rightarrow c} \frac{v}{V_0} = \frac{r}{a}. \quad (1.22)$$

This connection between the cases of the rigid and driven wall tubes will also be seen in the derivation of sound propagation in a toroidal waveguide carried out in Chapter 2.

Figure 1.4 shows the amplitude of the axial velocity as a function of radial position and speed of propagation of the wave in the driven wall for  $ka = 1$  which is well below

the cut-off frequency of the first order mode. Figure 1.5 shows the corresponding plot when the frequency is high enough to see the higher order modes. (Note that the axis has been rotated in order to better display the higher order modes.)

Figures 1.6 and 1.7 show corresponding plots for the radial velocity as a function of  $r$  and  $c_w$  for  $ka = 1$  and  $ka = 8$ . Again the particle velocity becomes infinite when the driven wall is a nodal surface of a radial mode. On a plot with a finer scale the curved ridges become infinite in amplitude with notches at the Bessel function roots [see Eqs. (1.17) and (1.18)]. The figures present challenging questions about what is happening on the molecular scale. When the driven wall is at a nodal surface for radial motion, theoretically the wall experiences an infinite impedance. The sound pressure and the sound temperature fluctuations in the gas become infinite. Clearly it is important to investigate the viscous and thermal losses in the gas for these driving configurations. This investigation is the subject of the next section.

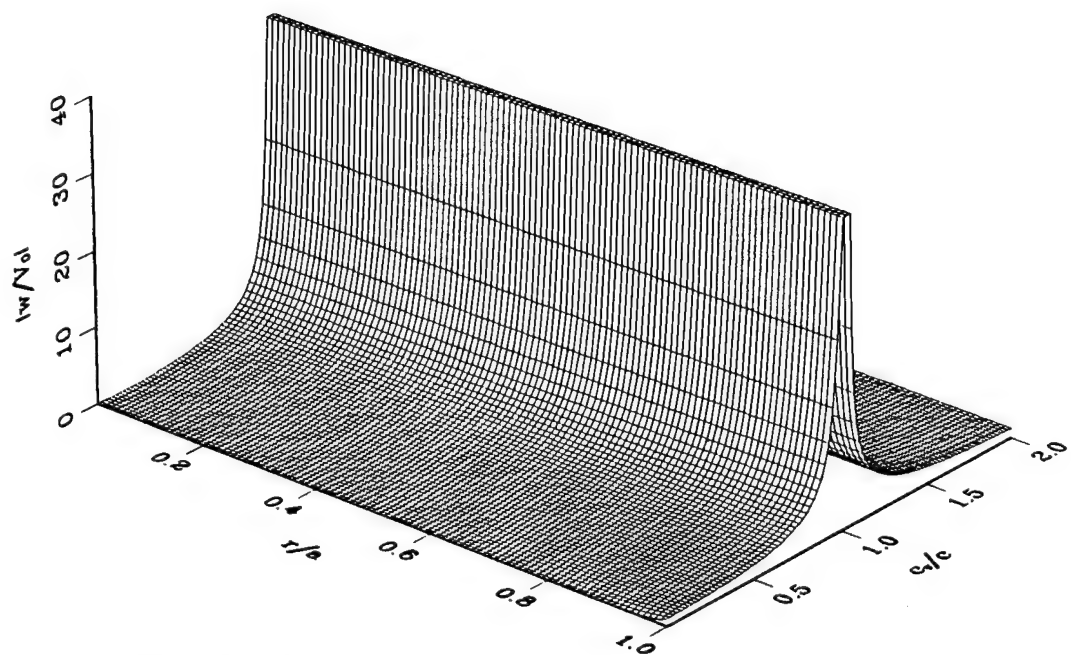


Figure 1.4: Normalized axial velocity amplitude for a lossless fluid filled tube as a function of the dimensionless radial position  $r/a$  and propagation speed  $c_w/c$ . Plot made for  $ka = 1$ .

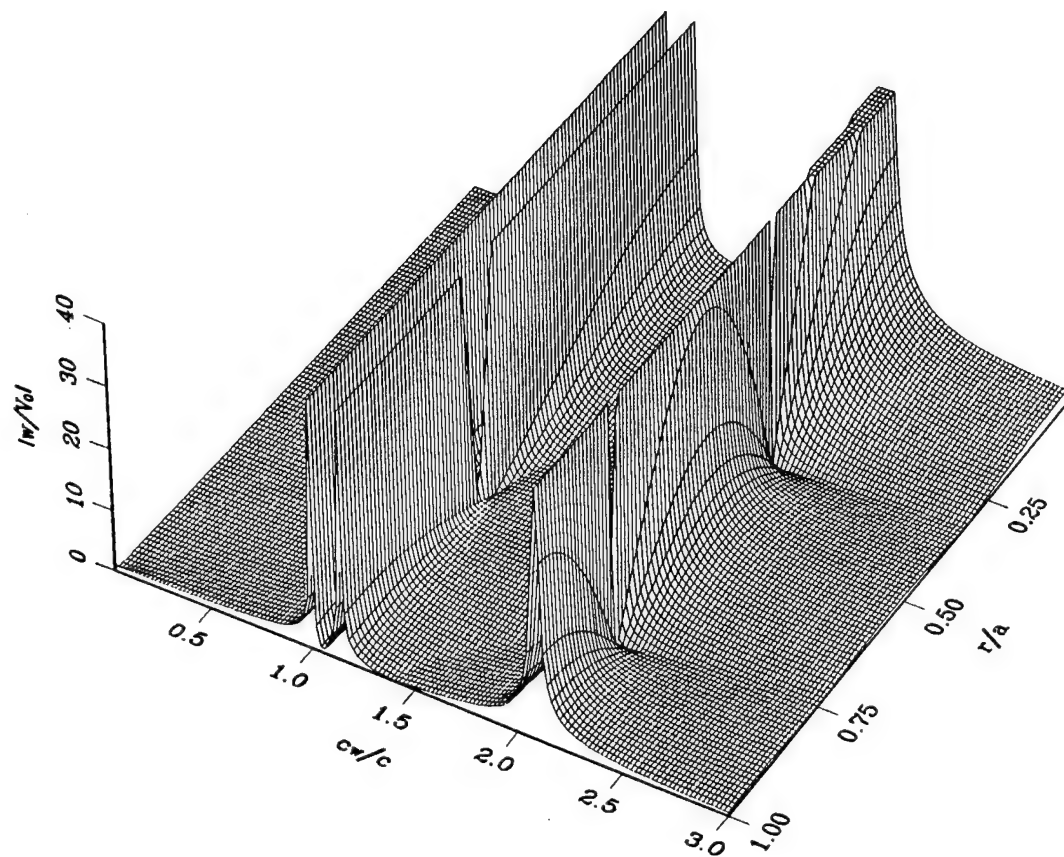


Figure 1.5: Normalized axial velocity amplitude for a lossless fluid filled tube as a function of the dimensionless radial position  $r/a$  and propagation speed  $c_w/c$ . Plot made for  $ka = 8$ .

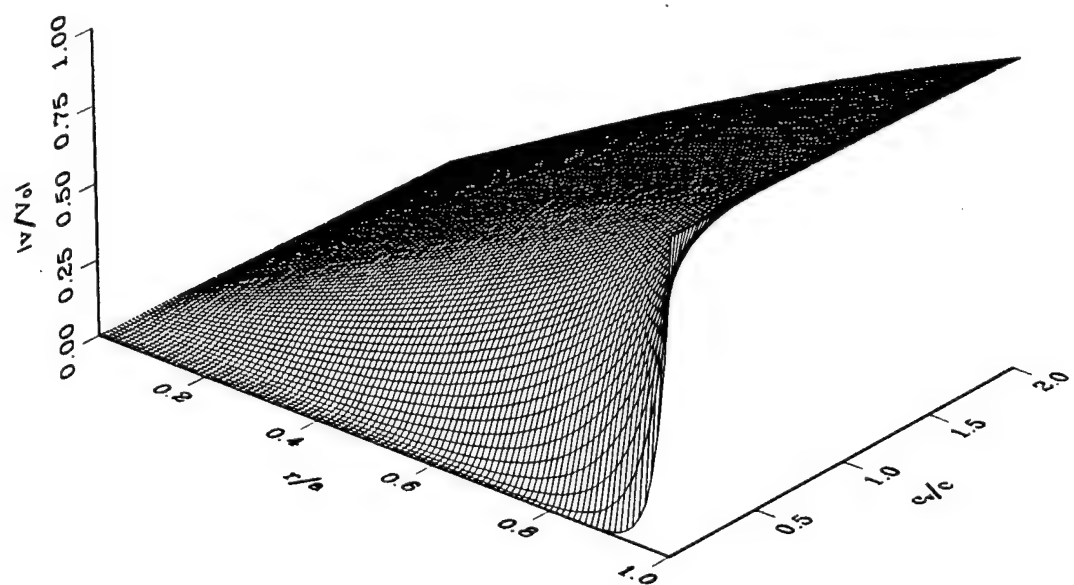


Figure 1.6: Normalized radial velocity amplitude for a lossless fluid filled tube as a function of the dimensionless radial position and propagation speed  $c_w/c$ . Plot made for  $ka = 1$ .

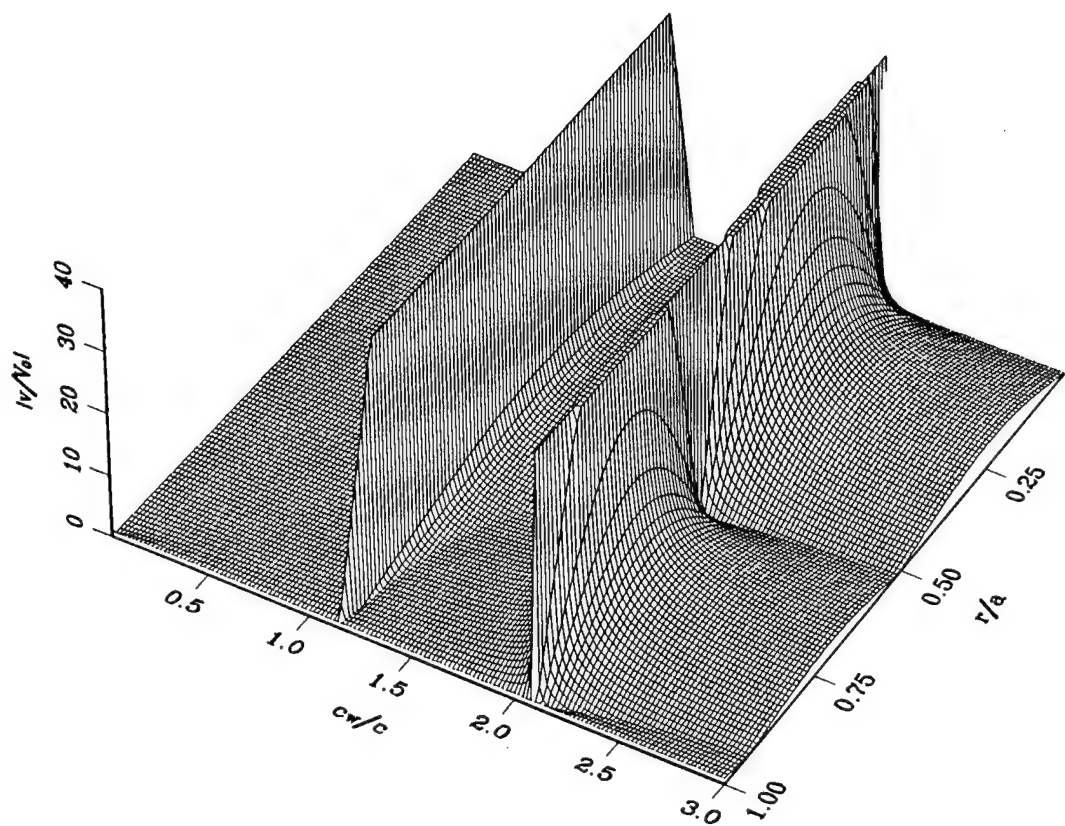


Figure 1.7: Normalized radial velocity amplitude for a lossless fluid filled tube as a function of the dimensionless radial position and propagation speed  $c_w/c$ . Plot made for  $ka = 8$ .

## 1.3 Viscid and Thermally Conducting Fluid Filled Tube with Driven Walls

### 1.3.1 Derivation of the General Equation

To solve for the case of the viscous and thermally conductivity medium, one must begin with the basic conservation equations where the effects of viscosity and thermal conduction have been included. These are [38]

$$\frac{1}{\rho_0} \frac{\partial \rho}{\partial t} + \nabla \cdot \mathbf{u} = 0, \quad (1.23)$$

$$\rho_0 \frac{\partial \mathbf{u}}{\partial t} = -\nabla p + \mu \left[ \nabla^2 \mathbf{u} + \frac{1}{3} \nabla (\nabla \cdot \mathbf{u}) \right], \quad (1.24)$$

$$\rho_0 T_0 \frac{\partial s}{\partial t} = \kappa \nabla^2 T, \quad (1.25)$$

$$\frac{p}{\rho_0} = \frac{1}{\rho_0} \left( \frac{\partial p}{\partial \rho} \right)_T \rho + \frac{1}{\rho_0} \left( \frac{\partial p}{\partial T} \right)_\rho T. \quad (1.26)$$

In these equations, the quantities  $p$ ,  $\rho$ ,  $T$ , and  $\mathbf{u}$  are acoustic variables with small amplitudes. Equation (1.23) is the equation of continuity which expresses the conservation of mass. Equation (1.24) is the Navier-Stokes equation which expresses the conservation of momentum. Equation (1.25) is the Fourier-Kirchhoff equation which expresses the conservation of energy. Equation (1.26) is the equation of state which results from assuming that the pressure is a function of temperature and density. The goal is to use these four equations to solve for the four acoustic variables listed above. Following Kirchhoff and Rayleigh, Eqs. (1.23)–(1.25) will be written in a more

compact form, and then solved for a single differential equation in terms of temperature, from which expressions for the other three variables can be found. The ultimate goal is to solve for the particle velocity components in the presence of a boundary.

Assume an  $\exp(-i\omega t)$  dependence so that  $\partial/\partial t$  can be replaced by  $-i\omega$ . Then Eqs. (1.23)–(1.25) become

$$-\frac{i\omega\rho}{\rho_0} + \nabla \cdot \mathbf{u} = 0, \quad (1.27)$$

$$i\omega\rho_0\mathbf{u} = \nabla p - \mu \left[ \nabla^2 \mathbf{u} + \frac{1}{3} \nabla (\nabla \cdot \mathbf{u}) \right], \quad (1.28)$$

$$-i\omega\rho_0 T_0 s = \kappa \nabla^2 T. \quad (1.29)$$

Eliminating  $\nabla \cdot \mathbf{u}$  in Eq. (1.28) and Eq. (1.27) and grouping the gradient terms together yields

$$i\omega\rho_0\mathbf{u} + \mu\nabla^2\mathbf{u} = \nabla \left( p - \frac{i\mu\omega\sigma}{3} \right), \quad (1.30)$$

where  $\sigma \equiv \rho/\rho_0$  is the condensation. Let

$$\mathcal{P} \equiv p - \frac{i\mu\omega\sigma}{3}, \quad (1.31)$$

where  $\mathcal{P}$  is a complex pressure with the real part corresponding to the pressure fluctuation in the medium and the imaginary part corresponding to a pressure associated with the shear force on the fluid. Then Eq. (1.30) becomes

$$i\omega\rho_0\mathbf{u} + \mu\nabla^2\mathbf{u} = \nabla\mathcal{P}. \quad (1.32)$$

This is the new Navier-Stokes equation.

Equation (1.29) can be rewritten using the entropy  $s(T, \rho)$  expanded by the chain-rule (see Appendix A);

$$-i\omega T + i\omega\sigma\rho_0 \left( \frac{\partial T}{\partial \rho} \right)_s = \frac{\kappa\nabla^2 T}{\rho_0 C_v}, \quad (1.33)$$

where  $C_v$  is the specific heat at constant volume given by,

$$C_v = T_0 \left( \frac{\partial s}{\partial T} \right)_\rho. \quad (1.34)$$

Consider  $(\partial p / \partial \rho)_s$ :

$$\begin{aligned} \left( \frac{\partial p}{\partial \rho} \right)_s &= \left( \frac{\partial p}{\partial \rho} \right)_T + \left( \frac{\partial p}{\partial T} \right)_\rho \left( \frac{\partial T}{\partial \rho} \right)_s \\ \frac{(\partial p / \partial \rho)_s}{(\partial p / \partial \rho)_T} &= 1 + \left( \frac{\partial p}{\partial T} \right)_\rho \left( \frac{\partial T}{\partial \rho} \right)_s \left( \frac{\partial \rho}{\partial p} \right)_T \\ \gamma &= 1 - \left( \frac{\partial T}{\partial \rho} \right)_s \left( \frac{\partial \rho}{\partial T} \right)_p \\ \gamma &= 1 - \rho_0 \alpha \left( \frac{\partial T}{\partial \rho} \right)_s, \end{aligned}$$

or

$$\left( \frac{\partial T}{\partial \rho} \right)_s = \frac{1 - \gamma}{\rho_0 \alpha}, \quad (1.35)$$

where  $\alpha = -\rho_0^{-1}(\partial \rho / \partial T)_p$  is the coefficient of expansion,  $\gamma$  is the ratio of specific heats and

$$\frac{(\partial p / \partial \rho)_s}{(\partial p / \partial \rho)_T} = \gamma. \quad (1.36)$$

Substituting this into Eq. (1.33) and multiplying through by  $\alpha/(\gamma - 1)$  yields

$$-i\omega \left( \frac{\alpha T}{\gamma - 1} \right) - i\omega\sigma = \frac{\kappa}{\rho_0 C_v} \nabla^2 \left( \frac{\alpha T}{\gamma - 1} \right). \quad (1.37)$$

Let  $\mathcal{T}$  be defined as a dimensionless temperature given by

$$\mathcal{T} \equiv \frac{\alpha T}{\gamma - 1}. \quad (1.38)$$

Substituting this into Eq. (1.37) yields

$$-i\omega\mathcal{T} - i\omega\sigma = \frac{\kappa}{\rho_0 C_v} \nabla^2 \mathcal{T}. \quad (1.39)$$

This is the new Fourier-Kirchhoff equation.

Consider Eq. (1.26):

$$\begin{aligned} \frac{p}{\rho_0} &= \left( \frac{\partial p}{\partial \rho} \right)_T \left( \frac{\rho}{\rho_0} \right) + \frac{1}{\rho_0} \left( \frac{\partial p}{\partial T} \right)_\rho T \\ &= \left( \frac{\partial p}{\partial \rho} \right)_T \sigma + \frac{1}{\rho_0} \left( \frac{\partial p}{\partial T} \right)_\rho T \\ &= c_T^2 \sigma + \frac{1}{\rho_0} \left( \frac{\partial p}{\partial T} \right)_\rho T \\ &= c_T^2 \sigma - \frac{1}{\rho_0} \left( \frac{\partial \rho}{\partial T} \right)_p \left( \frac{\partial p}{\partial \rho} \right)_T T \\ &= c_T^2 \sigma + c_T^2 \alpha T \end{aligned} \quad (1.40)$$

where  $c_T^2 = (\partial p / \partial \rho)_T$  and  $c^2 = (\partial p / \partial \rho)_s$  are the isothermal and adiabatic speed of

sound respectively. Substituting this along with Eq. (1.38) into Eq. (1.31) yields

$$\mathcal{P} = \left( c_T^2 \rho_0 - \frac{i\omega\mu}{3} \right) \sigma + \rho_0 (c_T^2 - c^2) \mathcal{T}. \quad (1.41)$$

This the new equation of state.

Grouping the new linear equations,

$$-i\omega\sigma + \nabla \cdot \mathbf{u} = 0, \quad (1.42)$$

$$i\omega\rho_0\mathbf{u} + \mu\nabla^2\mathbf{u} = \nabla\mathcal{P}, \quad (1.32)$$

$$-i\omega\mathcal{T} - i\omega\sigma = \frac{\kappa}{\rho_0 C_v} \nabla^2\mathcal{T}, \quad (1.39)$$

$$\mathcal{P} = \left( c_T^2 \rho_0 - \frac{i\omega\mu}{3} \right) \sigma + \rho_0 (c_T^2 - c^2) \mathcal{T}, \quad (1.41)$$

constituting four equations and four unknowns  $\mathcal{T}$ ,  $\mathbf{u}$ ,  $\mathcal{P}$ , and  $\sigma$ . At this point, these equations can be combined to form a single equation in terms of only  $\mathcal{T}$ . The solution for the temperature equation will be needed to derive the components of velocity because the entropy and the acoustic modes are coupled together.

Taking the divergence of Eq. (1.32) yields

$$i\omega\nabla \cdot \mathbf{u} + \frac{\mu}{\rho_0} \nabla^2 (\nabla \cdot \mathbf{u}) = \nabla^2\mathcal{P}. \quad (1.43)$$

Using Eqs. (1.42), (1.39), and (1.41) in Eq. (1.43) to eliminate  $\mathbf{u}$ ,  $\mathcal{P}$ , and  $\sigma$  yields

$$\omega^2\mathcal{T} + \left[ c^2 - i\omega \left( \frac{4\mu}{3\rho_0} + \frac{\kappa}{\rho_0 C_v} \right) \right] \nabla^2\mathcal{T} + \left( c_T - \frac{4i\omega\mu}{3\rho_0} \right) \frac{\kappa}{i\omega\rho_0 C_v} \nabla^4\mathcal{T} = 0. \quad (1.44)$$

For convenience, the vorticity and entropy *skin depths* will be introduced where

$$l_v = \sqrt{\frac{2\mu}{\omega\rho_0}} \quad (1.45)$$

and

$$l_e = \sqrt{\frac{2\kappa}{\omega\rho_0\gamma C_v}}. \quad (1.46)$$

Then Eq. (1.44) becomes

$$\frac{\omega^2}{c^2}T + \left[1 - i\left(\frac{\omega^2 l_e^2}{2c_T^2} + \frac{2\omega^2 l_v^2}{3c^2}\right)\right]\nabla^2 T - \left(1 - \frac{2i\omega^2 l_v^2}{3c_T^2}\right)\frac{i l_e^2}{2}\nabla^4 T = 0. \quad (1.47)$$

This equation is a fourth-order differential equation which is a function of  $T$  only. From this equation, a solution for  $T$  can be found from which the solution for the particle velocity can be found.

### 1.3.2 Solution for the Temperature Equation

Assume a solution to Eq. (1.47) of the form

$$T = A_1 Q_1(r) e^{ik_z z} + A_2 Q_2(r) e^{ik_z z} \quad (1.48)$$

where

$$\nabla^2 [Q_{1,2}(r) e^{ik_z z}] = \lambda_{1,2} Q_{1,2}(r) e^{ik_z z}. \quad (1.49)$$

Substitution into Eq. (1.47) requires  $\lambda_1$  and  $\lambda_2$  be the roots of

$$\frac{\omega^2}{c^2} + \lambda_{1,2} \left[ 1 - i \left( \frac{\omega^2 l_e^2}{2c_T^2} + \frac{2\omega^2 l_v^2}{3c^2} \right) \right] - \lambda_{1,2}^2 \left( 1 - \frac{2i\omega^2 l_v^2}{3c_T^2} \right) \frac{i l_e^2}{2} = 0. \quad (1.50)$$

Usually, the product of the thermoviscous skin depth and the wave number of the sound in the medium will be much less than one, so dropping insignificant terms yields

$$\frac{\omega^2}{c^2} + \lambda_{1,2} - \frac{i l_e^2 \lambda_{1,2}^2}{2} \approx 0. \quad (1.51)$$

The solutions for  $\lambda_{1,2}$  are then

$$\begin{aligned} \lambda_{1,2} &\approx \frac{-1 \pm \sqrt{1 + 2i l_e^2 (\omega/c)^2}}{-i l_e^2} \\ &\approx \frac{-1 \pm 1 + i l_e^2 (\omega/c)^2}{-i l_e^2} \end{aligned} \quad (1.52)$$

where

$$\lambda_1 \approx -\frac{\omega^2}{c^2} \quad (1.53)$$

is the acoustic root and

$$\lambda_2 \approx -\frac{2i}{l_e^2} \quad (1.54)$$

is the thermal root.

Consider an axially symmetric disturbance in a cylindrical tube of radius  $a$  oriented in the  $z$  direction as shown in Fig. 1.1. In cylindrical coordinates, Eq. (1.49) becomes

$$\frac{\partial^2}{\partial r^2} [Q_{1,2}(r) e^{ik_z z}] + \frac{1}{r} \frac{\partial}{\partial r} [Q_{1,2}(r) e^{ik_z z}] + \frac{\partial^2}{\partial z^2} [Q_{1,2}(r) e^{ik_z z}] = \lambda_{1,2} Q_{1,2}(r) e^{ik_z z} \quad (1.55)$$

which becomes

$$\frac{dQ_{1,2}}{dr} + \frac{1}{r} \frac{dQ_{1,2}}{dr} = (\lambda_{1,2} + k_z^2) Q_{1,2}. \quad (1.56)$$

The general solution for this equation is, from Section 1.1,

$$Q_{1,2} = J_0 \left( r \sqrt{-k_z^2 - \lambda_{1,2}} \right) \quad (1.57)$$

(Because  $r = 0$  is contained in the region of interest, the Neumann function, which becomes infinite at  $r = 0$ , has been dropped.)

Equation (1.44) can now be solved using Eq. (1.48) in terms of  $A_1$  and  $A_2$ . These coefficients can then be evaluated using the boundary conditions at the tube wall to give the solution for the temperature fluctuations inside the tube as a function of position inside the tube.

### 1.3.3 Solution for the Velocity Equation

At this point, the interest is in obtaining a solution for the axial and radial particle velocities associated with sound in the tube. Consider  $\mathbf{u} = \mathbf{u}' + \mathbf{u}''$ , where  $\mathbf{u}'$  is the homogeneous solution and  $\mathbf{u}''$  is the particular solution. Substituting Eq. (1.42) into Eq. (1.39) to eliminate  $\sigma$  yields

$$\nabla \cdot \mathbf{u}' + \nabla \cdot \mathbf{u}'' + i\omega T + \frac{\gamma l_e^2 \omega}{2} \nabla^2 T = 0, \quad (1.58)$$

which relates the divergence of the velocity to the temperature, for which a solution has already been found.

Dividing this equation into its parts, the homogeneous equation is

$$\nabla \cdot \mathbf{u}' = 0, \quad (1.59)$$

and the particular equation is

$$\nabla \cdot \mathbf{u}'' + i\omega T + \frac{\gamma l_e^2 \omega}{2} \nabla^2 T = 0. \quad (1.60)$$

Assume a solution for the particular velocity

$$\mathbf{u}'' = \nabla [B_1 Q_1(r) e^{ik_z z} + B_2 Q_2(r) e^{ik_z z}]. \quad (1.61)$$

Substituting this into Eq. (1.60), along with the solution for  $T$  given by Eq. (1.48), yields

$$\begin{aligned} 0 &= \nabla \cdot \{ \nabla [B_1 Q_1(r) e^{ik_z z} + B_2 Q_2(r) e^{ik_z z}] \} + i\omega [A_1 Q_1(r) + A_2 Q_2(r)] e^{ik_z z} \\ &\quad + \frac{\gamma l_e^2 \omega}{2} \{ A_1 \nabla^2 [Q_1(r) e^{ik_z z}] + A_2 \nabla^2 [Q_2(r) e^{ik_z z}] \}. \end{aligned} \quad (1.62)$$

For this equation to always be true,

$$\begin{aligned} 0 &= B_{1,2} \nabla^2 [Q_{1,2}(r) e^{ik_z z}] + i\omega A_{1,2} Q_{1,2}(r) e^{ik_z z} \\ &\quad + \frac{\gamma l_e^2 \omega}{2} A_{1,2} \nabla^2 [Q_{1,2}(r) e^{ik_z z}]. \end{aligned} \quad (1.63)$$

Solving for  $B_{1,2}$  using Eq. (1.49) gives

$$B_{1,2} = -A_{1,2}\omega \left( \frac{\gamma l_e^2}{2} + \frac{i}{\lambda_{1,2}} \right) \quad (1.64)$$

which, along with Eq. (1.61), is the general solution for the particular part of the velocity.

To find the solution for  $\mathbf{u}'$ , consider Eq. (1.32). The homogeneous part is

$$i\omega \mathbf{u}' + \frac{l_v^2 \omega}{2} \nabla^2 \mathbf{u}' = 0. \quad (1.65)$$

This is a vector equation and holds for the individual components of  $\mathbf{u}$ .

Consider first the axial component so that Eq. (1.65) becomes

$$\begin{aligned} 0 &= i w' + \frac{l_v^2}{2} \left( \frac{\partial^2 w'}{\partial r^2} + \frac{1}{r} \frac{\partial w'}{\partial r} + \frac{\partial^2 w'}{\partial z^2} \right) \\ &= i w' + \frac{l_v^2}{2} \left( \frac{\partial^2 w'}{\partial r^2} + \frac{1}{r} \frac{\partial w'}{\partial r} - k_z^2 w' \right) \\ &= \frac{\partial^2 w'}{\partial r^2} + \frac{1}{r} \frac{\partial w'}{\partial r} + \left( -k_z^2 + \frac{2i}{l_v^2} \right) w' \end{aligned} \quad (1.66)$$

which has an axisymmetric solution

$$w' = A_0 Q_0 e^{ik_z z}, \quad (1.67)$$

where

$$Q_0 = J_0 \left( r \sqrt{-k_z^2 + 2i/l_v^2} \right). \quad (1.68)$$

Now consider the radial component of the homogeneous velocity. From Eq. (1.59)

the relationship between  $w'$  and  $v'$  is

$$\begin{aligned} 0 &= \frac{1}{r} \frac{\partial r v'}{\partial r} + \frac{\partial w'}{\partial z} \\ &= \frac{v'}{r} + \frac{\partial v'}{\partial r} + \frac{\partial w'}{\partial z} \\ &= \frac{v'}{r} + \frac{\partial v'}{\partial r} + i k_z w'. \end{aligned} \quad (1.69)$$

Using a solution of the form

$$v' = B_0 \frac{dQ_0}{dr} e^{ik_z z} \quad (1.70)$$

in Eq. (1.69) yields

$$\begin{aligned} 0 &= \frac{B_0}{r} \frac{dQ_0}{dr} + B_0 \frac{dQ_0}{dr} + i k_z A_0 Q_0 \\ &= B_0 \left( \frac{dQ_0}{dr} + \frac{1}{r} \frac{dQ_0}{dr} \right) + i k_z A_0 Q_0. \end{aligned} \quad (1.71)$$

From Eq. (1.66)

$$\frac{dQ_0}{dr} + \frac{1}{r} \frac{dQ_0}{dr} = - \left( -k_z^2 + \frac{2i}{l_v^2} \right) Q_0 \quad (1.72)$$

which when substituted into Eq. (1.71) yields

$$0 = -B_0 Q_0 \left( -k_z^2 + \frac{2i}{l_v^2} \right) + i k_z A_0 Q_0. \quad (1.73)$$

Solving for  $B_0$  and substituting into Eq. (1.70) gives

$$v' = \frac{i A_0 k_z}{2i/l_v^2 - k_z^2} \frac{dQ_0}{dr} e^{ik_z z}. \quad (1.74)$$

Combining Eq. (1.67) with Eq. (1.61), the general solution for the axial component of the sound velocity in the tube is

$$\begin{aligned}
 w &= w' + w'' \\
 &= A_0 Q_0 e^{ik_z z} - \sum_{j=1}^2 \frac{\partial}{\partial z} \left[ A_j \omega \left( \frac{\gamma l_e^2}{2} + \frac{i}{\lambda_j} \right) Q_j(r) e^{ik_z z} \right] \\
 &= \left[ A_0 Q_0 - \sum_{j=1}^2 i A_j k_z \omega \left( \frac{\gamma l_e^2}{2} + \frac{i}{\lambda_j} \right) Q_j \right] e^{ik_z z}. \tag{1.75}
 \end{aligned}$$

Combining Eq. (1.74) with Eq. (1.61), the general solution for the radial component of the sound velocity in the tube is

$$\begin{aligned}
 v &= v' + v'' \\
 &= \frac{i A_0 k_z}{2i/l_v^2 - k_z^2} \frac{dQ_0}{dr} e^{ik_z z} - \sum_{j=1}^2 \frac{\partial}{\partial r} \left[ A_j \omega \left( \frac{\gamma l_e^2}{2} + \frac{i}{\lambda_j} \right) Q_j(r) e^{ik_z z} \right] \\
 &= \left[ \frac{i A_0 k_z}{2i/l_v^2 - k_z^2} \frac{dQ_0}{dr} - \sum_{j=1}^2 A_j \omega \left( \frac{\gamma l_e^2}{2} + \frac{i}{\lambda_j} \right) \frac{dQ_j}{dr} \right] e^{ik_z z}, \tag{1.76}
 \end{aligned}$$

where  $Q_0$ ,  $Q_1$ , and  $Q_2$  are defined by Eqs. (1.57) and (1.68).

### 1.3.4 Application of the Driven Wall Boundary Condition

Substituting the roots given by Eqs. (1.53) and (1.54) into Eqs. (1.75) and (1.76), the solution for the components of the velocity fluctuation in a cylindrical tube are

$$w e^{-i(k_z z - \omega t)} = A_0 Q_0 - i A_1 k_z \omega \left( -\frac{ic^2}{\omega^2} + \frac{\gamma l_e^2}{2} \right) Q_1 - \frac{1}{2} i A_2 k_z l_e^2 \omega (\gamma - 1) Q_2, \tag{1.77}$$

and

$$ve^{-i(k_z z - \omega t)} = \frac{iA_0 k_z}{2i/l_v^2 - k_z^2} \frac{dQ_0}{dr} - A_1 \omega \left( -\frac{ic^2}{\omega^2} + \frac{\gamma l_e^2}{2} \right) \frac{dQ_1}{dr} - \frac{1}{2} A_2 l_e^2 \omega (\gamma - 1) \frac{dQ_2}{dr}. \quad (1.78)$$

The goal is to determine  $A_0$ ,  $A_1$ , and  $A_2$  given specific boundary conditions.

Consider the walls of the tube to be driven at a constant driving velocity  $V_0$  with wave number  $k_w$  and frequency  $\omega$ . Also assume there is no slipping at the wall. The boundary conditions at the driven wall are then

$$v|_{r=a} = V_0 e^{i(k_w z - \omega t)}, \quad (1.79)$$

$$w|_{r=a} = 0, \quad (1.80)$$

$$T|_{r=a} = 0, \quad (1.81)$$

where it has been assumed that the wall is infinitely more conducting than the fluid, so the temperature of the wall can be considered constant. Applying these to Eqs. (1.77) and (1.78) yields

$$0 = A_0 Q_0(a) - iA_1 k_z \omega \left( -\frac{ic^2}{\omega^2} + \frac{\gamma l_e^2}{2} \right) Q_1(a) - \frac{1}{2} iA_2 k_z l_e^2 \omega (\gamma - 1) Q_2(a), \quad (1.82)$$

and

$$\begin{aligned} V_0 e^{i(k_w z - \omega t)} e^{-(ik_z z - i\omega t)} &= \left. \frac{iA_0 k_z}{-k_z^2 + 2i/l_v^2} \frac{dQ_0}{dr} \right|_{r=a} - A_1 \omega \left( -\frac{ic^2}{\omega^2} + \frac{\gamma l_e^2}{2} \right) \left. \frac{dQ_1}{dr} \right|_{r=a} \\ &\quad - \frac{1}{2} A_2 l_e^2 \omega (\gamma - 1) \left. \frac{dQ_2}{dr} \right|_{r=a}. \end{aligned} \quad (1.83)$$

This boundary condition requires that the axial wave number  $k_z$  be equal to the axial wall wave number  $k_w$ .  $A_0$ ,  $A_1$ , and  $A_2$  are obtained by combining Eqs. (1.82), (1.83), and (1.48) evaluated at  $r = a$ . Substituting the results into Eqs. (1.77) and (1.78) yields

$$\begin{aligned}
 \frac{w}{V_0} D &= i(ka)^2 \left( \frac{c}{c_w} \right) \left[ -\frac{i}{(ka)^2} + \frac{1}{2} \left( \frac{l_e}{a} \right)^2 \right] \\
 &\quad \times \frac{J_0 \left( kr \sqrt{2i/(kl_v)^2 - (c/c_w)^2} \right)}{J_0 \left( ka \sqrt{2i/(kl_v)^2 - (c/c_w)^2} \right)} \\
 &- i(ka)^2 \left( \frac{c}{c_w} \right) \left[ -\frac{i}{(ka)^2} + \frac{\gamma}{2} \left( \frac{l_e}{a} \right)^2 \right] \\
 &\quad \times \frac{J_0 \left( kr \sqrt{1 - (c/c_w)^2} \right)}{J_0 \left( ka \sqrt{1 - (c/c_w)^2} \right)} \\
 &+ i(ka)^2 \left( \frac{c}{c_w} \right) \frac{\gamma - 1}{2} \left( \frac{l_e}{a} \right)^2 \\
 &\quad \times \frac{J_0 \left( kr \sqrt{2i/(kl_e)^2 - (c/c_w)^2} \right)}{J_0 \left( ka \sqrt{2i/(kl_e)^2 - (c/c_w)^2} \right)}, \tag{1.84}
 \end{aligned}$$

for the axial particle velocity, and

$$\begin{aligned}
 \frac{v}{V_0} D &= (ka)^4 \left( \frac{c}{c_w} \right)^2 \sqrt{\frac{2i}{(kl_v)^2}} - \left( \frac{c}{c_w} \right)^2 \left[ \frac{-i/(ka)^2 + 2(l_e/2a)^2}{2i(a/l_v)^2 - (kac/c_w)^2} \right] \\
 &\quad \times \frac{J_1 \left( kr \sqrt{2i/(kl_v)^2 - (c/c_w)^2} \right)}{J_0 \left( ka \sqrt{2i/(kl_v)^2 - (c/c_w)^2} \right)} \\
 &+ (ka)^2 \sqrt{1 - \left( \frac{c}{c_w} \right)^2} \left[ -\frac{i}{(ka)^2} + \frac{\gamma}{2} \left( \frac{l_e}{a} \right)^2 \right]
 \end{aligned}$$

$$\begin{aligned}
& \times \frac{J_1 \left( kr \sqrt{1 - (c/c_w)^2} \right)}{J_0 \left( ka \sqrt{1 - (c/c_w)^2} \right)} \\
- & (ka)^2 \left( \frac{l_e}{a} \right)^2 \frac{\gamma - 1}{2} \sqrt{\frac{2i}{(kl_e)^2} - \left( \frac{c}{c_w} \right)^2} \\
& \times \frac{J_1 \left( kr \sqrt{2i/(kl_e)^2 - (c/c_w)^2} \right)}{J_0 \left( ka \sqrt{2i/(kl_e)^2 - (c/c_w)^2} \right)}
\end{aligned} \tag{1.85}$$

for the radial particle velocity where  $D$  is defined as

$$\begin{aligned}
D \equiv & (ka)^4 \left( \frac{c}{c_w} \right)^2 \sqrt{\frac{2i}{(kl_v)^2} - \left( \frac{c}{c_w} \right)^2} \left[ \frac{-i/(ka)^2 + 2(l_e/2a)^2}{2i(a/l_v)^2 - (kac/c_w)^2} \right] \\
& \times \frac{J_1 \left( ka \sqrt{2i/(kl_v)^2 - (c/c_w)^2} \right)}{J_0 \left( ka \sqrt{2i/(kl_v)^2 - (c/c_w)^2} \right)} \\
+ & (ka)^2 \sqrt{1 - \left( \frac{c}{c_w} \right)^2} \left[ -\frac{i}{(ka)^2} + \frac{\gamma}{2} \left( \frac{l_e}{a} \right)^2 \right] \\
& \times \frac{J_1 \left( ka \sqrt{1 - (c/c_w)^2} \right)}{J_0 \left( ka \sqrt{1 - (c/c_w)^2} \right)} \\
- & (ka)^2 \left( \frac{l_e}{a} \right)^2 \frac{\gamma - 1}{2} \sqrt{\frac{2i}{(kl_e)^2} - \left( \frac{c}{c_w} \right)^2} \\
& \times \frac{J_1 \left( ka \sqrt{2i/(kl_e)^2 - (c/c_w)^2} \right)}{J_0 \left( ka \sqrt{2i/(kl_e)^2 - (c/c_w)^2} \right)}.
\end{aligned} \tag{1.86}$$

These equations have been written in terms of the wave number  $k$  in the infinite medium and the wave velocity  $c_w$  in the wall given by Eqs. (1.19) and (1.20), respectively. Each term in Eqs. (1.84) and (1.85) corresponds to a mode of propagation determined by the nature of the root of the Bessel function. The first term is

the vorticity mode, the second term is the acoustic mode, and the third term is the entropy mode.

As a check, these equations should reduce to the results for the lossless fluid filled tube in Section 1.2. Letting  $l_e \rightarrow 0$  and  $l_v \rightarrow 0$  in Eqs. (1.84) and (1.86), the resulting solution for  $v/V_0$  is

$$\lim_{l_v, l_e \rightarrow 0} \frac{v}{V_0} = \frac{J_1 \left( kr \sqrt{1 - (c/c_w)^2} \right)}{J_1 \left( ka \sqrt{1 - (c/c_w)^2} \right)}, \quad (1.87)$$

which is identical to Eq. (1.17) for the case of the lossless fluid.

The resulting solution for  $w/V_0$  is

$$\begin{aligned} \lim_{l_v, l_e \rightarrow 0} \frac{w}{V_0} &= \frac{i J_0 \left( ka \sqrt{1 - (c/c_w)^2} \right)}{J_1 \left( ka \sqrt{1 - (c/c_w)^2} \right) \sqrt{(c_w/c)^2 - 1}} \\ &\times \left[ \frac{J_0 \left( kr \sqrt{2i/(kl_v)^2 - (c/c_w)^2} \right)}{J_0 \left( ka \sqrt{2i/(kl_v)^2 - (c/c_w)^2} \right)} - \frac{J_0 \left( kr \sqrt{1 - (c/c_w)^2} \right)}{J_0 \left( ka \sqrt{1 - (c/c_w)^2} \right)} \right]. \end{aligned} \quad (1.88)$$

For a large argument, the Bessel function can be expressed as

$$J_0(\bar{x}) \approx \sqrt{\frac{2}{\pi \bar{x}}} \cos \left( \bar{x} - \frac{\pi}{4} \right). \quad (1.89)$$

Let  $\text{Im}(\bar{x}) > 0$ . Rewriting this equation in terms of real and complex components, it reduces to

$$J_0(\bar{x}) \approx \sqrt{\frac{1}{2\pi \bar{x}}} e^{-i(\text{Re}(\bar{x}) - \pi/4)} e^{\text{Im}(\bar{x})}. \quad (1.90)$$

Now,

$$\begin{aligned}
 \bar{x} &= kr \sqrt{\frac{2i}{(kl_v)^2} - \left(\frac{c}{c_w}\right)^2} \\
 &\approx kr \sqrt{\frac{2i}{(kl_v)^2}} \\
 &\approx \frac{r}{l_v} \sqrt{2i} \\
 &\approx \frac{r}{l_v} (1 + i),
 \end{aligned} \tag{1.91}$$

therefore, the first term in the brackets in Eq. (1.88) can be written as

$$\frac{J_0 \left( kr \sqrt{2i/(kl_v)^2} - (c/c_w)^2 \right)}{J_0 \left( ka \sqrt{2i/(kl_v)^2} - (c/c_w)^2 \right)} \approx \sqrt{\frac{a}{r}} e^{-i(r-a)/l_v} e^{(r-a)/l_v}. \tag{1.92}$$

Since  $r < a$ , then  $(r - a) < 0$ , which will drive the exponent to zero as  $l_v \rightarrow 0$ . This will result in Eq. (1.88) becoming

$$\lim_{l_v, l_e \rightarrow 0} \frac{w}{V_0} = \frac{-i}{\sqrt{(c_w/c)^2 - 1}} \frac{J_0 \left( kr \sqrt{1 - (c/c_w)^2} \right)}{J_1 \left( ka \sqrt{1 - (c/c_w)^2} \right)} \tag{1.93}$$

which is identical to Eq. (1.18) for the case of the inviscid fluid except where  $r = a$ . In that case the bracketed term in Eq. (1.88) goes to zero so that the axial velocity goes to zero at the wall as required by the viscous boundary condition.

Table 1.1: Thermal properties are for air at 27°C at atmospheric pressure. (Source: "Table of Thermal Properties of Gases," National Bureau of Standards Circular 564, Issue Date: November 1; 1955.)

Parameter	Value
$\mu$ ( $\text{kg m}^{-1} \text{s}^{-1}$ )	$1.846 \times 10^{-5}$
$\kappa$ ( $\text{W m}^{-1} \text{K}^{-1}$ )	$2.624 \times 10^{-2}$
$\rho_0$ ( $\text{kg m}^{-3}$ )	1.177
$C_v$ ( $\text{J kg}^{-1} \text{K}^{-1}$ )	718.812
$\gamma$	1.4
$c$ ( $\text{m s}^{-1}$ )	347.14
$a$ (cm)	1.0

### 1.3.5 Theoretical Results for an Air Filled Tube

In order to calculate velocities from Eqs. (1.84) and (1.85) it is necessary to specify the thermal properties of the fluid as well as the radius. The values used for these calculations are given in Table 1.1. The size of the vorticity and entropy skin depths corresponding to the given values are  $l_v = (2.13 \times 10^{-3} \text{ m Hz}^{1/2})f^{-1/2}$  and  $l_e = (2.54 \times 10^{-3} \text{ m Hz}^{1/2})f^{-1/2}$  respectively.

The normalized velocity amplitude of the system as a function of the dimensionless wave number  $ka$  and propagation speed of the wave in the wall  $c_w/c$  is shown in Fig. 1.8 for the case of the radial velocity and Fig. 1.9 for the case of the axial velocity. Both are for  $r = a/2$ . These plots are similar to those of Section 1.2.2 except for the radial velocity going to zero when  $c_w = c$ . This can be seen from a closer examination of Eqs. (1.85) and (1.86). Setting  $c_w = c$  yields  $D \neq 0$  for all values of  $ka$  (see Fig. 1.10), so that the acoustic term of  $v$  is zero. Therefore, only the vorticity and entropy modes contribute to the radial velocity, which means that

Table 1.2: Outline of velocity amplitude figures.

Variables			Figure
Independent(s)	Constant	Dependent	
$ka, c_w/c$	$r = a/2$	$v$	1.8
		$w$	1.9
		$w$ (acoustic)	1.11
		$v$ (acoustic)	1.12
$r/a, c_w/c$	$ka = 1$	$v$ (acoustic)	1.13
		$v$ (vorticity)	1.14
		$v$ (entropy)	1.15
		$v$	1.16
		$w$ (acoustic)	1.18
		$w$ (vorticity)	1.19
		$w$ (entropy)	1.20
		$w$	1.21
	$ka = 8$	$v$	1.17
		$w$	1.22

the total velocity is negligible compared to the radial amplitude of the wall. Note also that the velocity amplitude when the tube is driven with a frequency and wave number corresponding to a propagation mode in the rigid tube is no longer infinite, as for the case of the inviscid fluid filled tube, but is finite and very large.

Inside the boundary layer when  $c_w = c$ , although the acoustic mode and entropy mode are coupled, the amplitude of the entropy mode is non-zero while the acoustic mode has zero amplitude. A closer examination of the acoustic mode is shown in Figs. 1.11 and 1.12 where the axial and radial velocities for  $r = a/2$  are shown. Curves for a lossless fluid, air, and water are shown for comparison. For the case of the axial velocity, the increased effect of viscosity not only lowers the maximum amplitude, but shifts the position of the peak along the curve of the inviscid fluid.

The result is that the peak actually occurs for  $c_w < c$ . For the case of the radial velocity, the amplitude increases above the value for the lossless fluid for  $c_w < c$  before dropping to zero. For values of  $c_w > c$ , the amplitude increases asymptotically to approach the value for the lossless fluid.

The radial velocities of the three modes of propagation are shown in Figs. 1.13–1.15, and the total velocity for  $ka = 1$  and  $ka = 8$  is shown in Figs. 1.16 and 1.17 for an air filled tube at atmospheric pressure. Corresponding figures for the axial velocities are shown in Figs. 1.18–1.22. (See Table 1.2 for an outline of all the velocity amplitude plots shown in this section.) As expected, the viscous and entropy modes are confined within the boundary layer at the wall. In most circumstances the thickness of this layer is only a few molecular mean free paths. However, comparison of Figs. 1.6 and 1.13 for  $ka = 1$  (that is, below the cutoff frequency of the first order mode) indicates that in a viscous and thermally conducting fluid, the radial motion of the driven wall excites radial motion in the thermal and viscous waves and leaves the acoustic wave in the body of the gas a plane wave without a radial component.

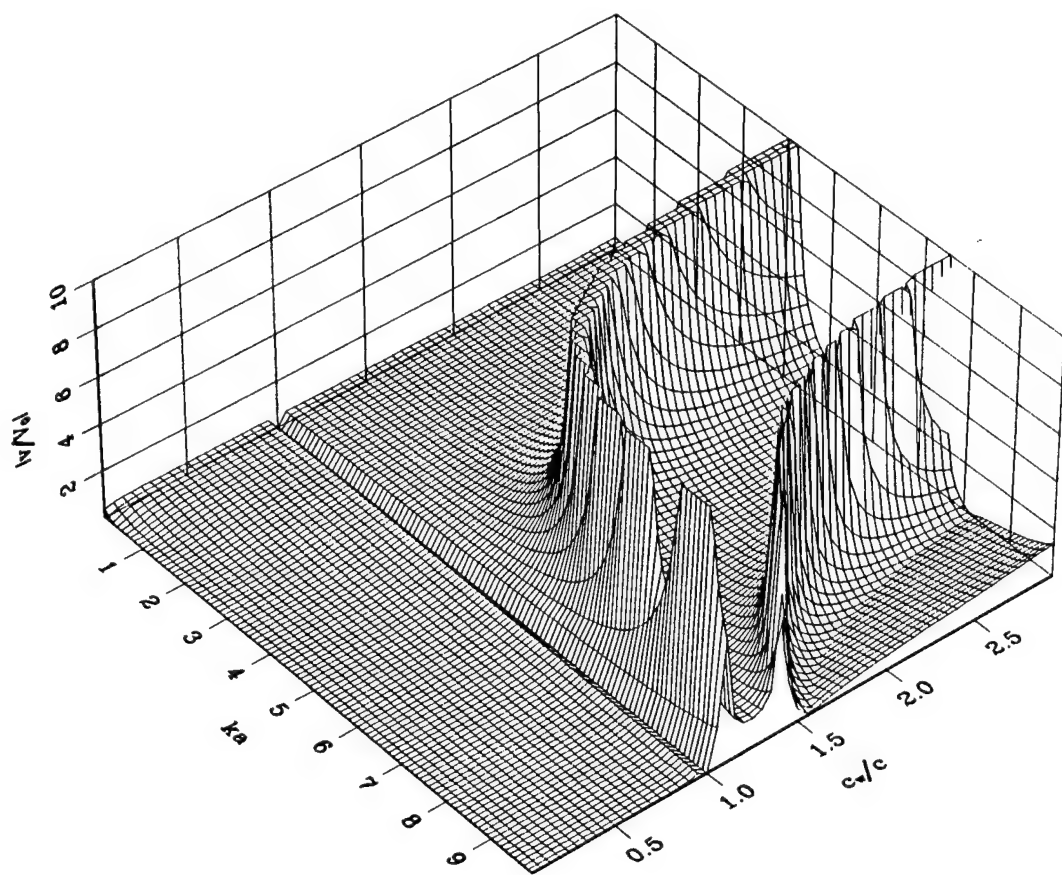


Figure 1.8: Normalized radial velocity amplitude as a function of the dimensionless wave number  $ka$  and propagation speed  $c_w/c$  in an air filled tube. Plot made for  $r = a/2$ .

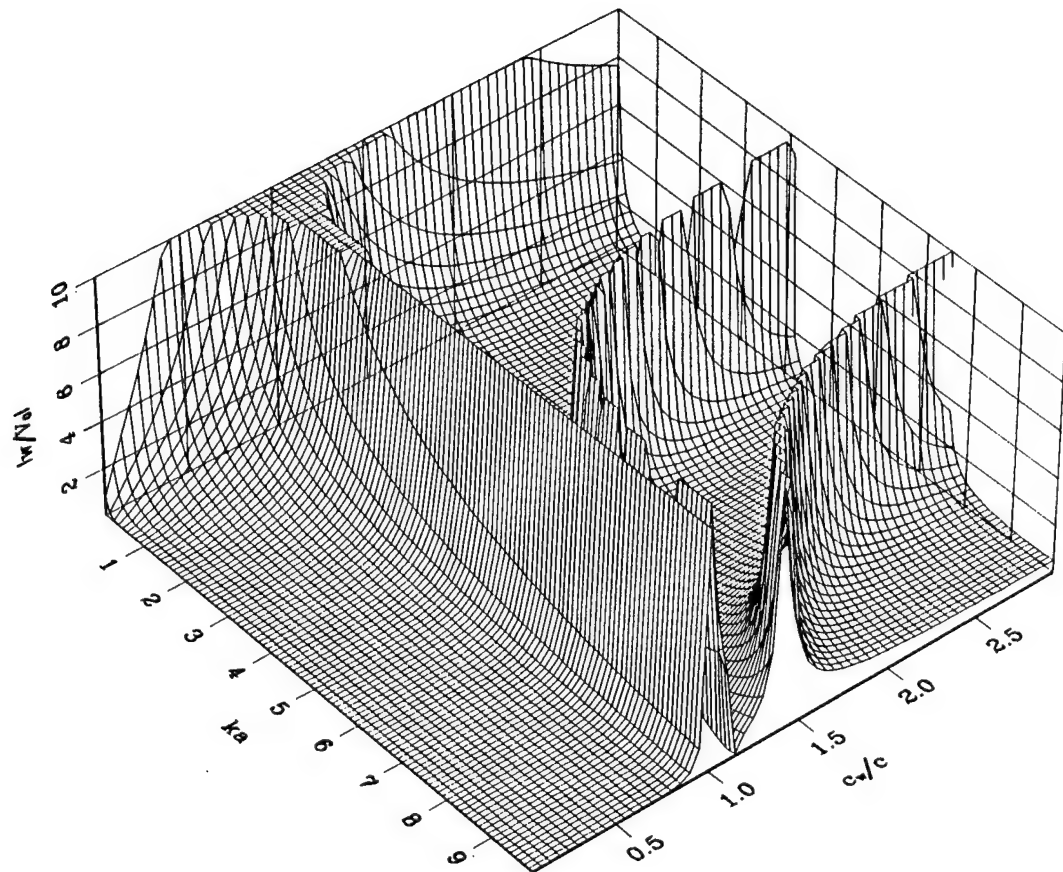


Figure 1.9: Normalized axial velocity amplitude as a function of the dimensionless wave number  $ka$  and propagation speed  $c_w/c$  in an air filled tube. Plot made for  $r = a/2$ .

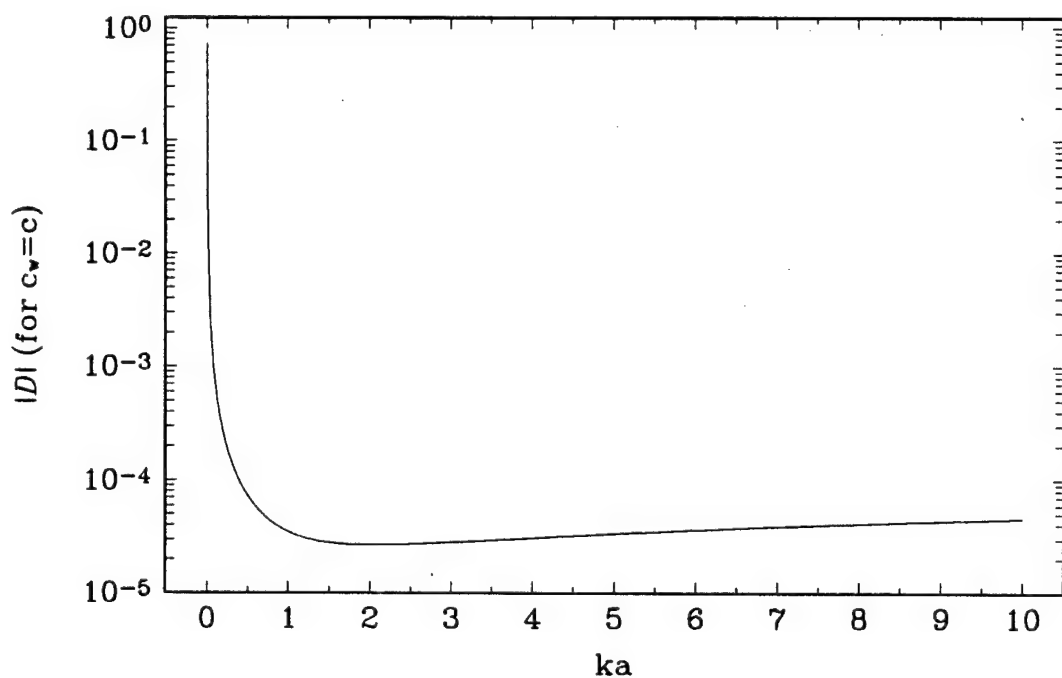


Figure 1.10: Plot of the magnitude  $D$  given by Eq. (1.86) for  $c_w = c$  in an air filled tube.

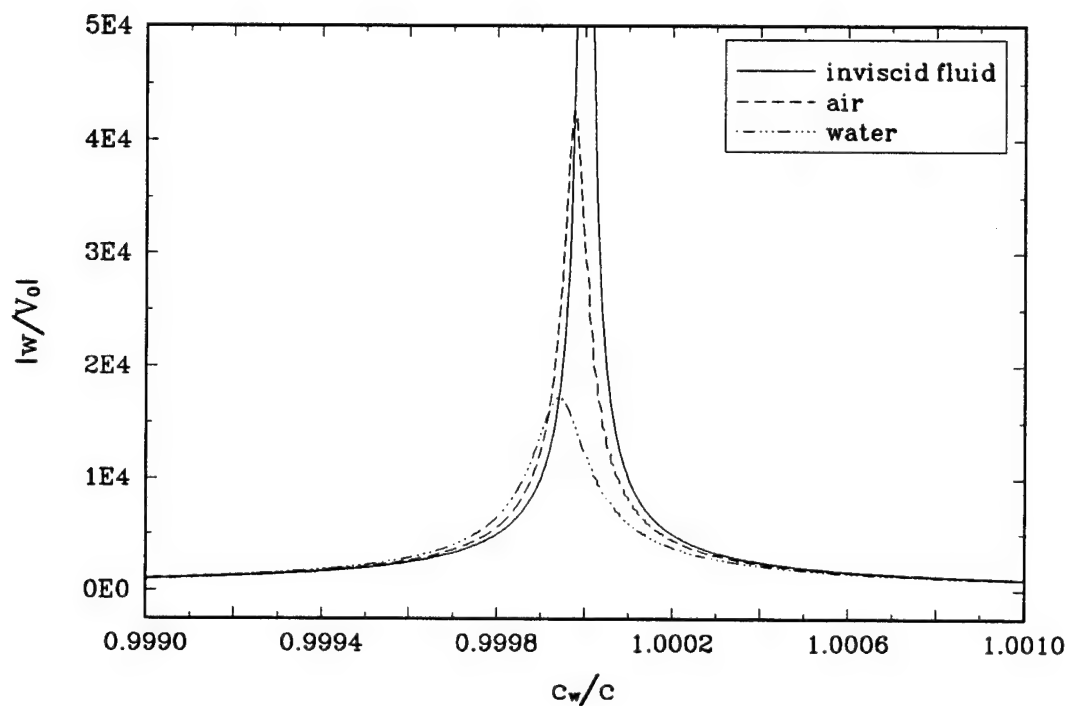


Figure 1.11: Normalized acoustic mode radial velocity amplitude for tube filled with various types of fluid. Plot made for  $ka = 1$  and  $r = a/2$ .

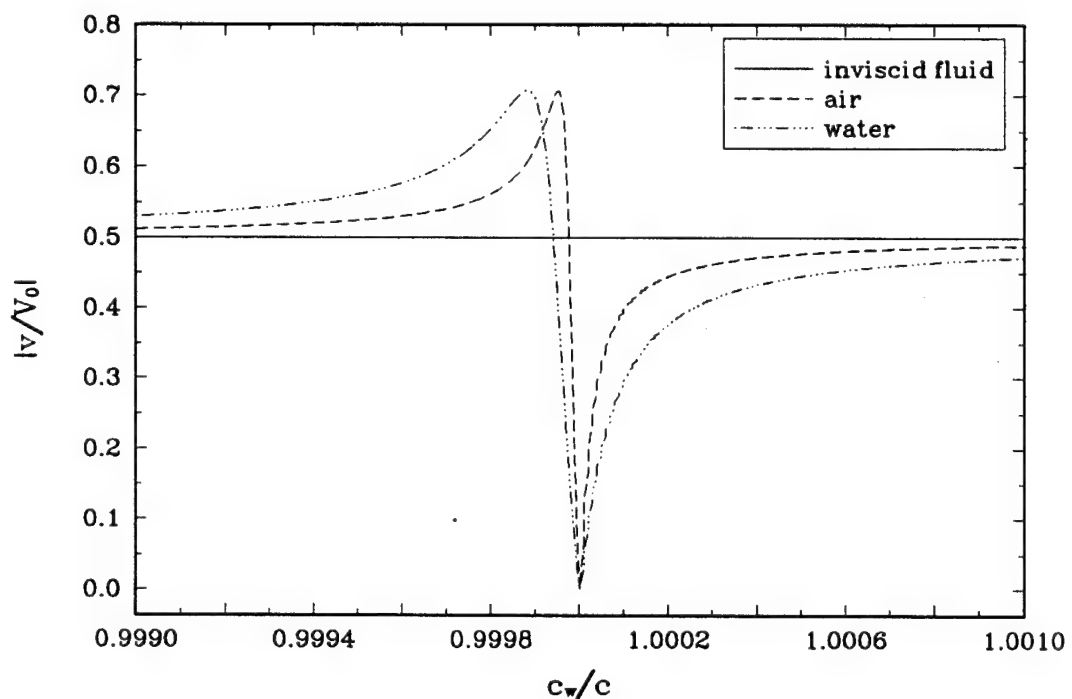


Figure 1.12: Normalized acoustic mode radial velocity amplitude for tube filled with various types of fluid. Plot made for  $ka = 1$  and  $r = a/2$ .

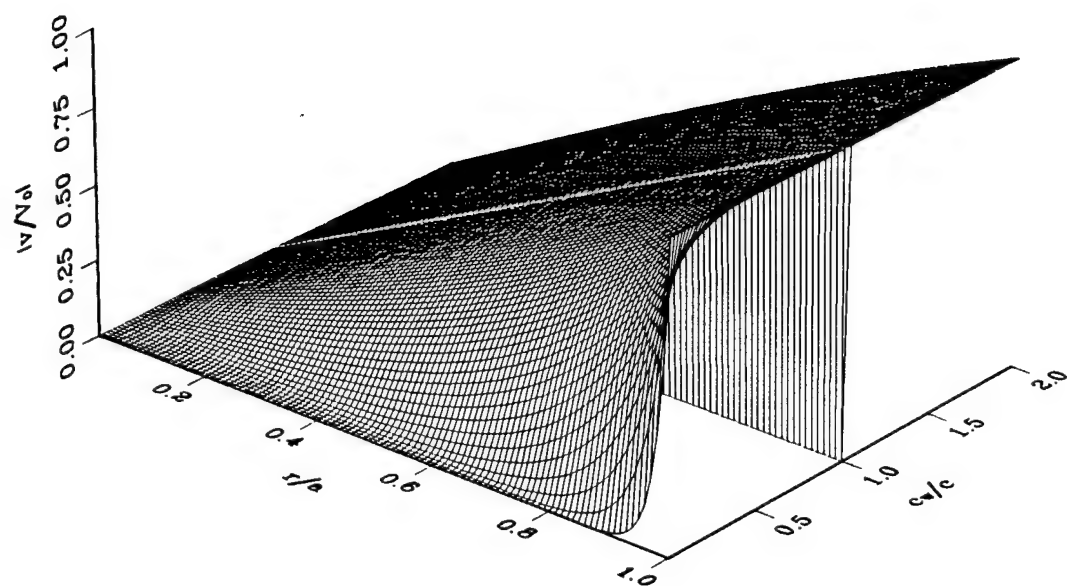


Figure 1.13: Normalized radial velocity amplitude of the acoustic mode as a function of the dimensionless radial position  $r/a$  and propagation speed  $c_w/c$  in an air filled tube. Plot made for  $ka = 1$ . Note that at  $c_w = c$  the amplitude of motion is zero for all values of  $r \leq a$ .

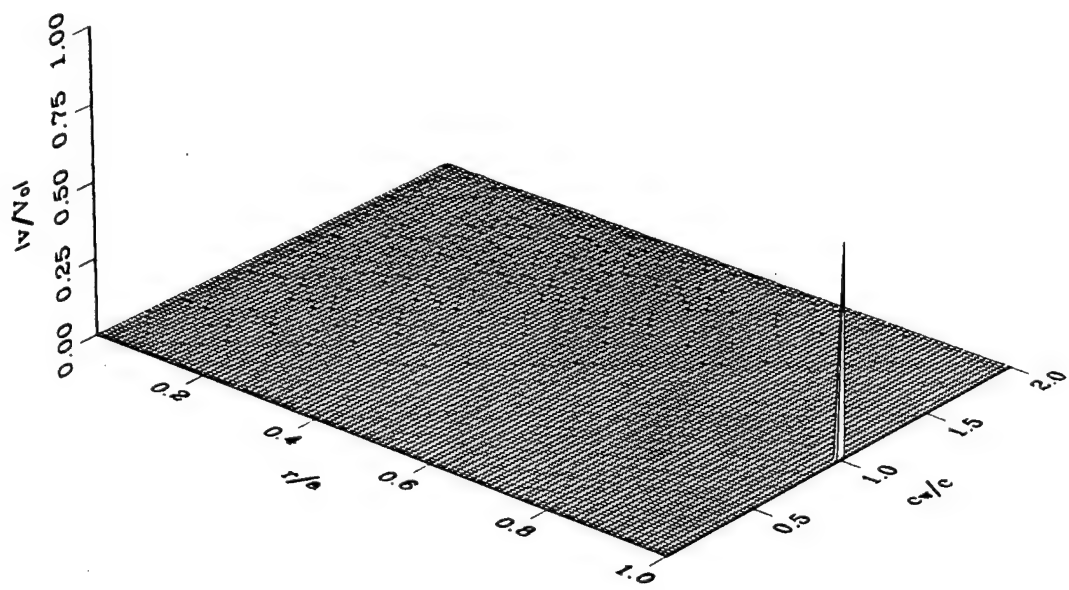


Figure 1.14: Normalized radial velocity amplitude of the vorticity mode as a function of the dimensionless radial position  $r/a$  and propagation speed  $c_w/c$  in an air filled tube. Plot made for  $ka = 1$ .

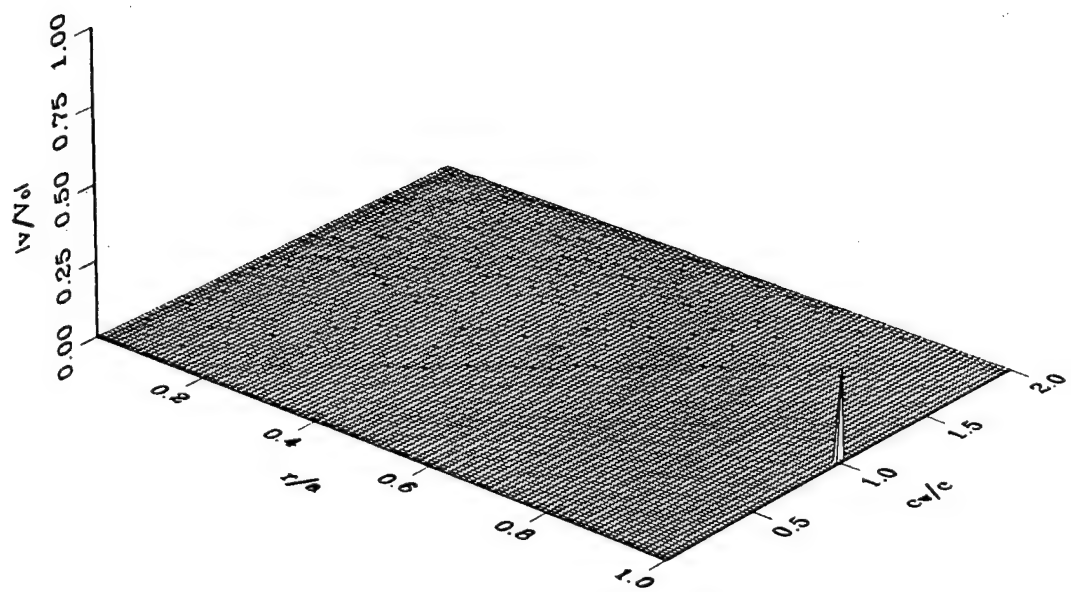


Figure 1.15: Normalized radial velocity amplitude of the entropy mode as a function of the dimensionless radial position  $r/a$  and propagation speed  $c_w/c$  in an air filled tube. Plot made for  $ka = 1$ .

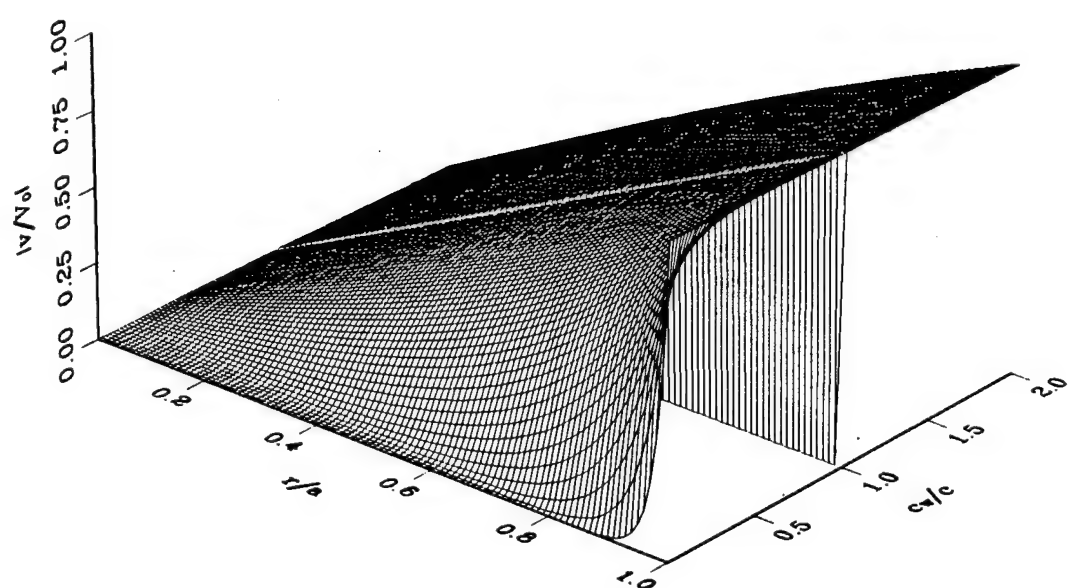


Figure 1.16: Normalized total radial velocity amplitude as a function of the dimensionless radial position  $r/a$  and propagation speed  $c_w/c$  in an air filled tube. Plot made for  $ka = 1$ . Note that for  $c_w = c$  the amplitude at the wall is such that  $|v/V_0| = 1$  as required by the boundary condition.

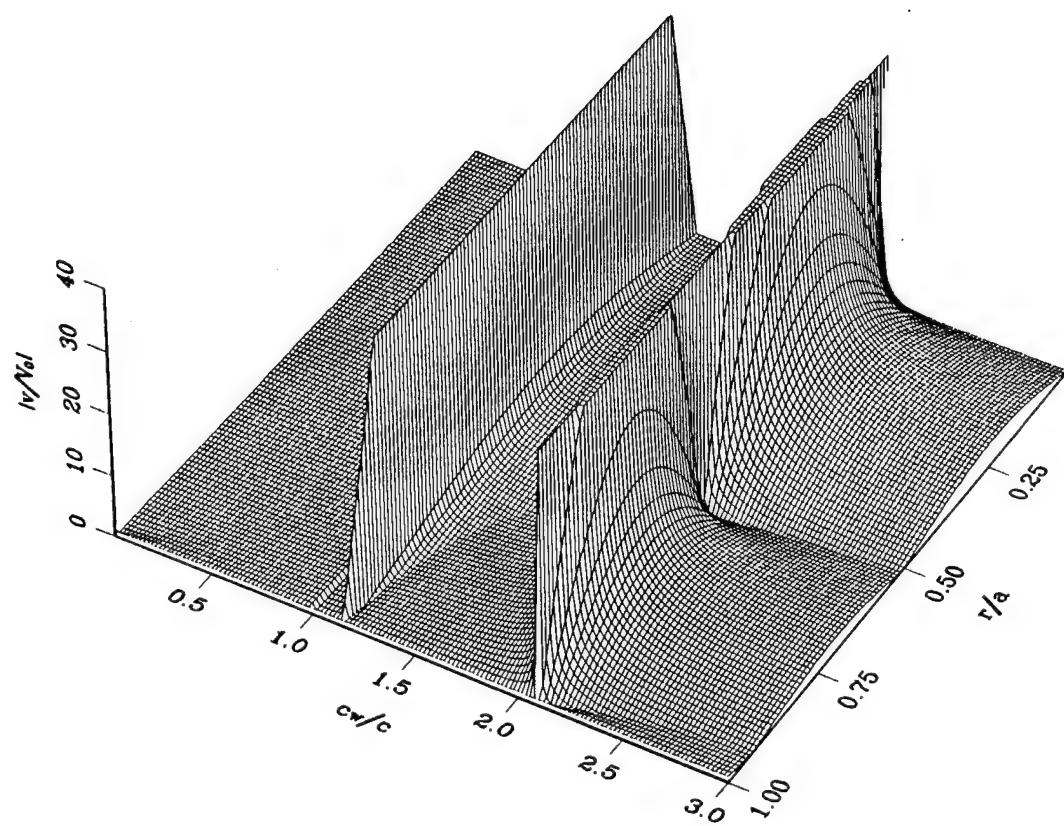


Figure 1.17: Normalized total radial velocity amplitude as a function of the dimensionless radial position  $r/a$  and propagation speed  $c_w/c$  in an air filled tube. Plot made for  $ka = 8$ .

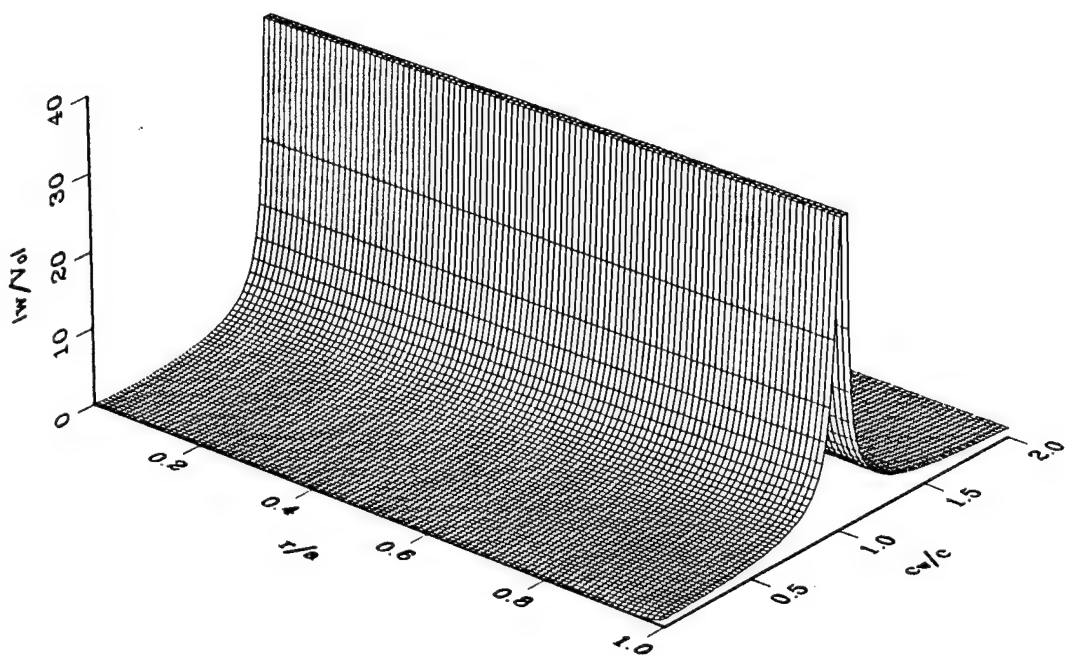


Figure 1.18: Normalized axial velocity amplitude of the acoustic mode as a function of the dimensionless radial position  $r/a$  and propagation speed  $c_w/c$  in an air filled tube. Plot made for  $ka = 1$ .

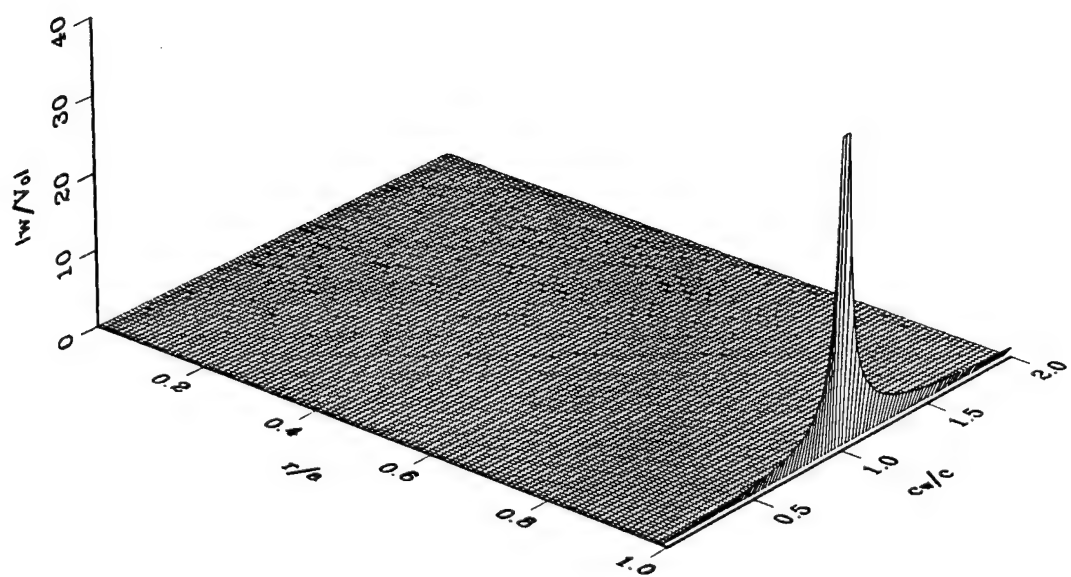


Figure 1.19: Normalized axial velocity amplitude of the vorticity mode as a function of the dimensionless radial position  $r/a$  and propagation speed  $c_w/c$  in an air filled tube. Plot made for  $ka = 1$ .

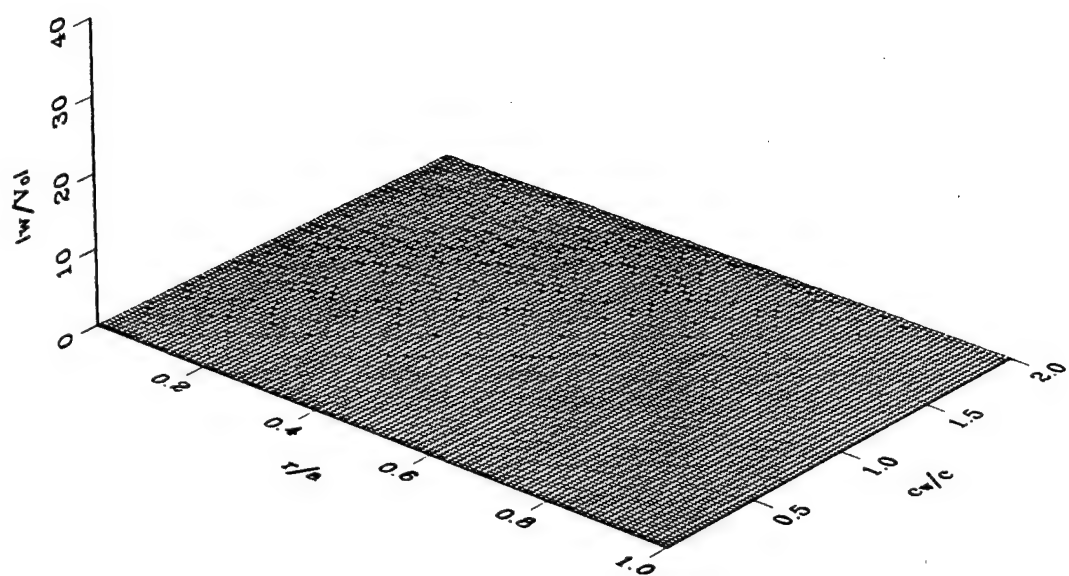


Figure 1.20: Normalized axial velocity amplitude of the entropy mode as a function of the dimensionless radial position  $r/a$  and propagation speed  $c_w/c$  in an air filled tube. Plot made for  $ka = 1$ .

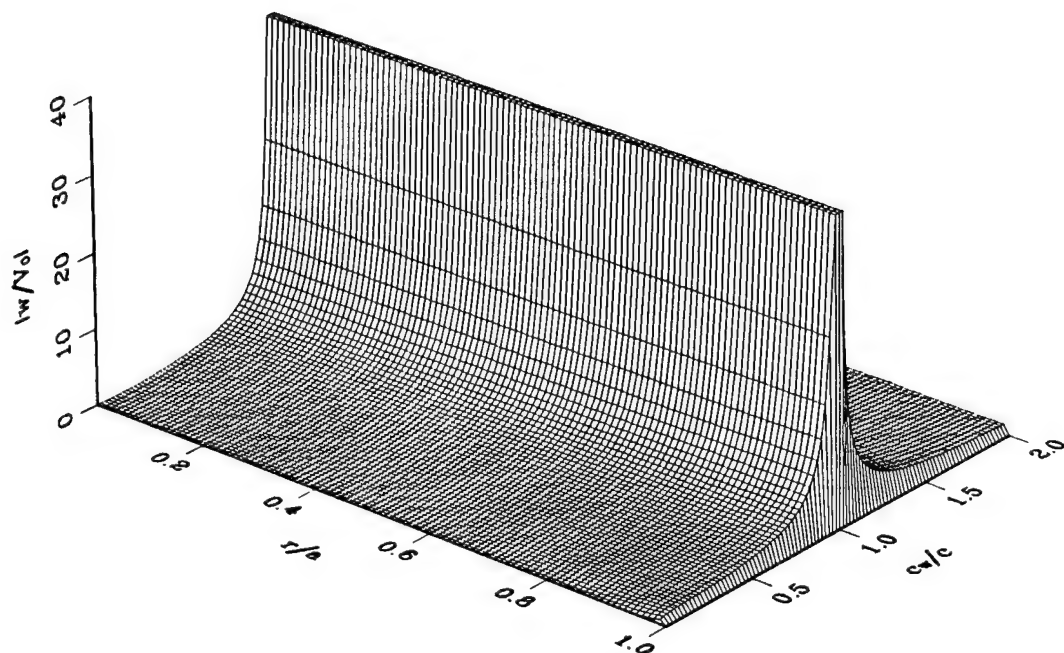


Figure 1.21: Normalized total axial velocity amplitude as a function of the dimensionless radial position  $r/a$  and propagation speed  $c_w/c$  in an air filled tube. Plot made for  $ka = 1$ .

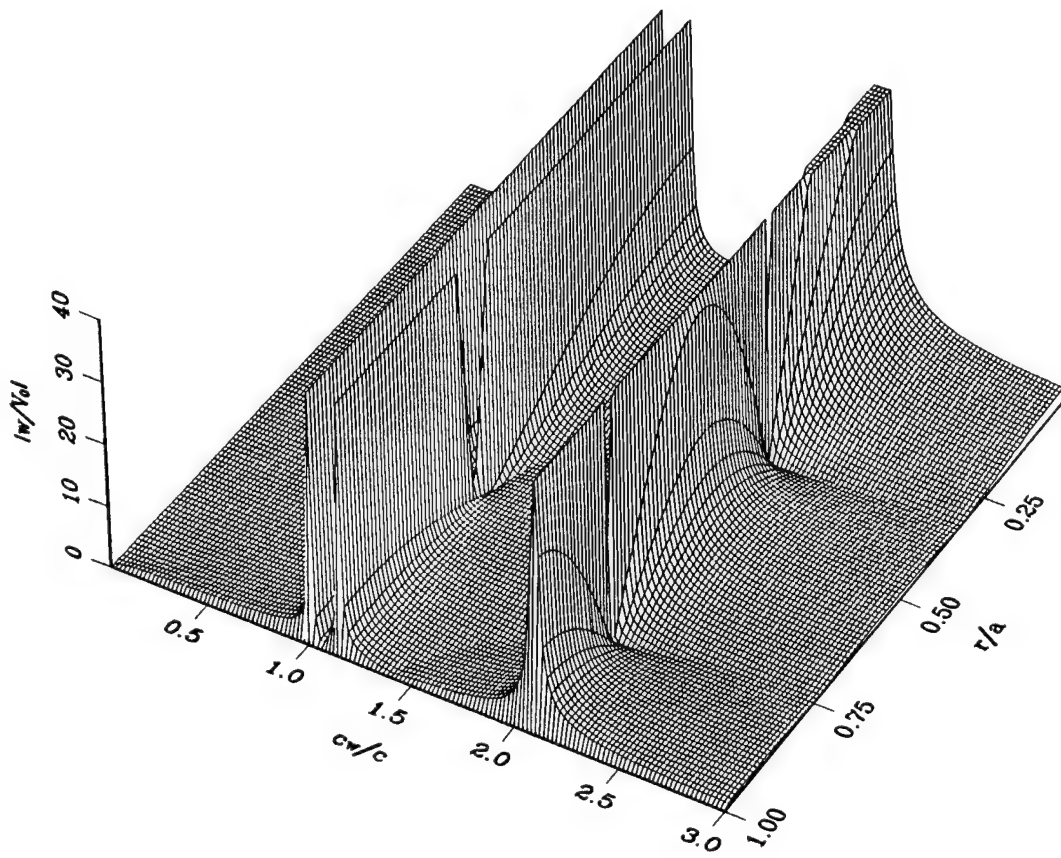


Figure 1.22: Normalized total axial velocity amplitude as a function of the dimensionless radial position  $r/a$  and propagation speed  $c_w/c$  in an air filled tube. Plot made for  $ka = 1$ .

## 1.4 Chapter Summary

In this chapter, the solution for sound propagation in a cylindrical driven wall tube with a given wave number and phase velocity has been presented. The cases of a lossless fluid and a viscous and thermally conducting fluid are considered. It has been shown that the latter case is in agreement with the former when the viscosity and thermal conductivity are equal to zero.

The results of these solutions show that the behavior of the sound particle velocity, in most respects, are very similar for both cases, except when  $c_w = c$ . When such a driving condition exists, the radial velocity of the acoustic mode is no longer finite, as in the case of the ideal fluid, but is zero throughout the tube. At the same time, the axial velocity is no longer infinite, as in the case of the ideal fluid, but is finite with an amplitude that depends on the value of viscosity and thermal conductivity of the fluid medium.

## Chapter 2

# Theory of the Toroidal Waveguide

In Chapter 1 the propagation of sound in an infinitely long straight tube has been considered. Experimentally, such a system can only be treated approximately, that is, it is not possible to build an infinitely long tube. It is possible, however, to construct a toroidal waveguide so that the effective path length over which the sound propagates is infinite.

Previous work dealing with sound propagation in curved tubes have considered only the case of rigid walls [29–33,37] and porous walls [35,36]. In the present work, the case of a toroid with rigid walls will first be considered, then the case of one with driven walls. It will be shown that, as for the cylindrical tube in Chapter 1, the solution for the rigid wall case will give some insight to the driven wall solution.

The geometry considered throughout this chapter is that of a toroidal duct with a rectangular cross-section. Let the toroid have an inside radius of  $a$  and an outside radius  $b$  as shown in Fig. 2.1. The height of the toroid is  $z = h$  with the base assumed to be in the  $x-y$  plane. Solutions will be sought in the form of waves traveling in the

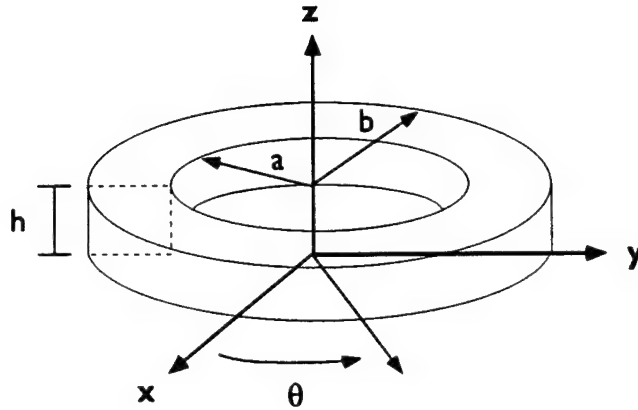


Figure 2.1: The Toroidal Waveguide.

azimuthal direction. The solution that will be used for the velocity potential derived in Section 1.1 is

$$\Phi = [A_r J_m(k_r r) + B_r Y_m(k_r r)] [A_z \cos(k_z z) + B_z \sin(k_z z)] e^{i(m\theta - \omega t)}. \quad (2.1)$$

In general, it is required that  $\Phi(r, \theta, z, t) = \Phi(r, \theta + 2\pi, z, t)$ . This requires that  $m$  be an integer. Because the propagation of sound is defined to be along  $\theta$ , it is convenient to think of  $m$  as analogous to a wave number. Following the convention of Krasnushkin [40],  $m$  will be referred to as the *angular wave number*. Because the phase of the velocity potential is given by  $\phi = m\theta - \omega t$ , the constant angular phase velocity  $(d\theta/dt)_{\phi=\text{constant}}$  is

$$\frac{d\theta}{dt} \equiv \Omega_m = \frac{\omega}{m}. \quad (2.2)$$

## 2.1 General Theory for the Lossless Toroid

First the general theory for sound propagation in a lossless fluid filled toroid with rigid walls will be developed, then the theory for driven walls will be developed. For the case of the driven wall toroid, an expression for the velocity potential in terms of an arbitrary function  $f(\theta)$  will be used so that any desired driving condition may be treated.

### 2.1.1 Rigid Wall Condition

In a toroid with rigid walls, the normal component of the fluid particle velocity is zero at the walls, i.e.,

$$\frac{\partial \Phi_m}{\partial z} \Big|_{z=0} = \frac{\partial \Phi_m}{\partial z} \Big|_{z=h} = 0, \quad (2.3)$$

$$\frac{\partial \Phi_m}{\partial r} \Big|_{r=a} = \frac{\partial \Phi_m}{\partial r} \Big|_{r=b} = 0, \quad (2.4)$$

for a given value of angular wave number  $m$ . Using Eq. (2.1) with these boundary conditions yields

$$B_z = 0, \quad k_z = \frac{n\pi}{h} \quad (n = 0, \pm 1, \pm 2 \dots), \quad (2.5)$$

and

$$A_m J'_m(k_r a) + B_m Y'_m(k_r a) = 0, \quad (2.6)$$

$$A_m J'_m(k_r b) + B_m Y'_m(k_r b) = 0. \quad (2.7)$$

Non-trivial solutions for  $A_m$  and  $B_m$  occur only when the determinant of the

coefficients is equal to zero, that is

$$J'_m(k_r a)Y'_m(k_r b) - J'_m(k_r b)Y'_m(k_r a) = 0. \quad (2.8)$$

Now define

$$\beta \equiv k_r a \quad (2.9)$$

so that

$$J'_m(\beta)Y'_m(\beta b/a) - J'_m(\beta b/a)Y'_m(\beta) = 0. \quad (2.10)$$

The solution to this equation is then

$$\beta = \beta_{mp}, \quad (2.11)$$

where  $\beta_{mp}$  is the  $p$ th root of Eq. (2.10) for a given  $m$ . From Eq. (1.8),

$$\omega_{mnp} = c \sqrt{\left(\frac{\beta_{mp}}{a}\right)^2 + \left(\frac{n\pi}{h}\right)^2}, \quad (2.12)$$

where  $\omega_{mnp}$  are the characteristic (or normal mode) frequencies.

Equation (2.11) may be used to solve for the ratio of  $B_m$  to  $A_m$  given by Eq. (2.6). Substituting this result and Eq. (2.5) into Eq. (2.1), yields a general solution for the velocity potential,

$$\Phi = \sum_{m=-\infty}^{\infty} \sum_{n=-\infty}^{\infty} \sum_{p=-\infty}^{\infty} A_{mnp} \left[ J_m \left( \frac{\beta_{mp} r}{a} \right) - Y_m \left( \frac{\beta_{mp} r}{a} \right) \frac{J'_m(\beta_{mp})}{Y'_m(\beta_{mp})} \right] \times \cos \left( \frac{n\pi z}{h} \right) e^{i(m\theta - \omega t)}. \quad (2.13)$$

A similar result was derived by Rostafinski [31] and Grigor'yan [33].

Now consider Eq. (2.10) for the case of a toroid whose width is much less than its radius, i.e.,

$$\frac{b}{a} = 1 + \epsilon, \quad 0 < \epsilon \ll 1, \quad (2.14)$$

so that

$$J'_m(\beta)Y'_m(\beta + \epsilon\beta) - J'_m(\beta + \epsilon\beta)Y'_m(\beta) = 0. \quad (2.15)$$

Expanding the Bessel functions for  $\beta\epsilon \ll 1$  in a Taylor series expansion yields

$$\begin{aligned} 0 &= J'_m(\beta)Y''_m(\beta) - J''_m(\beta)Y'_m(\beta) \\ &+ \frac{\epsilon\beta}{2} [J'_m(\beta)Y'''_m(\beta) - J'''_m(\beta)Y'_m(\beta)] \\ &+ \mathcal{O}(\beta^2\epsilon^2). \end{aligned} \quad (2.16)$$

Using the following identities for the difference of the products of Bessel and Neumann function derivatives [41],

$$J'_m(x)Y''_m(x) - J''_m(x)Y'_m(x) = \frac{2}{\pi x} \left(1 - \frac{m^2}{x^2}\right), \quad (2.17)$$

$$J'_m(x)Y'''_m(x) - J'''_m(x)Y'_m(x) = \frac{2}{\pi x^2} \left(\frac{3m^2}{x^2} - 1\right), \quad (2.18)$$

in Eq. (2.16) yields

$$\beta = m\sqrt{\frac{2-3\epsilon}{2-\epsilon}}, \quad (2.19)$$

or from Eq. (2.12),

$$\omega_{mn} = c\sqrt{\left(\frac{m}{a}\right)^2 \left(\frac{2-3\epsilon}{2-\epsilon}\right) + \left(\frac{n\pi}{h}\right)^2}. \quad (2.20)$$

Consider the case for  $n = 0$ , i.e., no variation of wave properties in the  $z$  direction, so that

$$\omega_m = \frac{mc}{a} \sqrt{\frac{2-3\epsilon}{2-\epsilon}}. \quad (2.21)$$

Expanding the square root for small  $\epsilon$

$$\begin{aligned} (2-\epsilon)^{-1/2} \times (2-3\epsilon)^{1/2} &= \frac{1}{2} \left[ 1 + \frac{1}{4}\epsilon + \mathcal{O}(\epsilon^2) \right] \times 2 \left[ 1 - \frac{3}{4}\epsilon + \mathcal{O}(\epsilon^2) \right] \\ &= 1 - \frac{1}{2}\epsilon + \mathcal{O}(\epsilon^2). \end{aligned} \quad (2.22)$$

Therefore to first order in  $\epsilon$ ,

$$\omega_m = \frac{mc}{a} \left( 1 - \frac{1}{2}\epsilon \right). \quad (2.23)$$

These characteristic frequencies correspond to those of integral wavelengths along the “center” circumference of the toroid. This can be demonstrated by considering a straight duct of length  $l = \pi(a+b)$  (the “center” circumference of the toroid). The frequencies of waves with an integral number of wavelengths over  $l$  are  $\omega = 2\pi mc/l$ . From Eq. (2.14),  $b = a(1+\epsilon)$ . Substituting this into  $l$ , the frequencies of waves that fit in this straight duct are

$$\begin{aligned} \omega &= mc \left( \frac{a+b}{2} \right)^{-1} \\ &= mc \left( \frac{a}{2} + \frac{a(1+\epsilon)}{2} \right)^{-1} \\ &= \frac{mc}{a} \left( 1 + \frac{1}{2}\epsilon \right)^{-1} \end{aligned}$$

$$\approx \frac{mc}{a} \left( 1 - \frac{1}{2}\epsilon \right), \quad (2.24)$$

which is identical to Eq. (2.23). Note that the similarity of the toroid to a straight duct requires that  $\beta\epsilon = k_r a\epsilon \ll 1$ , so that this approximation is only valid for wavelengths that are large compared to the width of the tube. Therefore in this limit, the shape of the bend has no effect on sound propagation. This result is the same as derived by Rostafinski [31], and even earlier by Lord Rayleigh [3] (Section 263).

### 2.1.2 The Driven Wall Condition

Let the outer and inner walls of the toroid now be driven with an angular dependent velocity function  $f(\theta)$  while the top and bottom walls are kept rigid (Fig. 2.2), i.e.,

$$\left. \frac{\partial \Phi_m}{\partial z} \right|_{z=0} = \left. \frac{\partial \Phi_m}{\partial z} \right|_{z=h} = 0, \quad (2.25)$$

$$\left. \frac{\partial \Phi_m}{\partial r} \right|_{r=a} = V_0 f(\theta) e^{-i\omega t}, \quad (2.26)$$

$$\left. \frac{\partial \Phi_m}{\partial r} \right|_{r=b} = -V_0 f(\theta) e^{-i\omega t}, \quad (2.27)$$

where  $V_0$  is the velocity amplitude of the wall. Note that the inner and outer walls move in opposite directions, as indicated by the minus sign in Eq. (2.26).

Equation (2.25) again yields the result for  $k_z$  given by Eq. (2.5). All driving conditions considered will be those with no  $z$  dependence, so that there will be no variation of wave properties in the  $z$  direction, i.e.,  $n = 0$ .

As stated earlier, a general solution in terms of  $\theta$  without any restrictions on the motion of the wall is desired. For this reason, it is convenient to write the  $\theta$  dependence

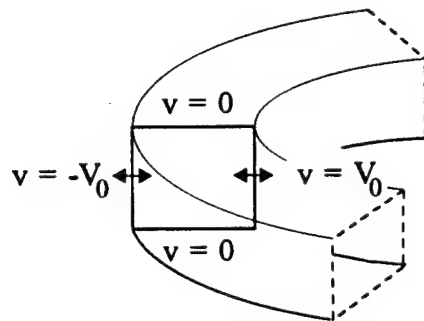


Figure 2.2: Toroid with inner and outer driven walls and upper and lower rigid walls.

of the driven boundary condition as the sum over all possible angular wave numbers in the wall by Fourier decomposing  $f(\theta)$ . Therefore,  $f(\theta)$  can be written as a Fourier sum,

$$f(\theta) = \sum_{l=-\infty}^{\infty} A_l e^{il\theta}, \quad (2.28)$$

where

$$A_l = \frac{1}{2\pi} \int_{-\pi}^{\pi} f(\theta') e^{-il\theta'} d\theta'. \quad (2.29)$$

All that is then required to solve for the velocity potential is an expression describing the driving wall in terms of  $\theta$ .

## 2.2 Application of Boundary Conditions: Delta Function Driver

### 2.2.1 Theory

Consider the case of a toroid with all rigid walls except for a single driving element located at  $\theta_d$ , so that

$$f(\theta) = \delta(\theta - \theta_d). \quad (2.30)$$

For convenience, the  $x-y$  axes will be oriented so that  $\theta_d = 0$ . When substituted into Eq. (2.29), the result is

$$A_l = \frac{1}{2\pi} \int_{-\pi}^{\pi} \delta(\theta') e^{-il\theta'} d\theta' = \frac{1}{2\pi}. \quad (2.31)$$

Equations (2.26) and (2.27) then become,

$$\left. \frac{\partial \Phi_m}{\partial r} \right|_{r=a} = \sum_{l=-\infty}^{\infty} \frac{V_0}{2\pi} e^{i(l\theta - \omega t)}, \quad (2.32)$$

$$\left. \frac{\partial \Phi_m}{\partial r} \right|_{r=b} = \sum_{l=-\infty}^{\infty} -\frac{V_0}{2\pi} e^{i(l\theta - \omega t)}. \quad (2.33)$$

Note that the amplitude of each angular wave number component will be the same. Each positive wave number has a corresponding negative wave number of the same amplitude. The result will therefore be a standing wave inside the toroid.

Using the general solution for the velocity potential, Eq. (2.1), in the above

(excluding the  $z$  dependence) yields,

$$\sum_{l=-\infty}^{\infty} \frac{V_0}{2\pi} e^{il\theta} = \sum_{m=-\infty}^{\infty} k_r [A_m J'_m(k_r a) + B_m Y'_m(k_r a)] e^{im\theta}, \quad (2.34)$$

$$\sum_{l=-\infty}^{\infty} -\frac{V_0}{2\pi} e^{il\theta} = \sum_{m=-\infty}^{\infty} k_r [A_m J'_m(k_r b) + B_m Y'_m(k_r b)] e^{im\theta}, \quad (2.35)$$

where  $k_r = \omega/c$ .

In order to solve for  $A_m$  and  $B_m$ , multiply both sides of Eqs. (2.34) and (2.35) by  $\exp(-ij\theta)$ , where  $j$  is an integer, and integrate over  $d\theta$  from  $-\pi$  to  $\pi$ . Integrating both sides over  $\theta$  results in Kronecker  $\delta$  functions  $\delta_{lj}$  and  $\delta_{mj}$  on the left and right sides respectively. The sums over  $m$  and  $l$  thus produce single terms in  $j$ . (Since  $j$  is just a dummy index, it will be replaced with  $m$  for convenience.) Equations (2.34) and (2.35) then become

$$\frac{V_0}{2\pi} = A_m k_r J'_m(k_r a) + B_m k_r Y'_m(k_r a), \quad (2.36)$$

$$-\frac{V_0}{2\pi} = A_m k_r J'_m(k_r b) + B_m k_r Y'_m(k_r b). \quad (2.37)$$

Solving for  $A_m$  and  $B_m$  yields,

$$A_m = \frac{V_0}{2\pi k_r \Delta_m} [Y'_m(k_r a) + Y'_m(k_r b)], \quad (2.38)$$

$$B_m = \frac{-V_0}{2\pi k_r \Delta_m} [J'_m(k_r a) + J'_m(k_r b)], \quad (2.39)$$

where

$$\Delta_m \equiv J'_m(k_r a) Y'_m(k_r b) - J'_m(k_r b) Y'_m(k_r a). \quad (2.40)$$

Comparison to Eq. (2.8) reveals that the frequencies that yield  $\Delta_m = 0$  are the characteristic frequencies of the rigid wall toroid,  $\omega_{mp}$ , given by Eq. (2.12) with  $n = 0$ .

From Eq. (2.1), the general solution for the velocity potential is then,

$$\Phi = \frac{V_0}{2\pi k_r} \sum_{m=-\infty}^{\infty} \frac{1}{\Delta_m} \left\{ [Y'_m(k_r a) + Y'_m(k_r b)] J_m(k_r r) - [J'_m(k_r a) + J'_m(k_r b)] Y_m(k_r r) \right\} e^{i(m\theta - \omega t)}, \quad (2.41)$$

which involves the sum over all possible values of angular wave number. The corresponding pressure  $p = -\rho_0 \partial \Phi / \partial t$  is

$$\frac{p}{\rho_0 c V_0} = \frac{i}{2\pi} \sum_{m=-\infty}^{\infty} \frac{1}{\Delta_m} \left\{ [Y'_m(k_r a) + Y'_m(k_r b)] J_m(k_r r) - [J'_m(k_r a) + J'_m(k_r b)] Y_m(k_r r) \right\} e^{i(m\theta - \omega t)}. \quad (2.42)$$

Since

$$Y_{-m}(x) = (-1)^m Y_m(x), \quad (2.43)$$

and

$$J_{-m}(x) = (-1)^m J_m(x), \quad (2.44)$$

the pressure can be written as

$$\frac{p}{\rho_0 c V_0} = i \sum_{m=0}^{\infty} \frac{1}{\Delta_m} \left\{ [Y'_m(k_r a) + Y'_m(k_r b)] J_m(k_r r) - [J'_m(k_r a) + J'_m(k_r b)] Y_m(k_r r) \right\} \cos(m\theta) e^{-i\omega t}. \quad (2.45)$$

This pressure corresponds to a standing wave inside the toroid with a frequency dependent amplitude. As pointed out above, the behavior of  $\Delta_m$  is such that when the driving frequency corresponds to a characteristic frequency of the rigid wall toroid, this term is zero. This will result in an infinite pressure with the driving element located at a pressure antinode. Therefore, even though there is no restriction placed on the driving frequency, if the driving frequency is not one of the characteristic frequencies, the pressure amplitude will be negligible compared to the pressure corresponding to a characteristic frequency. As shown in Section 2.1, in the low frequency limit, these characteristic frequencies are those that fit a whole number of wavelengths along the circumference of the toroid.

### 2.2.2 Theoretical Results for a Lossless Fluid

For a toroid with dimensions given in Table 3.1, the pressure as a function of angular position in the toroid is shown in Fig. 2.3 for a frequency close to the first characteristic frequency, and in Fig. 2.4 for the second characteristic frequency. These calculations include the first thirty terms in the sum. It was necessary to use only these terms because contributions to the sum for higher terms are negligible for the frequencies of interest. The response of this tube at these frequencies is similar to that of a pipe of length  $l = \pi(a + b)/2$  with a piston driver at one end and the other end closed, as shown in the expansion for a narrow tube shown in Section 2.1.1. In the toroid, the first characteristic frequency corresponds to a wavelength equal to the circumference around the tube, so that at this frequency there are two antinodes, each located halfway between the driver and the opposite side. The phase of the pressure changes

by  $\pi$  at each antinode as expected for the case of a standing wave.

Figures 2.5 and 2.6 plot the pressure as a function of angular position in the toroid for frequencies that do not correspond to characteristic frequencies. One can see that the pressure amplitude is much less than that corresponding to a characteristic frequency.

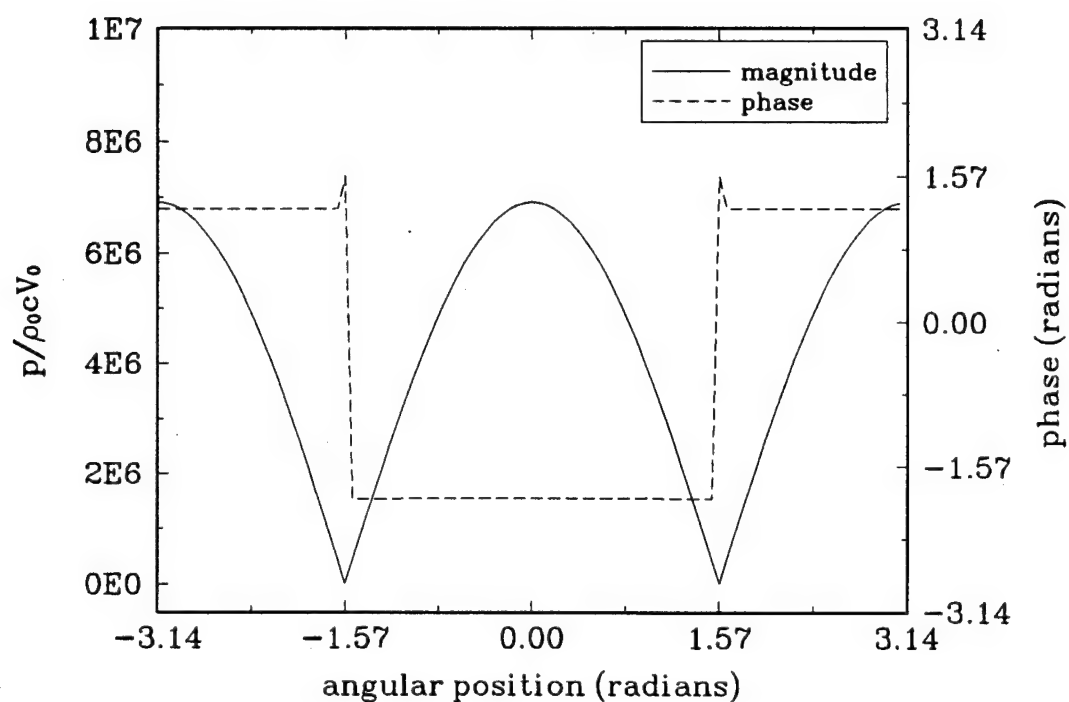


Figure 2.3: Theoretical complex pressure inside a toroid as a function of angular position driven with a single driving element. The driving element is located at  $\theta = 0$ . The driving frequency differs from the first characteristic frequency by 0.07%. Only the first thirty terms in the sum have been used.

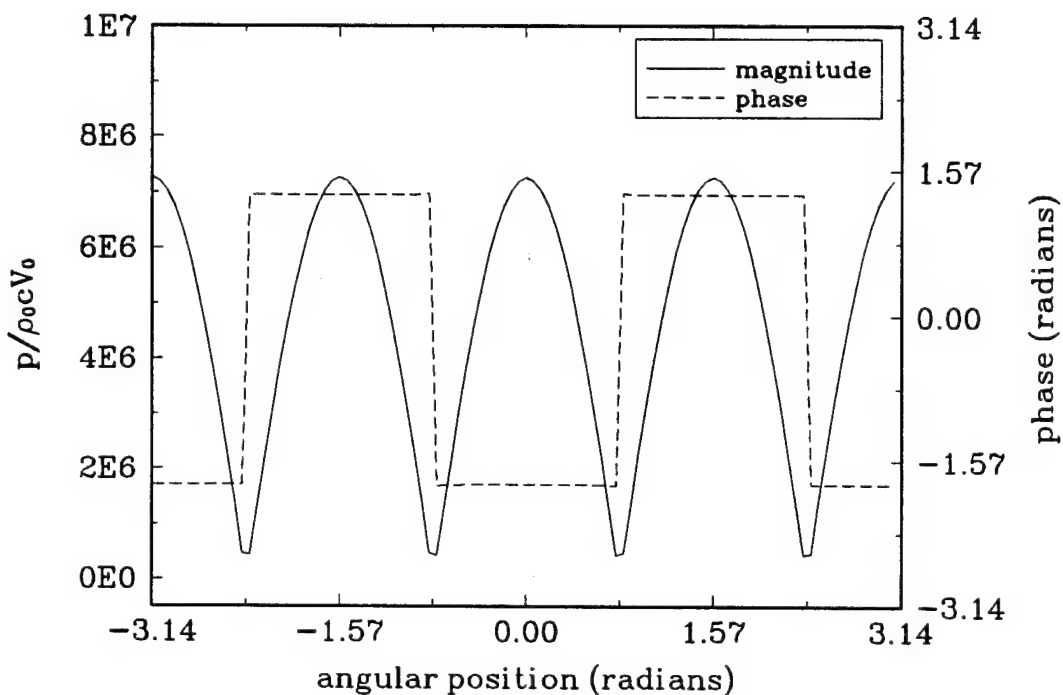


Figure 2.4: Theoretical complex pressure inside a toroid as a function of angular position driven with a single driving element. The driving element is located at  $\theta = 0$ . The driving frequency differs from the second characteristic frequency by 0.07%. Only the first thirty terms in the sum have been used.

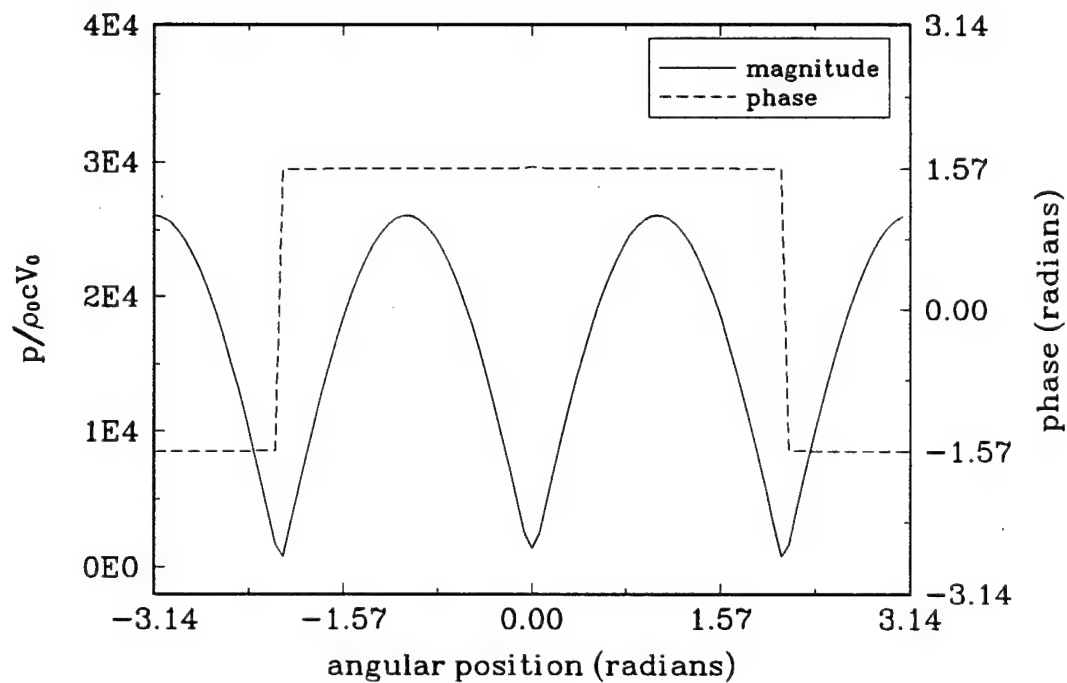


Figure 2.5: Theoretical complex pressure inside a toroid as a function of angular position driven with a single driving element. The driving element is located at  $\theta = 0$ . The driving frequency is halfway between the first and second characteristic frequency. Only the first thirty terms in the sum have been used.

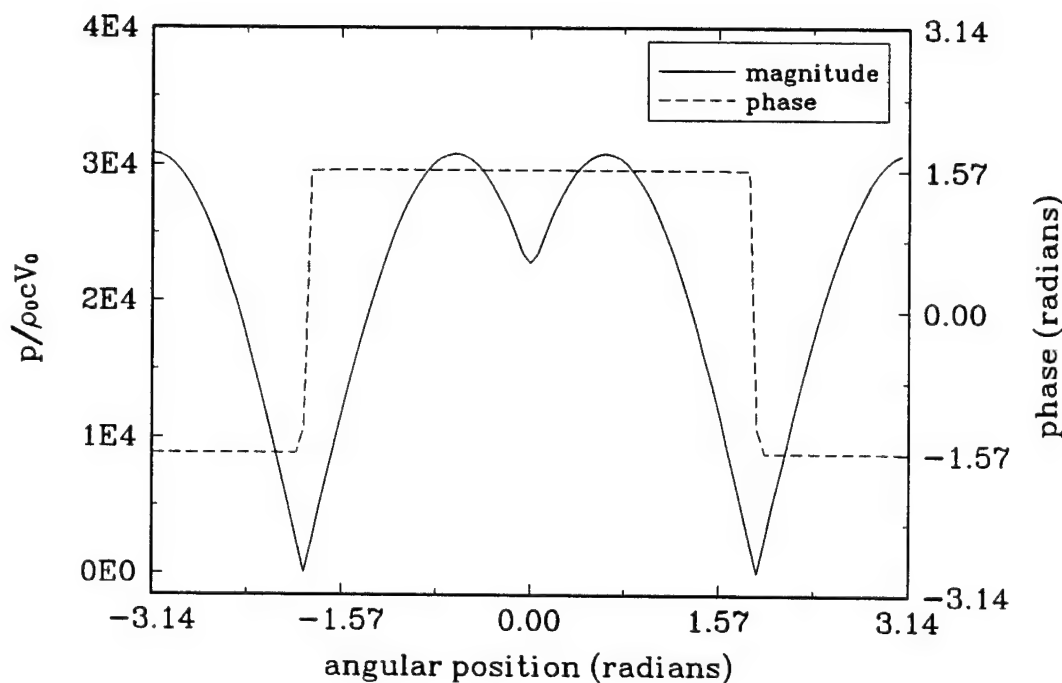


Figure 2.6: Theoretical complex pressure inside a toroid as a function of angular position driven with a single driving element. The driving element is located at  $\theta = 0$ . The driving frequency is a quarter of the way between the first and the second characteristic frequency. Only the first thirty terms in the sum have been used.

## 2.3 Application of Boundary Conditions: Driven Wall

### 2.3.1 Theory

Consider the case of a toroidal waveguide with a sinusoidal wave propagating along the wall between  $-\pi < \theta \leq \pi$  with an angular phase velocity  $\Omega$ . No restrictions will be placed on the choice of  $\Omega$  so that in general, a discontinuity in the driven wall will exist at  $\theta = \pi$ . Based on Eq. (2.2), the chosen  $\theta$  dependence will be

$$f(\theta) = e^{i\omega\theta/\Omega}. \quad (2.46)$$

(Note that  $\Omega = \Omega_m$  is not required, i.e., the value of  $\omega/\Omega$  is not necessarily an integer.)

When substituted into Eq. (2.29), the result is

$$\begin{aligned} A_l &= \frac{1}{2\pi} \int_{-\pi}^{\pi} e^{i\omega\theta'/\Omega} e^{-il\theta'} d\theta' \\ &= \frac{1}{2\pi} \int_{-\pi}^{\pi} e^{i(\omega/\Omega-l)\theta'} d\theta' \\ &= \frac{1}{2i(\omega/\Omega-l)\pi} [e^{i(\omega/\Omega-l)\pi} - e^{-i(\omega/\Omega-l)\pi}] \\ &= \frac{\sin(\omega/\Omega-l)\pi}{(\omega/\Omega-l)\pi}. \end{aligned} \quad (2.47)$$

For this driving condition, the amplitude of each angular mode will vary as a function of frequency and angular phase velocity.

Equations (2.26) and (2.27) then become,

$$\frac{\partial \Phi_m}{\partial r} \Big|_{r=a} = \sum_{l=-\infty}^{\infty} V_0 \frac{\sin(\omega/\Omega - l)\pi}{(\omega/\Omega - l)\pi} e^{il\theta} e^{-i\omega t}, \quad (2.48)$$

$$\frac{\partial \Phi_m}{\partial r} \Big|_{r=b} = \sum_{l=-\infty}^{\infty} -V_0 \frac{\sin(\omega/\Omega - l)\pi}{(\omega/\Omega - l)\pi} e^{il\theta} e^{-i\omega t}. \quad (2.49)$$

Using the general solution for the velocity potential given by Eq. (2.1) in the above and excluding the  $z$  dependence yields

$$\sum_{l=-\infty}^{\infty} V_0 \frac{\sin(\omega/\Omega - l)\pi}{(\omega/\Omega - l)\pi} e^{il\theta} = \sum_{m=-\infty}^{\infty} k_r [A_m J'_m(k_r a) + B_m Y'_m(k_r a)] e^{im\theta}, \quad (2.50)$$

$$\sum_{l=-\infty}^{\infty} -V_0 \frac{\sin(\omega/\Omega - l)\pi}{(\omega/\Omega - l)\pi} e^{il\theta} = \sum_{m=-\infty}^{\infty} k_r [A_m J'_m(k_r b) + B_m Y'_m(k_r b)] e^{im\theta}, \quad (2.51)$$

where  $k_r = \omega/c$ .

Following the same path used to reach Eqs. (2.36) and (2.37), these equations become

$$V_0 \frac{\sin(\omega/\Omega - m)\pi}{(\omega/\Omega - m)\pi} = A_m k_r J'_m(k_r a) + B_m k_r Y'_m(k_r a), \quad (2.52)$$

$$-V_0 \frac{\sin(\omega/\Omega - m)\pi}{(\omega/\Omega - m)\pi} = A_m k_r J'_m(k_r b) + B_m k_r Y'_m(k_r b). \quad (2.53)$$

Solving for  $A_m$  and  $B_m$  yields,

$$A_m = \frac{V_0}{k_r \Delta_m} [Y'_m(k_r a) + Y'_m(k_r b)] \frac{\sin(\omega/\Omega - m)\pi}{(\omega/\Omega - m)\pi}, \quad (2.54)$$

$$B_m = \frac{-V_0}{k_r \Delta_m} [J'_m(k_r a) + J'_m(k_r b)] \frac{\sin(\omega/\Omega - m)\pi}{(\omega/\Omega - m)\pi}, \quad (2.55)$$

where  $\Delta_m$  is defined by Eq. (2.40)

From Eq. (2.1), the general solution for the velocity potential for the driven wall toroid becomes

$$\begin{aligned}\Phi = & \frac{V_0}{k_r} \sum_{m=-\infty}^{\infty} \frac{1}{\Delta_m} \left\{ [Y'_m(k_r a) + Y'_m(k_r b)] J_m(k_r r) \right. \\ & \left. - [J'_m(k_r a) + J'_m(k_r b)] Y_m(k_r r) \right\} \frac{\sin(\omega/\Omega - m)\pi}{(\omega/\Omega - m)\pi} e^{i(m\theta - \omega t)}. \quad (2.56)\end{aligned}$$

The corresponding pressure is

$$\begin{aligned}p = & \frac{i\omega\rho_0 V_0}{k_r} \sum_{m=-\infty}^{\infty} \frac{1}{\Delta_m} \left\{ [Y'_m(k_r a) + Y'_m(k_r b)] J_m(k_r r) \right. \\ & \left. - [J'_m(k_r a) + J'_m(k_r b)] Y_m(k_r r) \right\} \frac{\sin(\omega/\Omega - m)\pi}{(\omega/\Omega - m)\pi} e^{i(m\theta - \omega t)}. \quad (2.57)\end{aligned}$$

Comparing this to the result in Eq. (2.12), it may be noted that the driving frequencies which produce infinite response are the resonant frequencies of the rigid wall toroid for the case of  $n = 0$ . Since  $\Delta_m$  is independent of the angular phase velocity, this resonance occurs at the characteristic frequencies regardless of the value of  $\Omega$ , even if an integral number of wavelengths does not fit in the toroid. This means that although the walls are moving (that is, they are not rigid) the behavior of the sound in the fluid will depend on the speed of sound in the infinite medium. Such a result in a tube with passive walls can only occur when the walls are rigid, which for the case of dense fluids (i.e., liquids), is often very difficult to obtain. Including losses in this solution will eliminate the unrealistic situation of an infinite amplitude. These losses will be dealt with in Section 2.4.

Consider the case of  $k_r a \neq \beta_{mp}$  such that the velocity potential remains finite. If the ratio of the angular frequency to the angular phase velocity is such that

$$\omega/\Omega = q \quad (2.58)$$

where  $q$  is an integer, then

$$\Phi \propto \sum_{m=-\infty}^{\infty} \frac{\sin(q-m)\pi}{(q-m)\pi} = \delta_{qm}. \quad (2.59)$$

This means only the angular wave number corresponding to  $m = q$  will contribute to the velocity potential;  $\Phi$  will represent a traveling wave. Such a wave will have an amplitude that is independent of angular position, and a phase difference between any two positions corresponds to the propagation time for the driven wave in the fluid.

If  $\omega/\Omega \approx m$ , the dominant term in the sum in Eq. (2.56) is the one corresponding to that value of  $m$ , with small contributions from other angular wave numbers. In this case, the sound in the duct is no longer a pure traveling wave, but it is also not a pure standing wave. However, if the choice of  $\omega/\Omega$  is such that the contribution of sound due to  $m < 0$  is the same as that for  $m > 0$ , then the result will be that of a standing wave inside the toroid.

### 2.3.2 Theoretical Results for a Lossless Fluid

Theoretical results for the pressure amplitude inside the driven wall toroid are shown in Figs. 2.7 and 2.8 for a toroid with dimensions given in Table 3.1. These calculations

include the range of  $m$  with values of -30 to 30. The values of angular phase velocity used are given in terms of the dimensionless quantity  $\Omega/\Omega_0$ , where  $\Omega_0$  is the angular phase velocity corresponding to the intrinsic speed of sound in the fluid. The  $\Delta_m$  dependence, which is independent of  $\Omega$  can be seen to drive the pressure amplitude to infinity at the characteristic frequencies of the rigid tube given by Eq. (2.12). (The fact that the peaks are not infinite in the graphs is a result of the finite frequency spacing missing the exact characteristic frequency values.) Varying  $\Omega/\Omega_0$  results in an asymmetry to the right for values of  $\Omega/\Omega_0 > 1$  (supersonic) and to the left for values of  $\Omega/\Omega_0 < 1$  (subsonic).

The condition for a traveling wave given by Eq. (2.58) is demonstrated in Fig. 2.9 where the sound pressure amplitude for four different values of angular position are plotted as a function of frequency for a specific value of  $\Omega$ . The circles on the plot indicate intersections where the amplitude is the same for all four positions. Traveling waves occur at these frequencies.

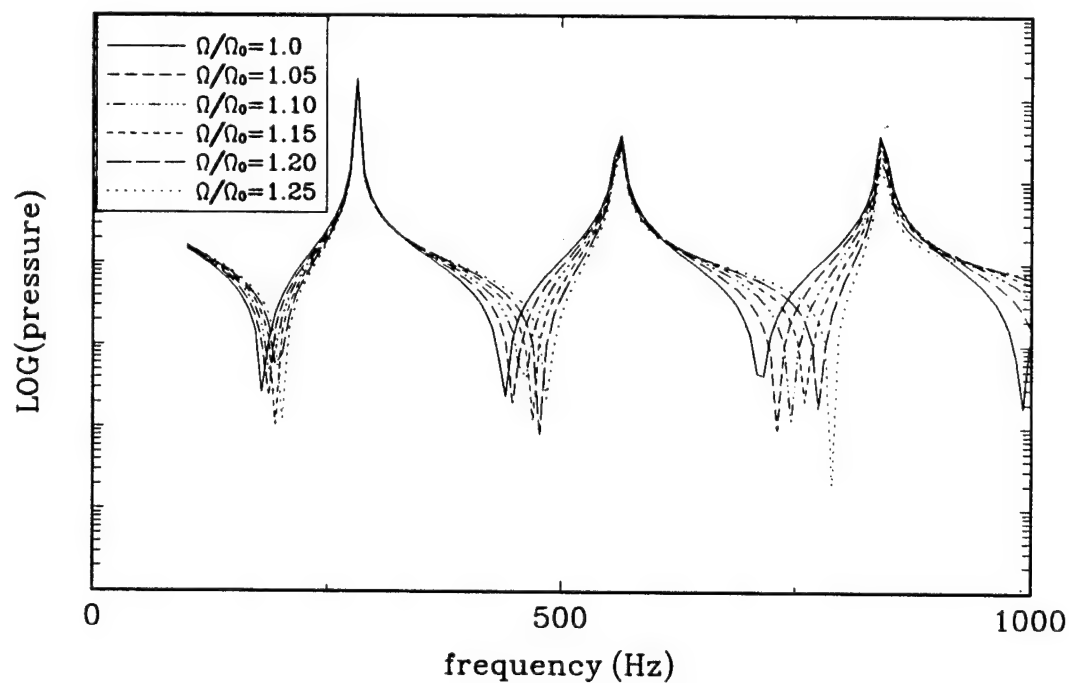


Figure 2.7: Sound pressure amplitude inside a toroid as a function of frequency for various values of  $\Omega \geq 1$  at  $\theta = 0$ . Values of  $m$  used range from -30 to 30.

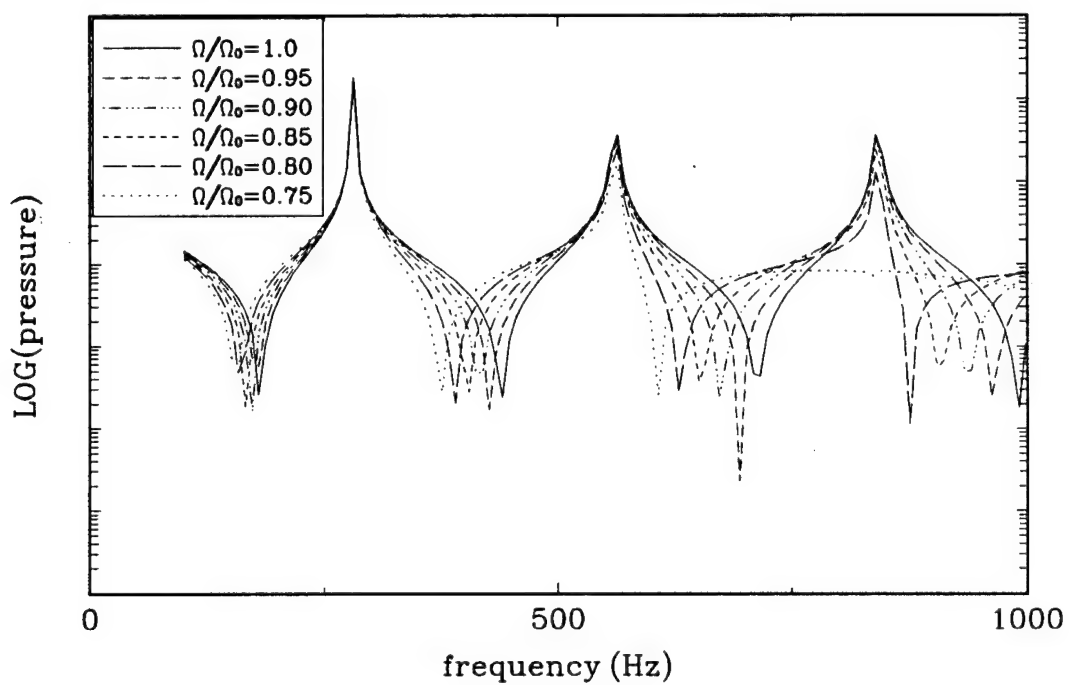


Figure 2.8: Sound pressure amplitude inside a toroid as a function of frequency for various values of  $\Omega \leq 1$  at  $\theta = 0$ . Values of  $m$  used range from -30 to 30.

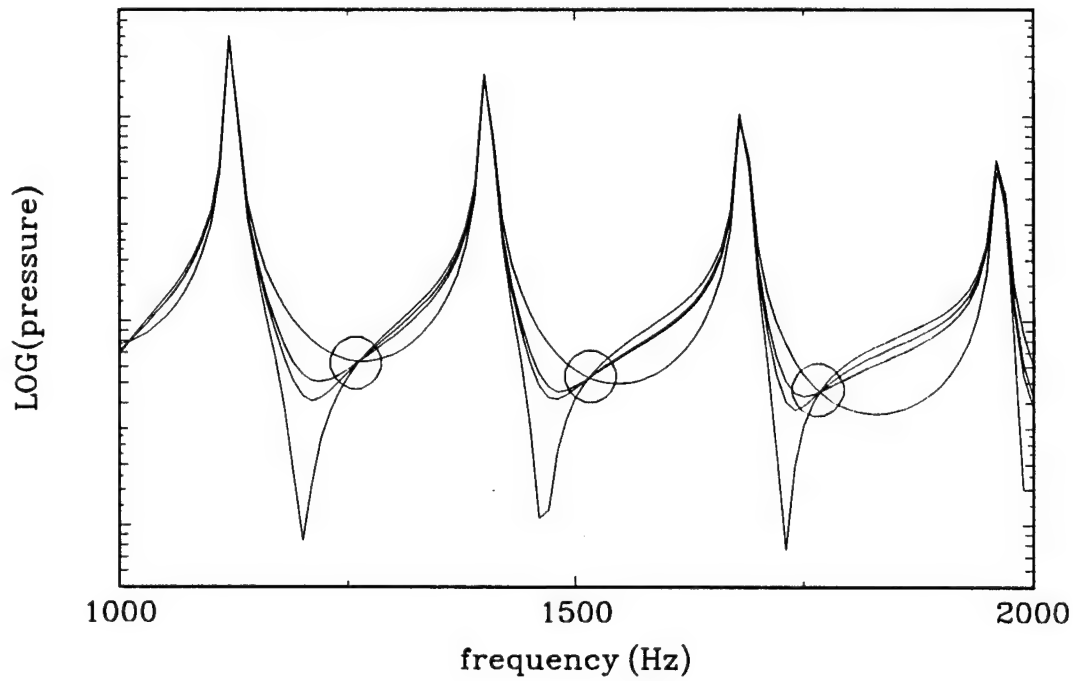


Figure 2.9: Theoretical values of the magnitude of the pressure at  $\theta = -3.30, -1.73, 0.16$ , and  $1.41$  radians. The frequencies at the circled intersections are those for the case of  $\Omega/\Omega_0 = 0.9$  that yield traveling waves.

## 2.4 General Theory for the Toroid Including Losses

In order to more realistically describe the propagation of sound in the toroid, it is necessary to include losses that will affect the sound amplitude. These losses can be treated by either obtaining the solution of the viscous fluid filled tube of Section 1.3 modified for the case of a toroid, or as modifications to the case of the inviscid fluid filled toroid of Section 2.1.

### 2.4.1 Solution for the Viscid and Thermally Conducting Fluid Filled Toroid

Consider the solution of the toroidal waveguide filled with a viscous and thermal conducting fluid. The approach followed is that used in Section 1.3 for the geometry of a straight cylindrical tube adapted for the case of a tube with sound propagating azimuthally in the toroidal waveguide derived in Section 2.1.

#### Solution of the Temperature Equation

The fourth-order differential equation describing the temperature dependence is [from Eq. (1.47)],

$$\frac{\omega^2}{c^2} T + \left[ 1 - i \left( \frac{\omega^2 l_e^2}{2c_T^2} + \frac{2\omega^2 l_v^2}{3c^2} \right) \right] \nabla^2 T - \left( 1 - \frac{2i\omega^2 l_v^2}{3c_T^2} \right) \frac{i l_e^2}{2} \nabla^4 T = 0. \quad (2.60)$$

Assume a solution to this equation of the form

$$T = \xi_1 Q_1(r) e^{im\theta} + \xi_2 Q_2(r) e^{im\theta}, \quad (2.61)$$

where

$$\nabla^2 [Q_{1,2}(r)e^{im\theta}] = \lambda_{1,2}Q_{1,2}(r)e^{im\theta} \quad (2.62)$$

where  $\lambda_1$  and  $\lambda_2$  are, from Eqs. (1.53) and (1.54)

$$\lambda_1 \approx -\frac{\omega^2}{c^2}, \quad (2.63)$$

and

$$\lambda_2 \approx -\frac{2i}{l_e^2}, \quad (2.64)$$

which are the acoustic and thermal roots, respectively.

Again consider a toroid with an inside radius of  $a$  and an outside radius  $b$  as shown in Fig. 2.1. The propagation of sound will be required to be in the azimuthal direction with no  $z$  dependence.

Equation (2.62) then simplifies to

$$\frac{\partial^2}{\partial r^2} [Q_{1,2}(r)e^{im\theta}] + \frac{1}{r} \frac{\partial}{\partial r} [Q_{1,2}(r)e^{im\theta}] + \frac{1}{r^2} \frac{\partial^2}{\partial \theta^2} [Q_{1,2}(r)e^{im\theta}] = \lambda_{1,2}Q_{1,2}(r)e^{im\theta}, \quad (2.65)$$

which becomes

$$\frac{dQ_{1,2}}{dr} + \frac{1}{r} \frac{dQ_{1,2}}{dr} + \left( -\lambda_{1,2} - \frac{m^2}{r^2} \right) Q_{1,2} = 0. \quad (2.66)$$

The general solution to this equation is a linear combination of Bessel and Neumann functions (see Section 1.2),

$$Q_{1,2} = A_{1,2}J_m \left( r\sqrt{-\lambda_{1,2}} \right) + C_{1,2}Y_m \left( r\sqrt{-\lambda_{1,2}} \right). \quad (2.67)$$

This equation, along with Eq. (2.61), is the solution for the temperature  $T$ .

### Solution of the Velocity Equation

To find the solution for the velocity components, the approach found in Section 1.3.3 will be used. Equations (1.58)–(1.60) apply to this procedure; assume a solution for the particular velocity,

$$\mathbf{u}'' = \nabla [\zeta_1 Q_1(r) e^{im\theta} + \zeta_2 Q_2(r) e^{im\theta}] . \quad (2.68)$$

Substituting this and Eq. (2.61) into Eq. (1.60), yields

$$\begin{aligned} 0 &= \nabla \cdot \{ \nabla [\zeta_1 Q_1(r) e^{im\theta} + \zeta_2 Q_2(r) e^{im\theta}] \} + i\omega [\xi_1 Q_1(r) + \xi_2 Q_2(r)] e^{im\theta} \\ &\quad + \frac{\gamma l_e^2 \omega}{2} \{ \xi_1 \nabla^2 [Q_1(r) e^{im\theta}] + \xi_2 \nabla^2 [Q_2(r) e^{im\theta}] \} . \end{aligned} \quad (2.69)$$

For this equation to always be true,

$$\begin{aligned} 0 &= \zeta_{1,2} \nabla^2 [Q_{1,2}(r) e^{im\theta}] + i\omega \xi_{1,2} Q_{1,2}(r) e^{im\theta} \\ &\quad + \frac{\gamma l_e^2 \omega}{2} \xi_{1,2} \nabla^2 [Q_{1,2}(r) e^{im\theta}] . \end{aligned} \quad (2.70)$$

Solving for  $\zeta_{1,2}$  using Eq. (2.62) gives

$$\zeta_{1,2} = -\xi_{1,2} \omega \left( \frac{\gamma l_e^2}{2}, +\frac{i}{\lambda_{1,2}} \right) \quad (2.71)$$

which along with Eq. (2.68) is the general solution for the particular equation of the velocity.

To find the solution for  $u'$ , once again consider Eq. (1.65), which is

$$i\omega u' + \frac{l_v^2 \omega}{2} \nabla^2 u' = 0. \quad (2.72)$$

As in the similar derivation in Section 1.3.3, one must solve for the homogeneous components of velocity separately. First consider the radial component of the velocity,

$$\begin{aligned} 0 &= iv' + \frac{l_v^2}{2} \left( \frac{\partial^2 v'}{\partial r^2} + \frac{1}{r} \frac{\partial v'}{\partial r} + \frac{1}{r^2} \frac{\partial^2 v'}{\partial \theta^2} \right) \\ &= iv' + \frac{l_v^2}{2} \left( \frac{\partial^2 v'}{\partial r^2} + \frac{1}{r} \frac{\partial v'}{\partial r} - \frac{m^2}{r^2} v' \right) \\ &= \frac{\partial^2 v'}{\partial r^2} + \frac{1}{r} \frac{\partial v'}{\partial r} + \left( \frac{2i}{l_v^2} - \frac{m^2}{r^2} \right) v', \end{aligned} \quad (2.73)$$

whose solution is

$$v' = \xi_0 Q_0 e^{im\theta}, \quad (2.74)$$

where

$$Q_0 = A_0 J_m(r\sqrt{2i/l_v^2}) + C_0 Y_m(r\sqrt{2i/l_v^2}). \quad (2.75)$$

From Eq. (1.59) the relationship between  $v'$  and  $w'$  is

$$\begin{aligned} 0 &= \frac{1}{r} \frac{\partial r v'}{\partial r} + \frac{1}{r} \frac{\partial w'}{\partial \theta} \\ &= \frac{v'}{r} + \frac{\partial v'}{\partial r} - \frac{im}{r} w'. \end{aligned} \quad (2.76)$$

Solving for  $w'$  in terms of  $v'$  yields,

$$w' = \frac{-i}{m} \left( v' + r \frac{\partial v'}{\partial r} \right). \quad (2.77)$$

Combining the equations for the homogeneous and particular parts of the radial and azimuthal velocity yields, for the radial velocity,

$$\begin{aligned}
 v &= v' + v'' \\
 &= \xi_0 Q_0 e^{im\theta} - \sum_{j=1}^2 \frac{\partial}{\partial r} \left[ \xi_j \omega \left( \frac{\gamma l_e^2}{2} + \frac{i}{\lambda_j} \right) Q_j e^{im\theta} \right] \\
 &= \left[ \xi_0 Q_0 - \sum_{j=1}^2 \xi_j \omega \left( \frac{\gamma l_e^2}{2} + \frac{i}{\lambda_j} \right) \frac{dQ_j}{dr} \right] e^{im\theta}, \tag{2.78}
 \end{aligned}$$

and for the azimuthal velocity,

$$\begin{aligned}
 w &= w' + w'' \\
 &= \frac{-i}{m} \left[ \xi_0 Q_0 e^{im\theta} + r \frac{\partial}{\partial r} (\xi_0 Q_0 e^{im\theta}) \right] + \sum_{j=1}^2 \frac{1}{r} \frac{\partial}{\partial \theta} \left[ \xi_j \omega \left( \frac{\gamma l_e^2}{2} + \frac{i}{\lambda_j} \right) Q_j e^{im\theta} \right] \\
 &= \left[ \frac{-i \xi_0}{m} \left( Q_0 + r \frac{\partial Q_0}{\partial r} \right) + \sum_{j=1}^2 \frac{im}{r} \xi_j \omega \left( \frac{\gamma l_e^2}{2} + \frac{i}{\lambda_j} \right) Q_j \right] e^{im\theta}, \tag{2.79}
 \end{aligned}$$

where  $Q_0$ ,  $Q_1$ , and  $Q_2$  are defined by Eqs. (2.67) and (2.75).

### Application of the Driven Wall Boundary Condition

The solutions for the coefficients in the equations above (there are a total of six to solve for) can be derived by the application of the appropriate boundary conditions. If one considers the case of the driven wall from Section 2.1.2 for the radial component and assumes similar boundary conditions for the axial velocity and the temperature for the case of the straight tube in Section 1.3.4, then

$$w|_{r=a} = w|_{r=b} = 0, \tag{2.80}$$

$$\mathcal{T}|_{r=a} = \mathcal{T}|_{r=b} = 0, \quad (2.81)$$

$$v|_{r=a} = V_0 f(\theta) e^{-i\omega t}, \quad (2.82)$$

$$v|_{r=b} = -V_0 f(\theta) e^{-i\omega t}. \quad (2.83)$$

Solving for the coefficients in Eqs. (2.61), (2.78), and (2.79) using the boundary conditions given above, the solution for sound propagation in a viscous and thermally conducting fluid filled toroidal waveguide with driven walls can be derived.

#### 2.4.2 Attenuation

The solution above requires the solution of a  $6 \times 6$  matrix equation which, for the present purpose, is not practical to solve. Therefore, it is advantageous to consider an alternative approach to the problem. It is also important to note that the configuration used for making experimental measurements consists of a compliant wall tube with individual driving elements (see Chapter 3). This is one source of attenuation not considered by the theory of the previous section.

Another approach that will be presented is that of including losses in the toroid by considering the wave number in the fluid to be complex. Once the value of this wave number is determined, Eq. (2.57) can be used to solve for the pressure in the toroid.

The complex wave number can be written as

$$\bar{k} = k - i\alpha, \quad (2.84)$$

where  $\alpha$  is the *absorption coefficient* and  $k = \omega/c$ . The sources of attenuation are

the various mechanisms that take energy out of the system. These effects combine so that the total absorption coefficient can be considered as the sum of the absorption coefficients of each individual loss mechanism calculated independently so that

$$\alpha = \sum_i \alpha_i. \quad (2.85)$$

In practice, this will be true as long as  $\alpha/k \ll 1$  [42].

### The Tube Effect

Because of imposed boundary conditions due to the walls of the tube, the effects of viscosity and thermal conductivity on propagating sound are significant (see Section 1.3). For wide rigid tubes, that is a tube where the skin depth occupies only a small fraction of the cross-sectional area, the attenuation is given by [38]

$$\alpha_w = 2^{-3/2} \left( \frac{\omega \mu}{\rho_0 c^2} \right) \left[ 1 + \sqrt{\frac{\kappa}{\mu C_p}} (\gamma - 1) \right] \frac{S}{A} \quad (2.86)$$

where  $S$  is the length of the perimeter and  $A$  is the cross-sectional area. The quantity  $\mu C_p / \kappa$  is called the Prandtl number. For air at 27°C, and a pressure of 1 atmosphere, the coefficient of absorption is

$$\alpha_w = 2.87 \times 10^{-5} \frac{\sqrt{f}}{a}. \quad (2.87)$$

## Classical Absorption and Absorption by Relaxation Processes

The attenuation of sound in the bulk medium due to viscous and thermal effects, as well as molecular relaxation, is insignificant compared to  $\alpha_w$  at the frequencies of interest. For this reason these will be ignored.

### Compliant Walls

For the case of sound propagating in a tube with compliant or elastic walls, there is an additional contribution to the overall attenuation due to the motion of the wall. The expression for such attenuation in terms of the impedance of the wall is given by [15]

$$\alpha_{cw} = \text{Re}\left(\frac{\rho_0 c}{Z}\right) \frac{S}{2A}. \quad (2.88)$$

The quantity  $Z$  will be related to the elastic properties of the wall as a function of frequency.

Consider a length of cylindrical tube  $L$  with radius  $a$  and thickness  $T$  shown in Fig. (2.10). The sum of the forces exerted on the tube wall are equal to the time rate of change of the momentum of the wall, i.e.

$$p + p_e = \rho_w \frac{dv}{dt} \quad (2.89)$$

where  $p$  is the sound pressure pushing the wall radially outward, and  $p_e$  is an effective pressure caused by the elastic force pulling the wall inward, to be obtained below.

Consider a rectangular piece of elastic material of length  $x$  and cross-sectional area  $A$  which is stretched by an amount  $\Delta x$  under the influence of a tensile force  $F_e$ .

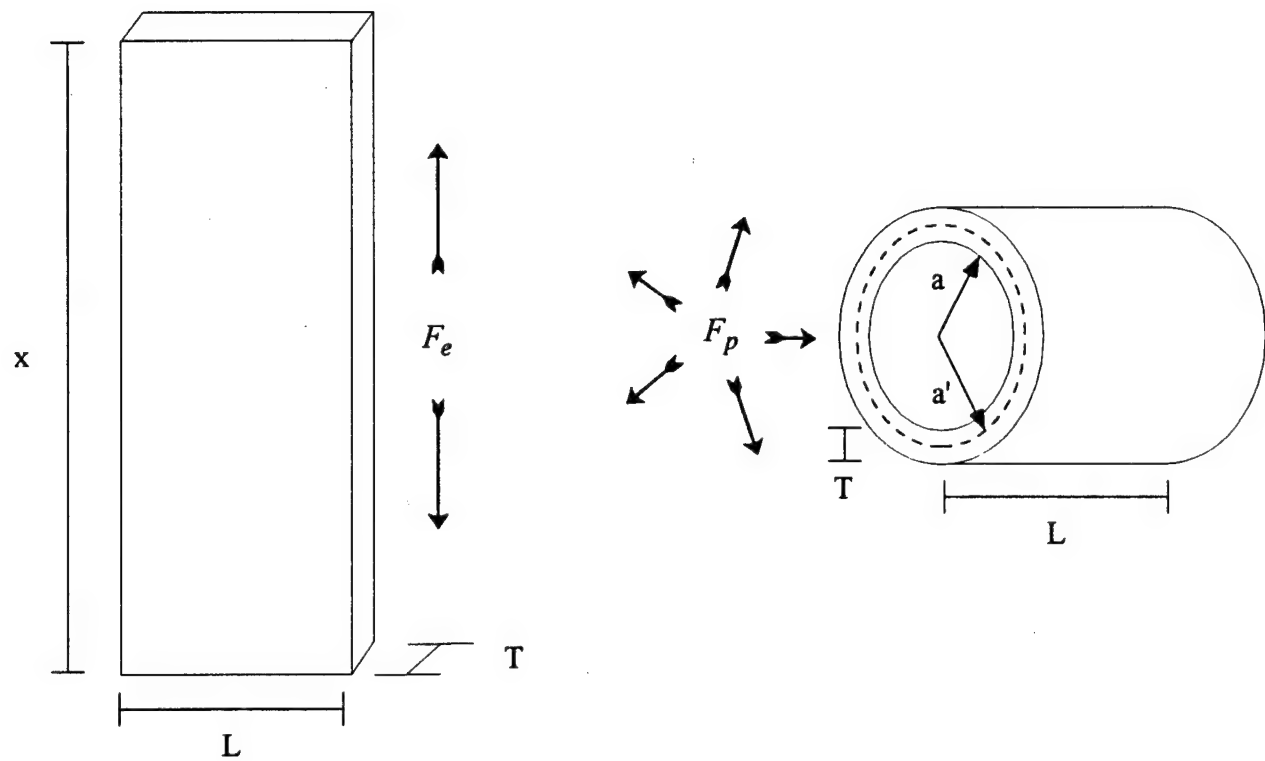


Figure 2.10: Elastic tube considered in derivation of absorption coefficient. The figure on the left is the open section of tube shown on the right. Vectors are shown indicating the direction of the elastic force ( $F_e$ ) and the force due to the pressure ( $F_p$ ) are shown.

Then from Hooke's law,

$$F_e = -k\Delta x. \quad (2.90)$$

The force constant  $k$  can be expressed in terms of Young's modulus, which is the ratio of the stress to the strain,

$$Y = \frac{F_e}{A} \frac{x}{\Delta x}. \quad (2.91)$$

The potential energy stored in the elastic material when it is stretched is given by

$$U = \frac{1}{2}k\Delta x^2. \quad (2.92)$$

Now bend the material into a circle so that it forms a section of tube. The unstretched length is now the circumference of the tube, given by

$$x = 2\pi a', \quad (2.93)$$

and the elongation of the material is now an increase in circumference, given by

$$\Delta x = 2\pi\Delta r. \quad (2.94)$$

If this elongation is due an effective surface pressure  $p_e$ , then this force is

$$\begin{aligned} p_e &= -\frac{\partial U}{\partial(\Delta r)} \frac{1}{2\pi a L} \\ &= -\frac{\partial}{\partial(\Delta r)} \left( \frac{1}{2} \frac{TLY}{2\pi a'} 4\pi^2 \Delta r^2 \right) \frac{1}{2\pi a L} \\ &= -\frac{TY}{aa'} \Delta r. \end{aligned} \quad (2.95)$$

Substituting this into Eq. (2.89) yields

$$p - \frac{YT\Delta r}{aa'} = \rho_w T(-i\omega v) \quad (2.96)$$

where an  $\exp(-i\omega t)$  dependence on the velocity has been assumed. Such a time dependence also yields  $\Delta r = iv/\omega$ . Solving for  $Z$  yields,

$$Z \equiv \frac{p}{v} = i \left( \frac{YT}{aa'\omega} - \omega \rho_w T \right). \quad (2.97)$$

Inspection of Eq. (2.88) shows that in order to determine the attenuation due to the compliant walls, it is necessary to have an expression for the real part of  $Z$ . The quantity  $Y$  can be considered to be complex, so that

$$Z \equiv \frac{p}{v} = \text{Re}(Z) + i \left( \frac{\text{Re}(Y)T}{aa'\omega} - \omega \rho_w T \right). \quad (2.98)$$

This can be determined using the imaginary part just derived along with information from experimental data. If  $Z = \text{Re}(Z) + i \text{Im}(Z)$ , then Eq. (2.88) becomes

$$\alpha_{\text{CW}} = \frac{\rho_0 c \text{Re}(Z)}{\text{Re}(Z)^2 + \text{Im}(Z)^2} \frac{1}{a} - i \frac{\rho_0 c \text{Im}(Z)}{\text{Re}(Z)^2 + \text{Im}(Z)^2} \frac{1}{a}. \quad (2.99)$$

The imaginary term will dominate  $Z$  for all frequencies, except for the resonant frequency. For this case, the impedance can be considered to be mostly real such that  $\text{Im}(Z) \approx 0$ . At this frequency, setting the imaginary term to zero,

$$\alpha_{\text{CW}}^R = \frac{1}{a} \frac{\rho_0 c}{\text{Re}(Z)} \quad (2.100)$$

where  $\alpha_{\text{CW}}^R$  is the value of the attenuation measured at the resonant frequency. Using this,  $Z$  can now be written as

$$Z = \frac{\rho_0 c}{a \alpha_{\text{CW}}^R} + i \left( \frac{\text{Re}(Y) T}{aa' \omega} - \omega \rho_w T \right). \quad (2.101)$$

Substituting this into Eq. (2.102) yields

$$\alpha_{\text{CW}} = \alpha_{\text{CW}}^R \left[ 1 + \left( \frac{\rho_w}{\rho_0} \right)^2 \left( \frac{\omega \alpha_{\text{CW}}^R}{c} \right)^2 \left( \frac{a \omega_0^2}{a' \omega^2} - 1 \right)^2 \right]^{-1}, \quad (2.102)$$

where

$$\omega_0 = \sqrt{\text{Re}(Y) / aa' \rho_w}, \quad (2.103)$$

which is determined by setting  $Z = 0$  in Eq. (2.98).

## 2.5 Chapter Summary

In this chapter, the solutions for sound propagating in lossless fluid filled toroidal waveguides has been presented for both rigid and driven wall cases. For the case of driven walls, two types of boundary conditions have been considered: (1) all rigid walls except for a single driving element, and (2) a sinusoidal wave propagating along  $\theta$ , where  $\pi < \theta \leq \pi$ , with a given wave number and angular phase velocity. For both cases, the inner and outer walls contained the driving elements and the top and bottom walls were held rigid. Two methods for including losses in the system have also been presented.

For the case of the rigid wall toroidal waveguide, solutions exist only for certain

frequencies. In the narrow tube limit, these frequencies correspond to those producing an integral number of wavelengths along the circumference, that is the curvature of the waveguide has no effect on the nature of the solution.

For the case of the driven wall toroid, the resulting sound pressure in the toroid driven at a single point is a standing wave of infinite amplitude at the characteristic frequencies of the rigid wall tube. On the other hand, driving the entire wall at a single phase velocity results in (1) infinite peaks in the pressure when the frequency corresponds to a characteristic frequency of the rigid wall toroid (the circumference corresponds to a whole number of wavelengths for the bulk speed of sound in the fluid), and (2) traveling waves when the ratio of the phase velocity and the driving frequency is an integer value (the circumference corresponds to a whole number of wavelengths in the wall).

Two methods have been considered to include losses in the system. The first gives six boundary value equations from which the velocity components can be solved. These equations give the particle velocity and temperature in a conducting, viscous medium that are similar to those derived in Section 1.3, except with the geometry of a toroid. The second method derives the frequency dependence of the absorption due to a yielding wall based on an empirical measurement, and adds it to the tube absorption calculated from the traditional equation for a wide tube.

# Chapter 3

## Experimental Results

Experimental verification of theory derived in Chapter 2 is presented in this chapter.

The following experiments were performed:

- velocity amplitude and displacement of the driven wall of a toroid,
- attenuation in a toroid with compliant walls (from Section 2.4.2),
- toroid with a delta function driver (from Section 2.2),
- toroid with driven walls (from Section 2.3),
- traveling waves in a driven wall toroid (from Section 2.3).

First, the construction of a driven wall torus as well as the operation of the digital circuit used to drive it will be discussed.

## 3.1 Experimental Devices

### 3.1.1 The Torus with Driven Walls (The Acoustitron)

Table 3.1: Dimensions and configuration of the acoustitron.

torus	$R_0$ (cm)	19.40
	a (cm)	1.27
driving elements	number	32
	width (cm)	1.27
	thickness (cm)	0.32
	O.D. (cm)	3.81

In order to verify the theoretical results for sound propagation in a toroidal waveguide with driven walls, a device was built that has been called an *acoustitron*. It consists of a length of Tygon®<sup>1</sup> with the ends connected to form a torus. Mounted around the outside are thirty-two evenly spaced piezoceramic rings as shown in Fig. 3.1. The dimensions of the acoustitron are given in Table 3.1. The driving elements have electrodes on the inner and outer surfaces and are poled in the radial direction. In the presence of a varying electric field, the change in thickness is primarily in the radial direction. The piezoelectric properties of the driving elements used are given in Table 3.2. Each element is glued to the torus in order to maximize the coupling between the driver and the tube wall.

A second torus made of soft PVC was also constructed, but with only a single movable driving element. This tube was used in measurements described in Sections 3.3.2 and 3.3.5 and will be referred to as the *PVC torus*. The dimensions of this tube

---

<sup>1</sup> "TYGON" is a registered trademark of Norton Company.

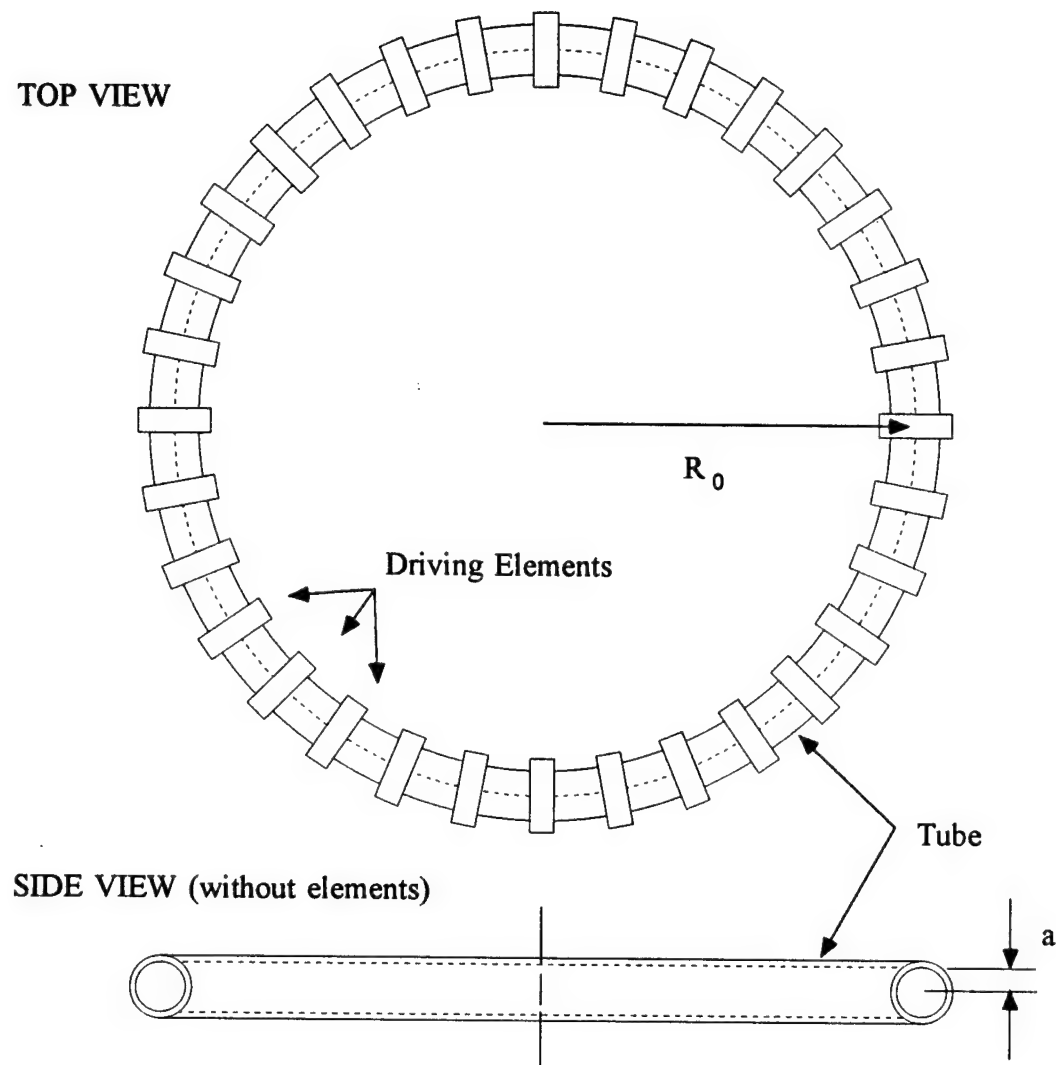


Figure 3.1: The acoustitron.

Table 3.2: Piezoelectric properties of EDO Corporation EC-70 piezoelectric driving element, equivalent to DOD-STD-1376A(SH) Type V (Lead Zirconate Titanate). Note that the values given are nominal; actual production values vary  $\pm 10\%$ . (Source: EDO Corporation, Acoustics Division, Salt Lake City, Utah.)

Piezoelectric Properties	Values
density ( $\text{Kg m}^{-3}$ )	$7.45 \times 10^3$
Young's modulus ( $\text{N m}^{-2}$ )	$6.3 \times 10^{10}$
dielectric constant at 1 kHz	2750
$d_{31}$ ( $\text{m V}^{-1}$ )	$-230 \times 10^{-12}$
$d_{33}$ ( $\text{m V}^{-1}$ )	$490 \times 10^{-12}$
frequency constant (kHz m)	1.727

are the same as those of the acoustitron.

Sound pressure measurements were made using a Brüel & Kjær eighth-inch microphone (type 4138) inserted through an airtight opening in the wall of the tube. The protective grille was carefully removed and the microphone was positioned flush with the tube wall so that it was perpendicular to the  $z$  axis in the  $z$  plane bisecting the torus. A Hewlett Packard 35665A Signal Analyzer was configured to record the sound pressure level (SPL) measured with the microphone.

### 3.1.2 The Acoustitron Driving Circuit

In order to drive the acoustitron, it was necessary to design and build a digital delay circuit capable of driving thirty-two elements with a specific time delay between outputs. The circuit built consisted of a single input and thirty-two analog outputs. A diagram outlining the basic components of the circuit is shown in Fig. 3.2.

The input signal could be produced by either an external analog source, or by

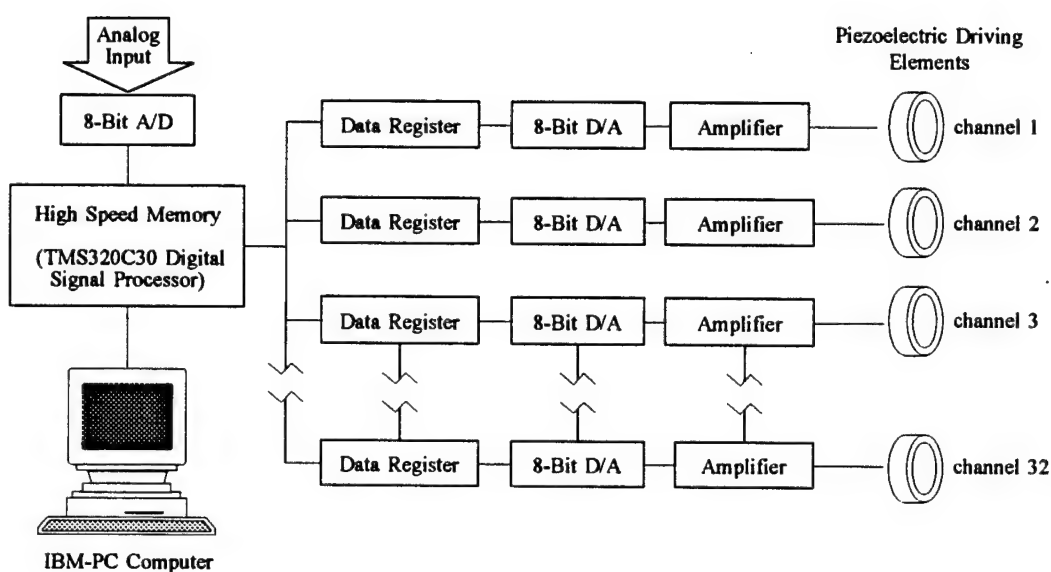


Figure 3.2: Diagram of the digital delay circuit used to drive the acoustitron. The user can control the time delay between successive outputs, as well as which output is the first in the output sequence. In general, there will be a discontinuity between the first and last outputs of the circuit which will fix the position of the microphone to a specific position in the acoustitron. By allowing the user to vary the location of the “break” in the driving wall, the microphone can be “moved” around the tube to any of thirty-two “positions”.

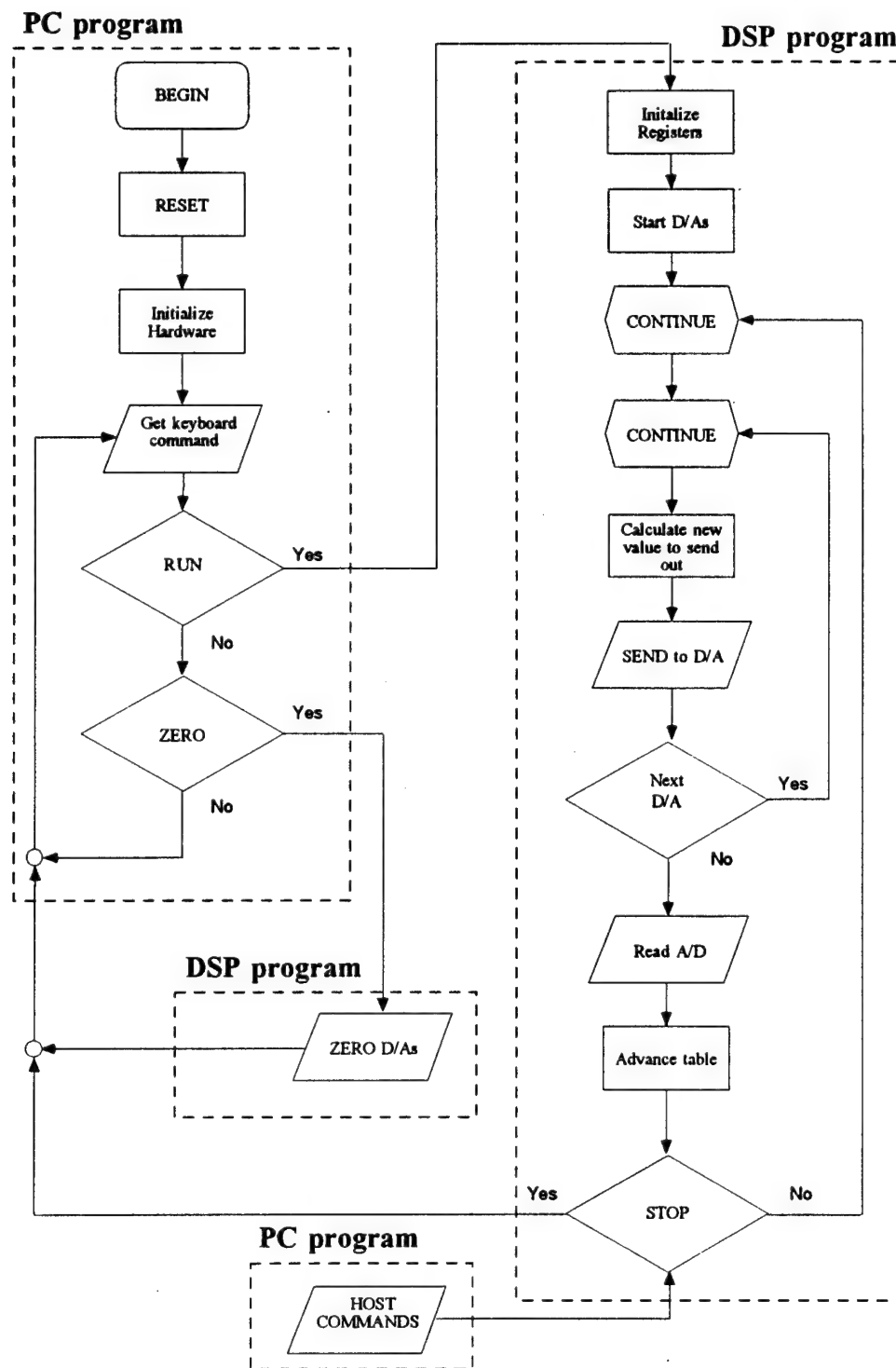
an internal preprogrammed waveform stored in memory. For the case of external input, the analog signal was received through an eight-bit analog-to-digital converter and loaded into the high speed memory of a Texas Instruments TMS320C30 Digital Signal Processor (DSP) which was located inside an IBM-PC compatible computer.

The method of operation of the circuit is as follows: as data (the instantaneous driving level) is loaded into memory, the most recent data is placed at the top of the memory stack and the data at the bottom of the stack is discarded so that with each successive input, the digital data is pushed through the stack. During each sample, data from thirty-two different equally spaced positions in the stack are pulled out and loaded into thirty-two data registers. For a fixed sample time, the "distance" between these positions corresponds to a specific time delay from one channel to the next. The values in the registers are then sent in parallel to individual amplifiers, which in turn drive the piezoceramic elements. The result is thirty-two "function generators" with identical waveforms, but shifted in time. (See Appendix B for a detailed schematic of the digital delay circuit.)

Note that this method is limited to time delays that are an integral number of the sample time. For example, if the sample rate of the circuit is 33.3 kHz, then the allowed time delays will be  $30n$  microseconds, where  $n$  is an integer. In order to avoid this limitation, non-integer values of  $n$  are used by interpolating between known integer values of  $n$ . For example, if a time delay of 45 microseconds is desired, and the value in memory for  $n = 1$  is 1.5 and for  $n = 2$  is 2.5, then the value sent to the output register will be 2.0. This way, there is no restriction on the time delay values that can be used. For a sinusoidal driving signal, if the signal period is long compared to the desired delay time, the interpolated value will be a good approximation.

Software consisted of a PC-side program that allowed the parameters to be set in the DSP, and a DSP-side program which controlled the operation of the DSP. A flowchart of these programs is shown in Fig. 3.3

Figure 3.3: Flowchart of computer programs used to operate the DSP.



## 3.2 Comparing Geometries of Theory and Experiment

To this point, only the two-dimensional solution for a toroid with driven walls has been considered, i.e., a toroid with a rectangular cross-section and no  $z$  dependence. Experimentally, it is easier to construct a toroid with a circular cross-section with driving rings, than to build one with a rectangular cross-section. In order to compare theory and experiment, some statements need to be made about these two geometries.

### 3.2.1 Tube Geometry

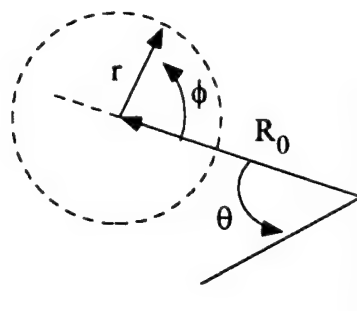


Figure 3.4: The toroidal coordinate system.

It is desirable to derive the solution for sound propagation in a toroid with a circular cross-section, i.e., the toroidal coordinate system (Fig. 3.4). The problem encountered is that the wave equation written in such a system, which is given by Cummings [36]

as

$$\frac{\partial^2 p}{\partial r^2} + \left( \frac{1}{r} - \frac{\cos \phi}{l} \right) \frac{\partial p}{\partial r} + \frac{1}{r^2} \frac{\partial^2 p}{\partial \phi^2} + \frac{\sin \phi}{rl} \frac{\partial p}{\partial \phi} + \frac{1}{l^2} \frac{\partial^2 p}{\partial \theta^2} - \frac{1}{c^2} \frac{\partial^2 p}{\partial t^2} = 0, \quad (3.1)$$

is not a separable equation, where  $l = R - r \cos \phi$ . In order to compare the theoretical case of a rectangular cross-section to the experimental results obtained from a circular cross-section, it is therefore necessary to make approximations. It has been shown in Section 2.1.1 that for wavelengths long compared to the width of the toroid, the shape of the bend can be ignored. Therefore, the toroid can be thought of as an infinitely long tube with a driven wall that is periodic along the center axis. In a viscous and conducting fluid filled tube with a given cross-sectional shape, the propagation characteristics of sound can be expressed in terms of an average over the cross-sectional area, defined by [43,44]

$$F(\lambda) \equiv \langle \phi \rangle = \frac{1}{A} \oint \phi(s) dA. \quad (3.2)$$

Given such a function, the density is given by

$$\rho(\omega) = \rho_0 / F(\lambda). \quad (3.3)$$

The *characteristic pore radius* is given as twice the transverse pore area divided by the pore perimeter. For a rectangular cross-section of height  $a$  and width  $b$ , the characteristic pore radius is  $ab/(a+b)$ . For a circular cross-section of radius  $r$ , the characteristic pore radius is  $r$ . If  $a = b = 2r$  for the rectangular cross-section, then both geometries will have the same value for the characteristic pore radius. Therefore, the propagation characteristics of sound in narrow toroids, will be the same for these

two geometries if the widths and heights are identical.

In his paper on sound propagation in curved tubes, Cummings [36] compared the experimental sound pressure measured across a circular duct to the theoretical case of a rectangular duct. (The range of wave numbers considered were those comparable to the radius of curvature of the tube.) He found that the pressure distribution from inside to outside radius for both cases were almost identical when the width of the square duct was set equal to the diameter of the circular duct. For the pressure distribution from top to bottom, he found some variation in the results. From this, as well as impedance measurements, he proposed that an alternative to the duct of circular cross-section is a rectangular duct with a width equal to the diameter of the circular cross-section, and a height such that the cross-sectional areas of the two shapes were identical.

In both of these cases, square and circular ducts are considered equivalent when the widths are the same. Therefore a comparison of the theory for sound propagation in a rectangular duct to experiments performed in circular ducts can be made if the widths of the ducts are equal.

### **3.2.2 Driving Geometry**

The analysis of the toroid in Chapter 2 is restricted to two-dimensions, as opposed to three-dimensions, in order to simplify the problem. Driving both top and bottom walls, as well as the inside and outside walls, adds to the complexity of the problem without gaining any new information.

Another advantage of the two-dimensional approach is the similarity to the torus

used in experiments. For the case of the driven toroid discussed in Section 2.1.2, there is only one independent coordinate across the cross-section because of symmetry in the  $z$  direction. For the experimental case, driving rings are used to produce motion in the wall. This motion is symmetric in terms of  $\phi$  (Fig. 3.4), so that across the cross-section there will be only one independent coordinate.

Analysis of measurements shown in Sections 3.3.3 and 3.3.4 justify this approximation.

### 3.3 Experiments

#### 3.3.1 Velocity and Displacement of the Tube Walls

In order to calculate the theoretical pressure amplitude of sound propagating in the acoustitron [Eq. (2.57)], it was necessary to know the velocity amplitude of the driven wall. For this reason, velocity amplitude measurements were made at various points on the acoustitron with of a DISA 55X Laser Doppler Vibrometer (LDV).

An LDV is a device that permits non-contact measurements of the component of velocity in the direction of a laser beam originating in a He-Ne laser. The initial beam is split into two beams of approximately the same intensity, where one beam is used as a reference and the other beam is focused on the vibrating object. The light reflected from the moving surface is collimated and sent to the detector. This beam is then recombined with the reference beam in opto-electronic circuitry that produces an electrical signal proportional to the surface velocity. This signal is multiplied by a given calibration constant to yield the absolute surface velocity component along the

laser beam.

The signal analyzer operating in swept sine mode was used to drive a single element of the acoustitron. The LDV was then used to measure the velocity amplitude of the driving element as well as the tube wall at three different positions as indicated in Fig. 3.5.

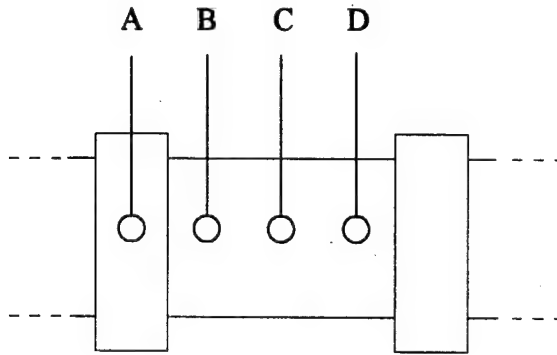


Figure 3.5: Location of four positions from which velocity amplitude measurements were taken using the LDV. Position A was the driving element.

The resulting velocity measurements are shown in Fig. 3.6.

At frequencies much less than modal frequencies of the piezoceramic element, the expected displacement amplitude  $D$  is given by its static value  $D_s$ , i.e. [45]

$$D_s = d_{33}V, \quad (3.4)$$

where  $d_{33}$  is the ratio of strain and applied field in the radial direction given in Table 3.2, and  $V$  is the amplitude of the driving voltage. Thus, for a constant driving voltage, no frequency dependence in  $D$  is expected. Taking the velocity and dividing

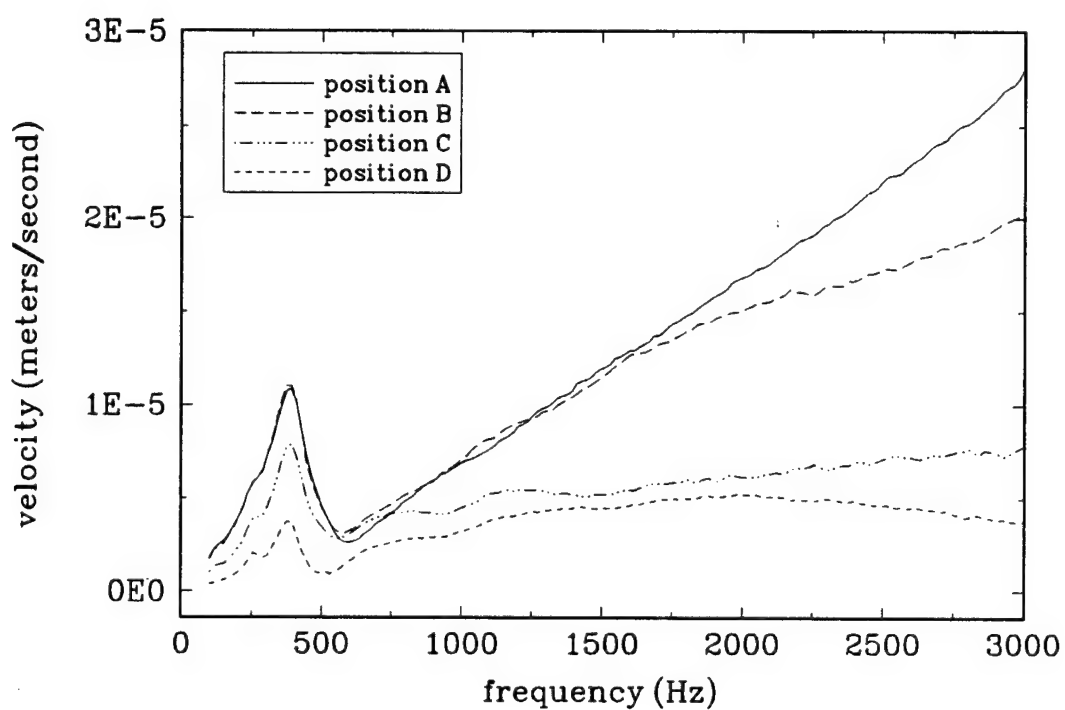


Figure 3.6: Velocity amplitude of driver and wall measured at four different positions. Data was taken with a 1 volt driving signal.

by the driving frequency  $\omega$ , yields the displacement  $D$  which is shown in Fig. 3.7. The displacement calculated from Eq. (3.4) is shown in Fig. 3.7 along with the measured data taken with the LDV. Inspection of this figure shows that there is a resonance at low frequencies in the displacement of the driving element, as well as the tube wall. This resonance is assumed to be a mechanical resonance associated with the structure of the acoustitron. When considering the displacement amplitude of the tube, the fairly flat response observed at most frequencies of interest will be considered as representative of the motion. (This is done to simplify the comparison to theory.) Because of this approximation, there will be some discrepancies in the theory for the very lowest frequencies.

Approximating all but the lower frequencies in Fig. 3.7 with  $D = 1.0 \times 10^{-9}$  meters per volt, one can determine a value the velocity amplitude  $V_0$  for use Eq. (2.57) where,

$$V_0 = \omega D V. \quad (3.5)$$

This value will be a good representation of  $D$  at most frequencies in the range considered.

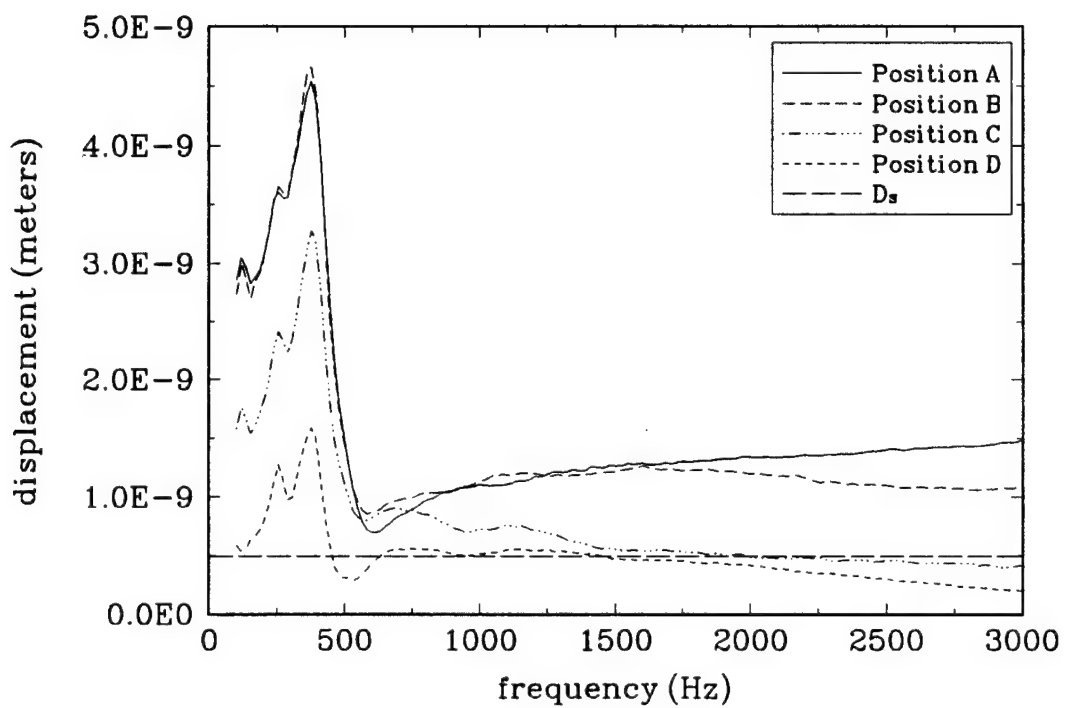


Figure 3.7: Displacement of driver and wall measured at four different positions. The theoretical displacement of the driving element based on piezoelectric properties is also shown. Data was taken with a 1 volt driving signal.

### 3.3.2 Attenuation in the Acoustitron

In order to determine the value of  $\alpha_{\text{CW}}$  given by Eq. (2.102), it was necessary to make measurements of the attenuation in the acoustitron. The acoustitron was driven so as to generate a traveling wave with a particular frequency. All elements of the acoustitron were then turned off simultaneously. The decay of the traveling wave with time was then observed and recorded with a digital oscilloscope. In order to verify the explanation of the observed resonance (see Section 2.4.2), measurements were also made on the PVC torus by recording the decay of standing waves produced by the single driving element. (This measurement was made this way because the construction of a second acoustitron was not feasible at the time.)

First consider the case of the acoustitron. In order to determine the absorption of sound, the natural logarithm of the sound pressure amplitude was plotted versus time. The absorption coefficient for the driving frequency was then found by

$$\alpha = \frac{|s|}{c}, \quad (3.6)$$

where  $s$  was the slope of the line from the semi-log plot, and  $c$  was the speed of sound. Measurements were made at the characteristic frequencies of the system setting  $\Omega = \Omega_0$ , where  $\Omega$  is the angular phase velocity from Chapter 2. The driving signal used was generated by the DSP, which was programmed to deactivate all thirty-two elements simultaneously. (An external source could not be used since the thirty-two elements would have been deactivated sequentially due to the nature of the driving circuit.)

For the case of the PVC torus, the decay of the sound pressure in time consisted of a number of cycles of equal amplitude, with each successive set “stepped” down

in amplitude (see Fig. 3.8). The absorption coefficient for the driving frequency was then determined by

$$\alpha = \ln \left( \frac{A_2}{A_1} \right) \frac{1}{C}, \quad (3.7)$$

where  $A_1$  and  $A_2$  were the amplitudes of adjacent steps with  $A_2 > A_1$ , and  $C$  was the circumference corresponding to  $R_0$  in Fig. 3.1. For this case, a function generator was used to generate the driving signal.

The results, as well as theory from Eq. (2.102), are plotted in Figs. 3.9 and 3.10. In order to compare the results of these two types of measurements, some standing wave values were measured driving a single element of the acoustitron. These are also shown in Fig. 3.9 and are similar to those measured from traveling waves.

The shift in resonance frequency between the PVC and Tygon® tubes can be attributed to a difference in Young's modulus in the two materials. The value of  $Y$  for the two materials is calculated using Eq. (2.103) along with measured values given in Table 3.3. The results are also give in Table 3.3, along with values of  $Y$  obtained by stretching strips of the material (Hooke's law experiment) and a value for Tygon® given by the manufacturer.

The dependence of the tube wall motion on the sound pressure amplitude inside the acoustitron can also be verified experimentally. In Fig. 3.11 are plotted the measured displacements of a single driving element in the acoustitron and a location on the tube wall between two elements. The frequencies are those that produce traveling waves in the acoustitron for  $\Omega = \Omega_0$  (indicated by the empty markers), as well as non-traveling waves (indicated by the solid markers). Also shown are the microphone voltage levels measured inside the device as a function of these same

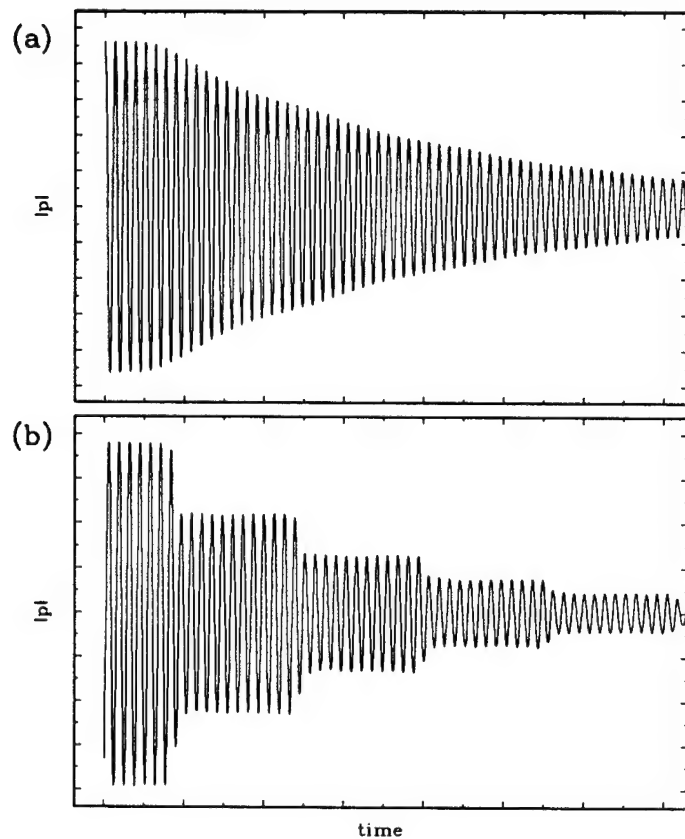


Figure 3.8: Examples of decay measured for the case of (a) a traveling wave in the acoustitron and (b) a standing wave produced by a single driving element. For the standing wave case, the driving frequency was twelve times the fundamental frequency and the microphone was located approximately opposite the driving element. Therefore the number of cycles in the first step is about six, and the remainder of the steps is exactly twelve. The driving frequency used in both cases was about 3900 Hz.

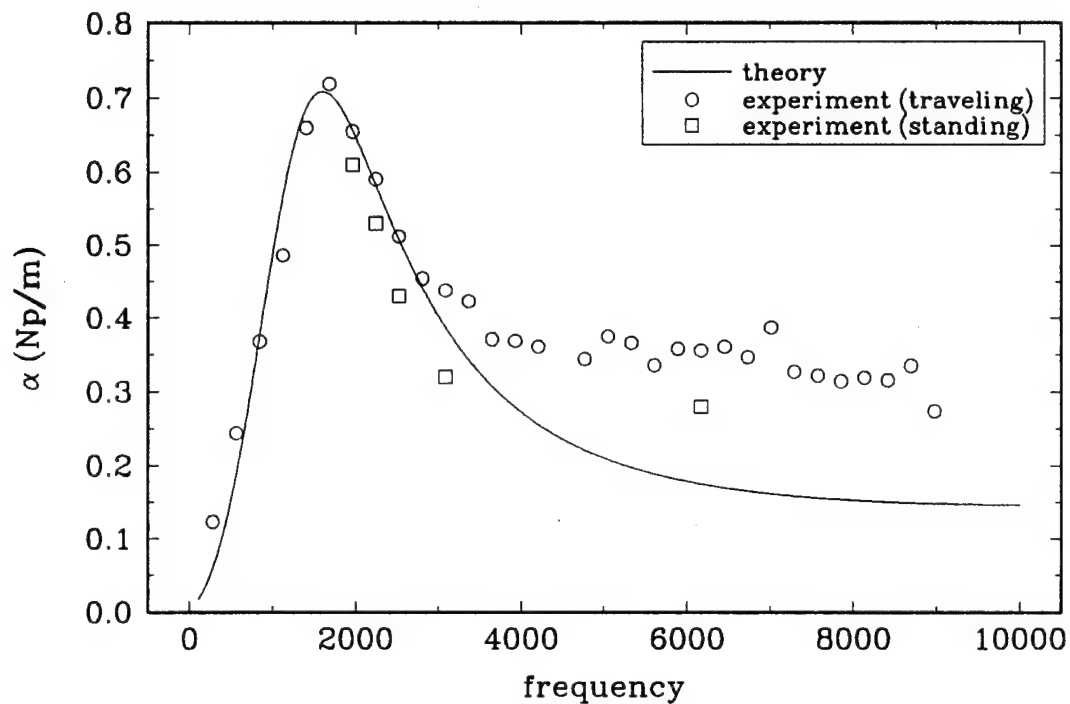


Figure 3.9: Measured values of absorption coefficient in the acoustitron along with theoretical curves from Eq. (2.102) based on the measured value of absorption at the resonance frequency. The frequencies plotted as circles correspond to traveling waves inside the acoustitron. Standing wave values are plotted as squares.

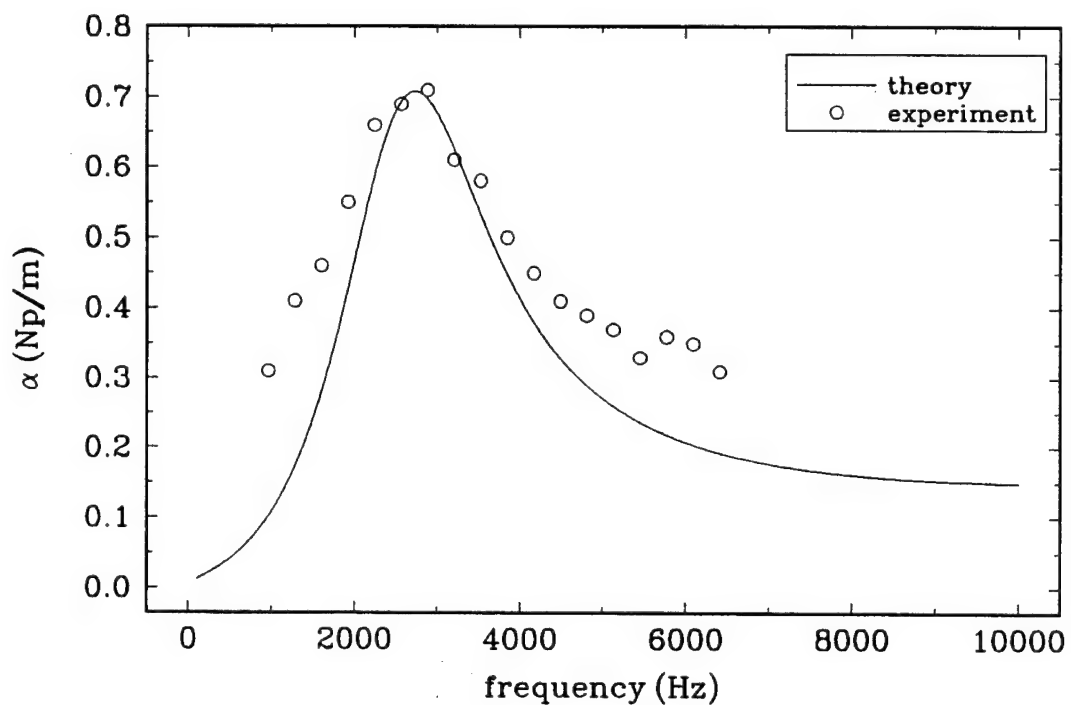


Figure 3.10: Measured values of absorption coefficient in the PVC torus along with theoretical curves from Eq. (2.102) based on the measured value of absorption at the resonance frequency. The frequencies plotted as circles correspond to characteristic frequencies.

Table 3.3: Experimentally determined parameters from measurements made on both the acoustitron (Tygon®) and PVC torus, along with manufacturers information. The value for attenuation measured at the resonance frequency given in the table excludes the tube effect.

	Parameter	acoustitron (Tygon®)	PVC torus
experiment	$f_0$ (Hz)	1683.1	2885.3
	$\alpha_{CW}^R$ (Np m <sup>-1</sup> )	0.67	0.65
	$\rho_w$ (kg m <sup>-3</sup> )	—	1185
	$Y$ ( $\times 10^6$ N m <sup>-2</sup> )	$3.32 \pm 0.20$	$34.3 \pm 3.3$
calculated [Eq. (2.103)]	$Y$ ( $\times 10^6$ N m <sup>-2</sup> )	$23.9 \pm 7.89$	$70.6 \pm 23.3$
manufacturer	$Y$ ( $\times 10^6$ N m <sup>-2</sup> )	$5.37 \pm 0.14$	—
	$\rho_w$ (kg m <sup>-3</sup> )	1180	—

frequencies. Inspection of this figure shows that the motion of the tube wall does follow the sound pressure amplitude inside the acoustitron for a relatively constant driver displacement. The resonance frequency seen in Fig. 3.9 also appears as a resonance in the displacement of the tube wall.

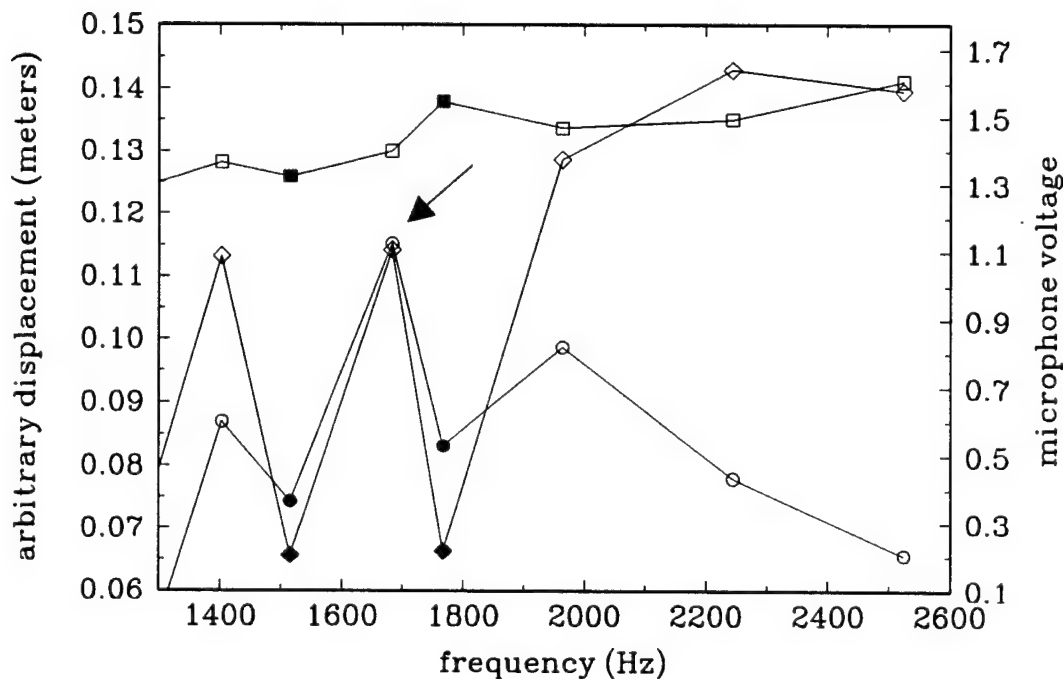


Figure 3.11: Displacement of a driving element (square markers) and the tube wall (circular markers) while driving the acoustitron at traveling wave frequencies. The measured microphone voltage (diamond markers) is also shown. The resonance in the motion of the tube wall is indicated by the arrow.

### 3.3.3 Pressure Distribution in the Acoustitron with a Delta Function Driver

To verify Eq. (2.42), the PVC torus was used. By moving the single driving element around the circumference of the tube while making measurements with a fixed microphone inside the tube, the sound pressure level could be mapped out as a function of angular position.

The element was driven with a function generator set to the desired driving frequency and the microphone output was monitored using a digital oscilloscope set to average the incoming data. Measurements were made at intervals of  $10^\circ$  along the entire circumference of the torus. Since the pressure amplitude in the tube was symmetric about the driving element, corresponding data from both sides were averaged together to form a pressure map for the range  $-\pi \leq \theta = 0$ . Two different driving frequencies were used corresponding to the third and fourth characteristic frequency.

In order to make a qualitative comparison, theoretical data was normalized to fit a single experimental data point. The measured and predicted responses of the system as a function of position are shown in Figs. 3.12 and 3.13.

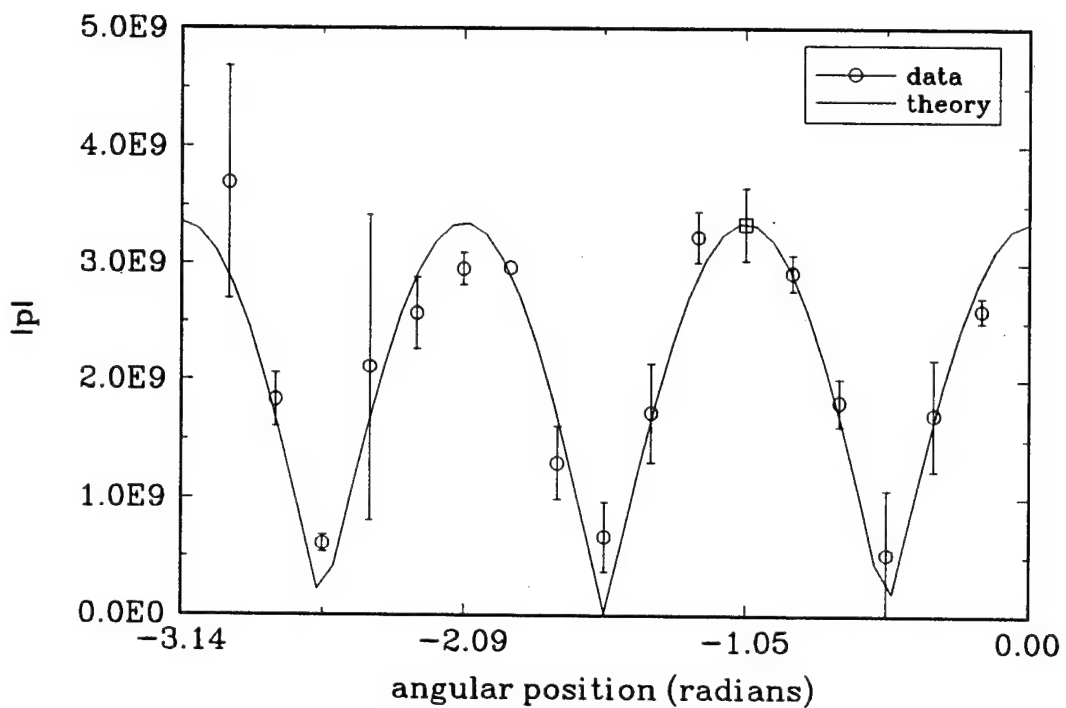


Figure 3.12: Normalized microphone voltage levels for driver element positions ranging from  $-\pi \leq \phi \leq 0$ ; the normalized data point is indicated by the square marker. The solid curve is that given by Eq. (2.45). The microphone was located at  $\phi = 0$ , and data points were spaced in increments of  $10^\circ$ . The driving frequency was 841.5 Hz.

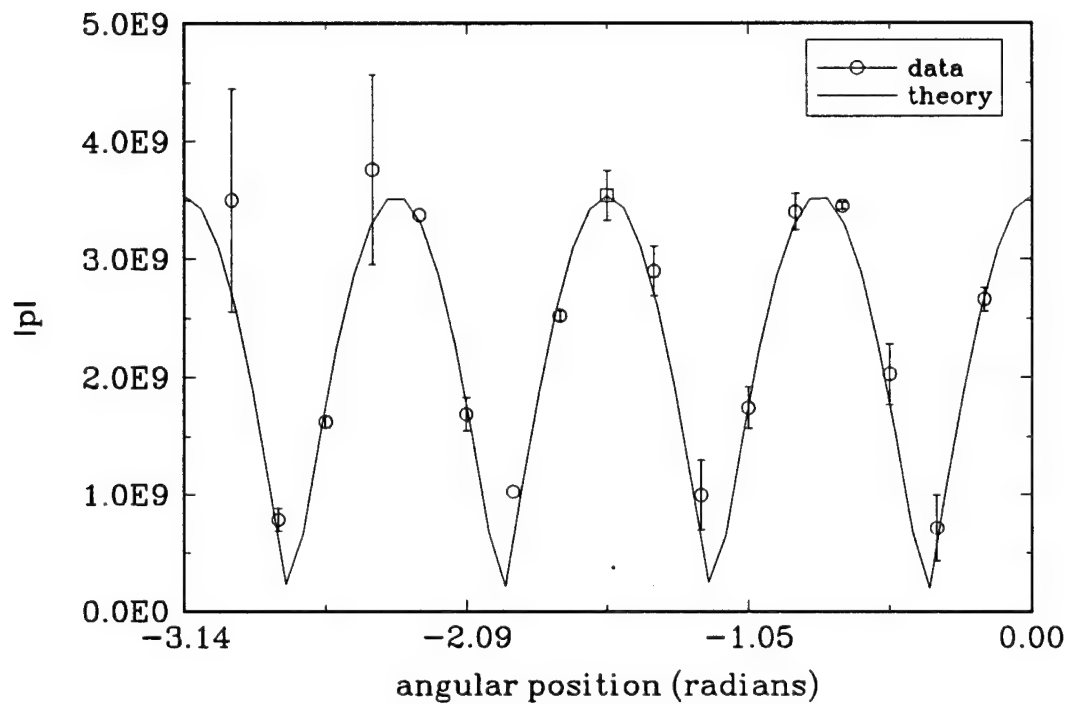


Figure 3.13: Normalized microphone voltage levels for driver element positions ranging from  $-\pi \leq \phi \leq 0$ ; the normalized data point is indicated by the square marker. The solid curve is that given by Eq. (2.45). The microphone was located at  $\phi = 0$ , and data points were spaced in increments of  $10^\circ$ . The driving frequency was 1122.0 Hz.

### 3.3.4 Sound Pressure Measurements Inside the Acoustitron

Measurements of the pressure amplitude as a function of frequency and  $\Omega$  were made with the acoustitron. The signal analyzer operating in swept sine mode was used to record the output of the microphone. These measurements are shown in Figs. 3.14 and 3.15. The SPL was measured with a calibrated microphone. (The sweep rate was slow enough to allow the system to reach a steady state pressure at each frequency.) The driving voltage amplitude was 16.72 volts rms. For all these measurements, the microphone was located at  $\theta = 0$

As pointed out in the theory, the peaks in the response of the acoustitron correspond to the characteristic frequencies of a rigid wall toroid with identical dimensions. From the frequency positions of the peaks and the known circumference of the acoustitron, the intrinsic speed of sound in the fluid can be determined using Eqs. (2.9) and (2.12). Comparison of Figs. 3.14 and 3.15 to Figs. 2.7 and 2.8 shows that the theory correctly predicts the relative behavior of the sound pressure for the various values of frequency and  $\Omega$ , specifically the asymmetric shifting to the left and right of the peak for  $\Omega < \Omega_0$  and  $\Omega > \Omega_0$  respectively. The experimental data will now be examined more closely to determine how well it matches the theory.

The theoretical equation for the pressure is given by Eq. (2.57) for the case of an inviscid fluid, where  $V_0$  is the velocity amplitude of the wall. The measured displacement amplitude at points along the wall (Fig. 3.7) show a definite frequency dependence of the amplitude of the motion, especially at low frequencies. It is also apparent that the motion of the wall varies with the distance from the driving element. For these reasons, it is advantageous to eliminate  $V_0$  from the experimental data in

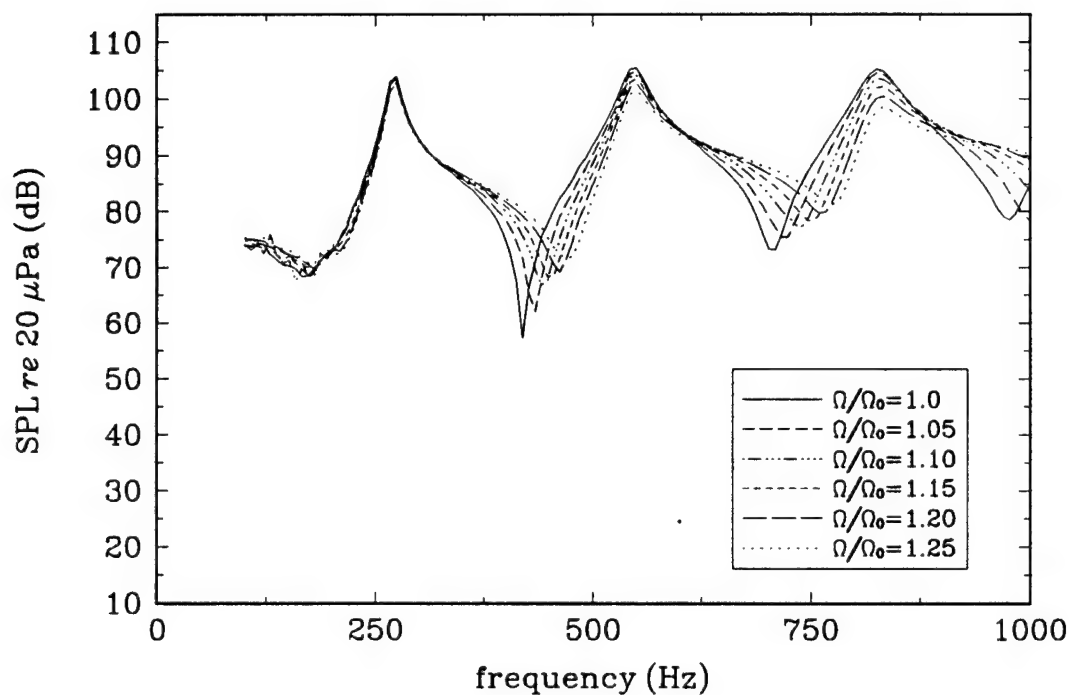


Figure 3.14: Measured values of the sound pressure levels inside the acoustitron for values of  $\Omega/\Omega_0 \geq 1.0$ . The driving voltage was 16.72 volts rms.

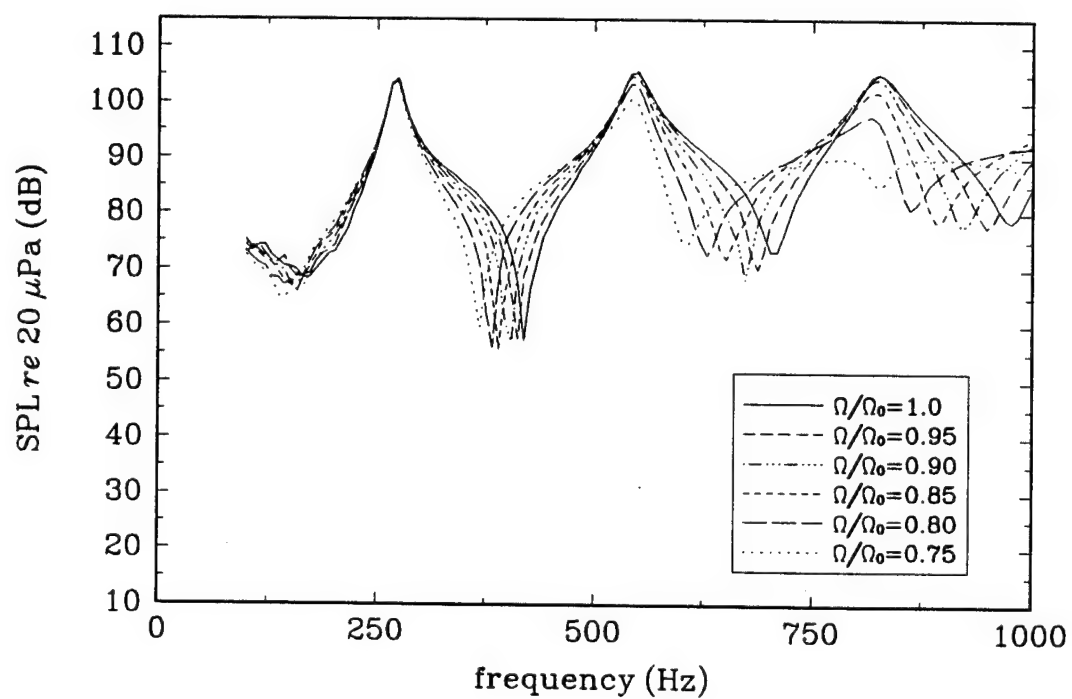


Figure 3.15: Measured values of the sound pressure levels inside the acoustitron for values of  $\Omega/\Omega_0 \leq 1.0$ . The driving voltage was 16.72 volts rms.

order to facilitate a comparison to theory. Therefore, the measured and predicted values of pressure were normalized by the pressure for the case of  $\Omega = \Omega_0$ , that is  $P(\Omega)/P(\Omega_0)$ , where theory was normalized by theory and experiment was normalized by experiment. The choice to normalize by the pressure for the case of  $\Omega = \Omega_0$  was arbitrary. In Figs. 3.16–3.25, the normalized pressure amplitude for both experimental and theoretical values are plotted as a function of frequency for values of  $\Omega$  ranging from 0.75 to 1.25. The theoretical pressures shown are for the case of an inviscid fluid with an identical frequency resolution as that of the experimental data. The effect of the lossless fluid produces peaks that are for the most part, taller than the measured data for a tube with losses. The exception to this is the peak corresponding to the first harmonic of the fundamental frequency. From the measured velocity amplitude of the tube shown in Fig. 3.6, it is evident that a resonance in the driving system exists around the frequency in question. Since there is a mechanical resonance, the theoretical curves, which assume constant amplitude boundary conditions, will not show this behavior.

To see how well the theory predicts the SPL measured in the acoustitron, the theoretical pressure for a lossless fluid filled tube [Eq. (2.57)] will be used and attenuation will be included by writing the pressure in terms of a complex wave number  $\bar{k}$  and speed of sound  $\bar{c}$  where

$$\bar{k} = \omega \bar{c}, \quad (3.8)$$

and  $\bar{k}$  is given by Eq. (2.84), and the absorption  $\alpha$  is given by Eqs. (2.85), (2.87), and (2.102). The value of  $\alpha_{CW}$  can be determined from the measured values given in Table 3.3. A value for  $V_0$  is obtained from Eq. (3.5) with  $V = 16.72$  volts rms.

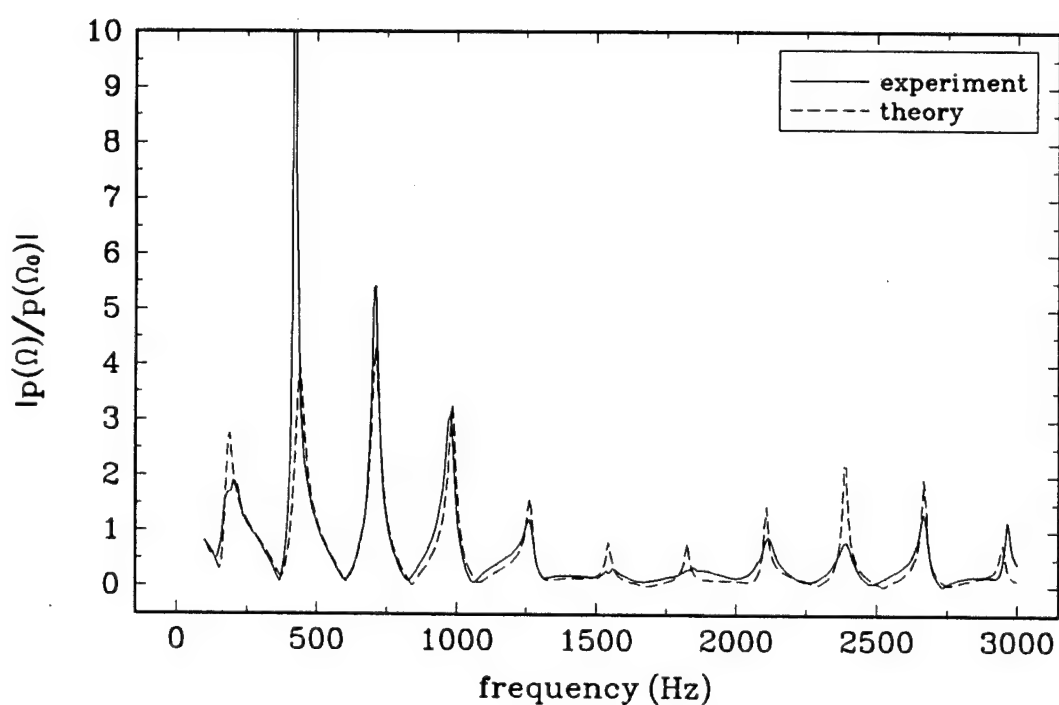


Figure 3.16: Comparison of theoretical and experimental values of the normalized sound pressure amplitude in the acoustitron as a function of frequency for  $\Omega/\Omega_0 = 0.75$ . The normalization pressure is that for  $\Omega = \Omega_0$ .

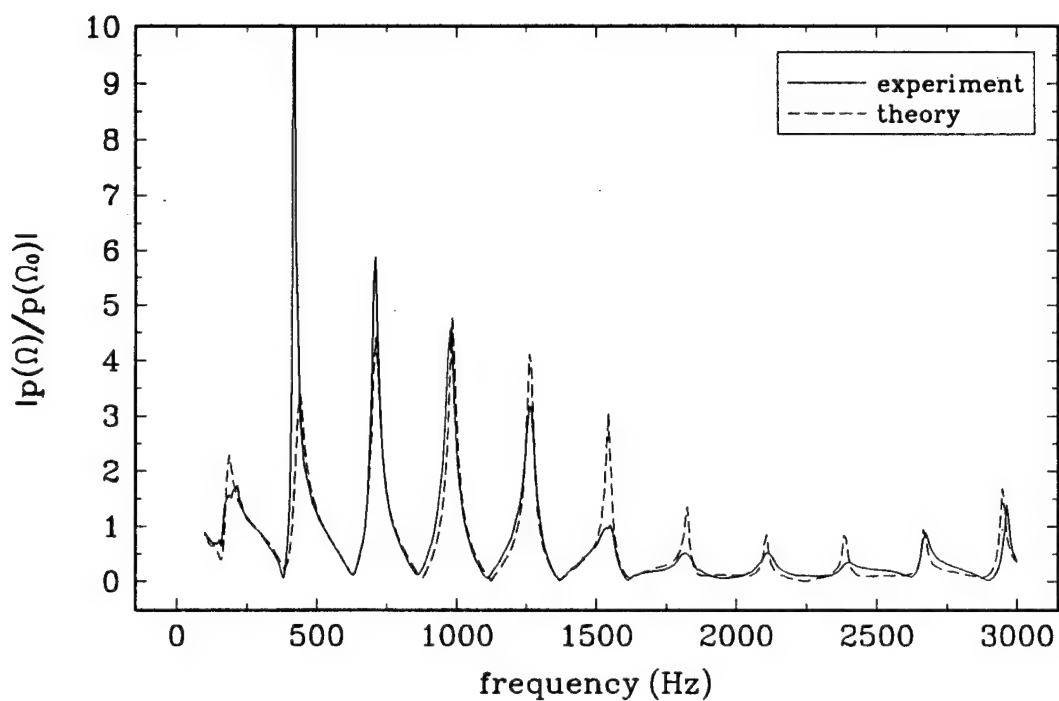


Figure 3.17: Comparison of theoretical and experimental values of the normalized sound pressure amplitude in the acoustitron as a function of frequency for  $\Omega/\Omega_0 = 0.80$ . The normalization pressure is that for  $\Omega = \Omega_0$ .

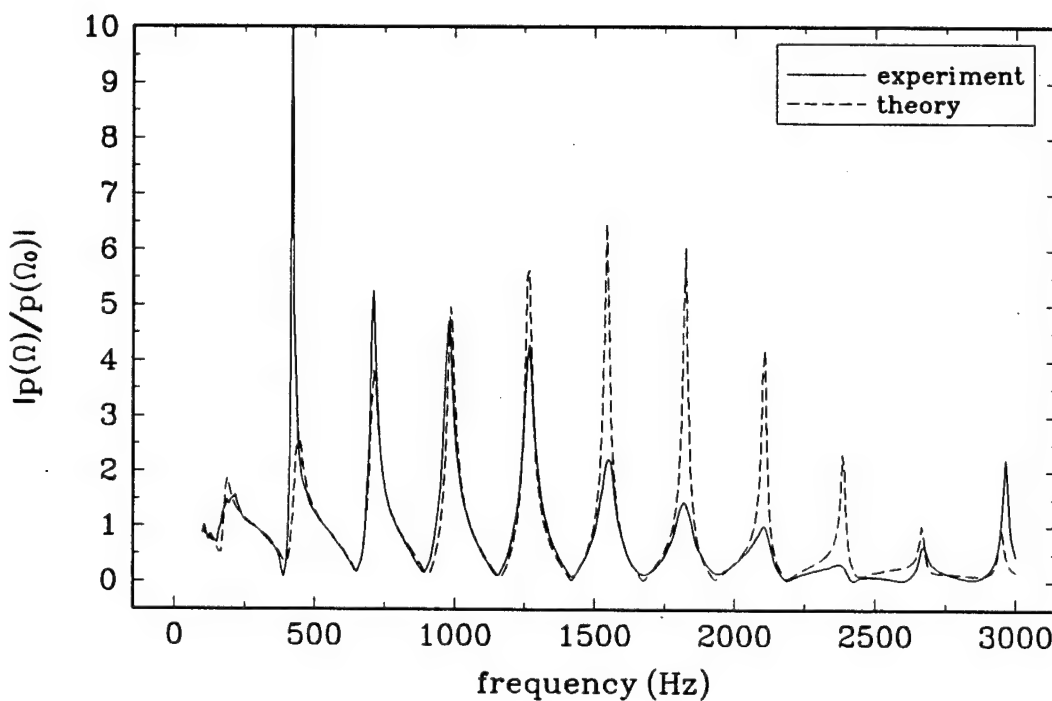


Figure 3.18: Comparison of theoretical and experimental values of the normalized sound pressure amplitude in the acoustitron as a function of frequency for  $\Omega/\Omega_0 = 0.85$ . The normalization pressure is that for  $\Omega = \Omega_0$ .

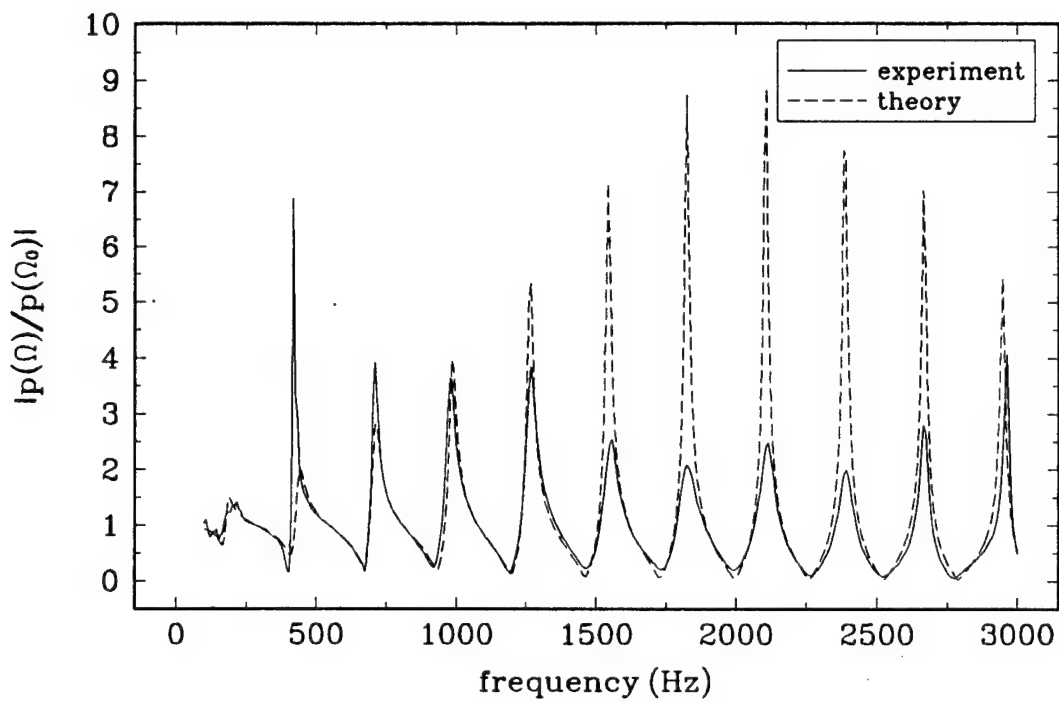


Figure 3.19: Comparison of theoretical and experimental values of the normalized sound pressure amplitude in the acoustitron as a function of frequency for  $\Omega/\Omega_0 = 0.90$ . The normalization pressure is that for  $\Omega = \Omega_0$ .

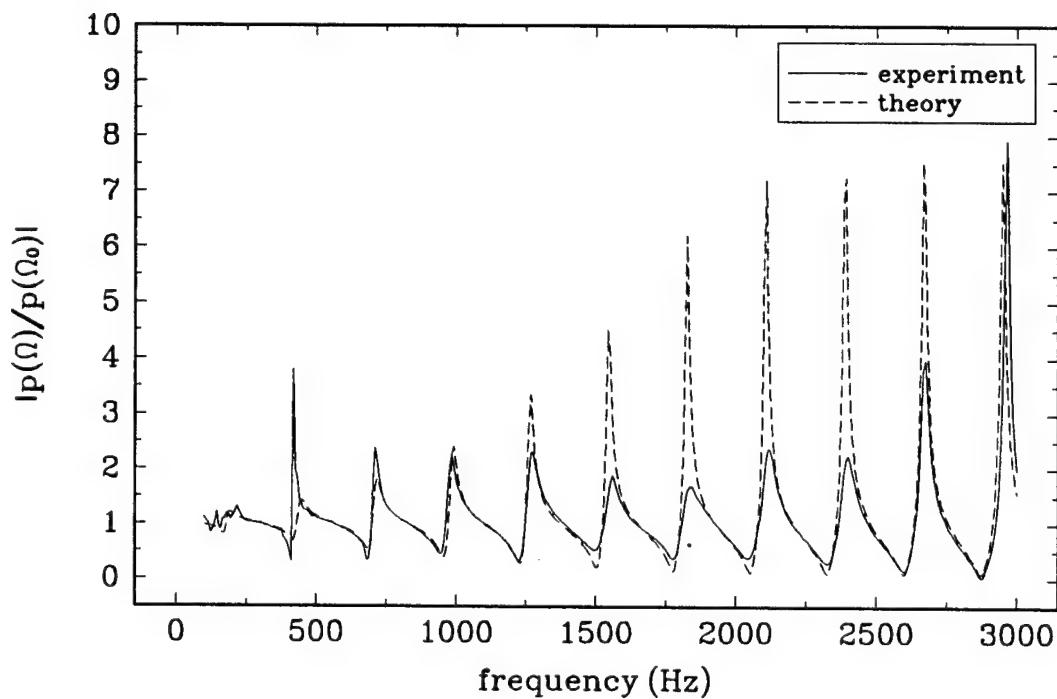


Figure 3.20: Comparison of theoretical and experimental values of the normalized sound pressure amplitude in the acoustitron as a function of frequency for  $\Omega/\Omega_0 = 0.95$ . The normalization pressure is that for  $\Omega = \Omega_0$ .

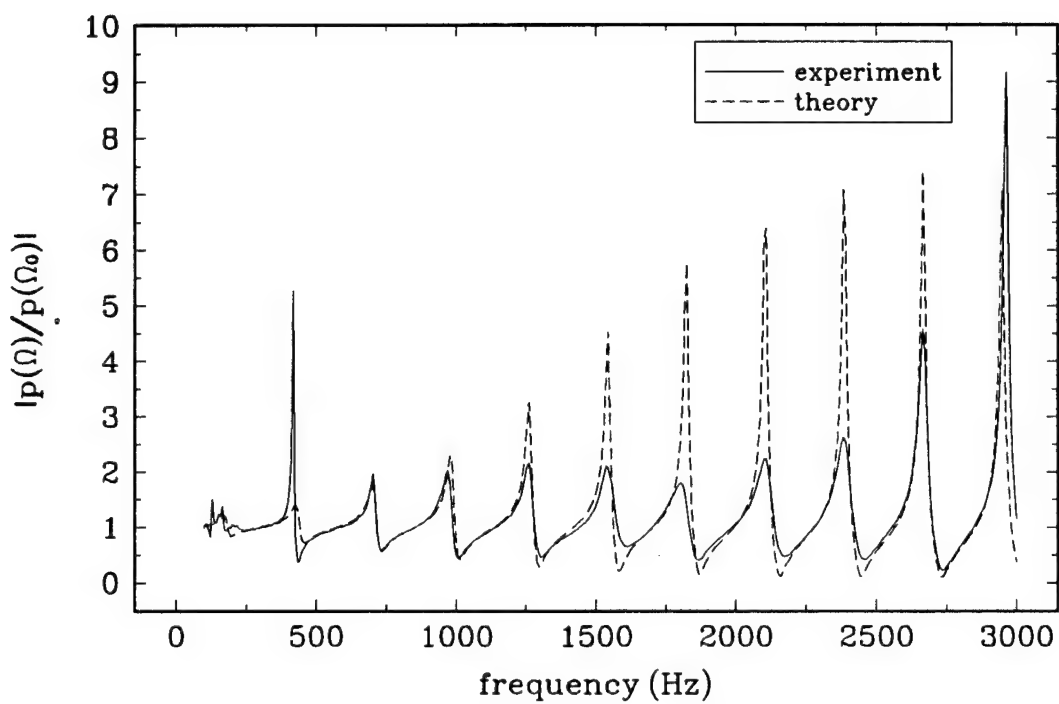


Figure 3.21: Comparison of theoretical and experimental values of the normalized sound pressure amplitude in the acoustitron as a function of frequency for  $\Omega/\Omega_0 = 1.05$ . The normalization pressure is that for  $\Omega = \Omega_0$ .

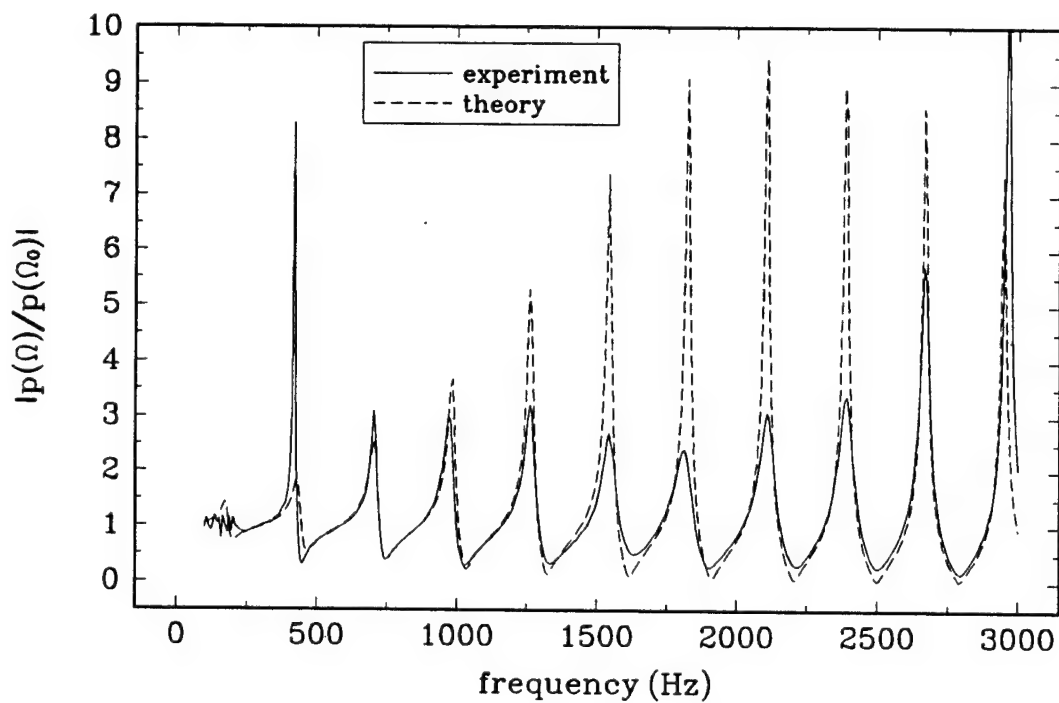


Figure 3.22: Comparison of theoretical and experimental values of the normalized sound pressure amplitude in the acoustitron as a function of frequency for  $\Omega/\Omega_0 = 1.10$ . The normalization pressure is that for  $\Omega = \Omega_0$ .

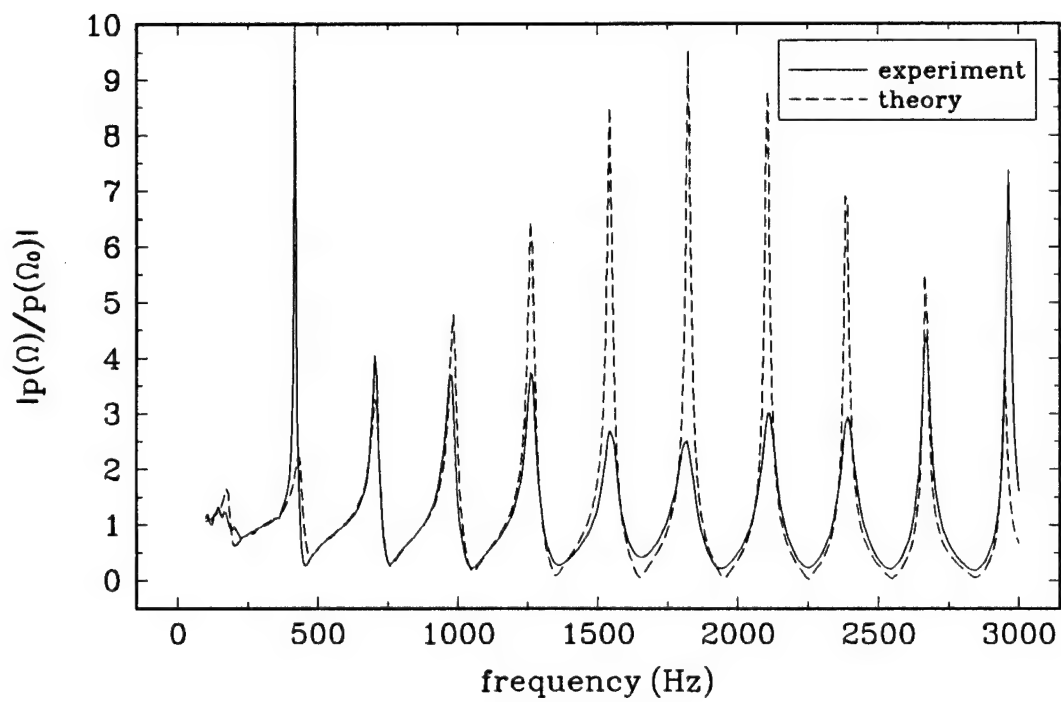


Figure 3.23: Comparison of theoretical and experimental values of the normalized sound pressure amplitude in the acoustitron as a function of frequency for  $\Omega/\Omega_0 = 1.15$ . The normalization pressure is that for  $\Omega = \Omega_0$ .

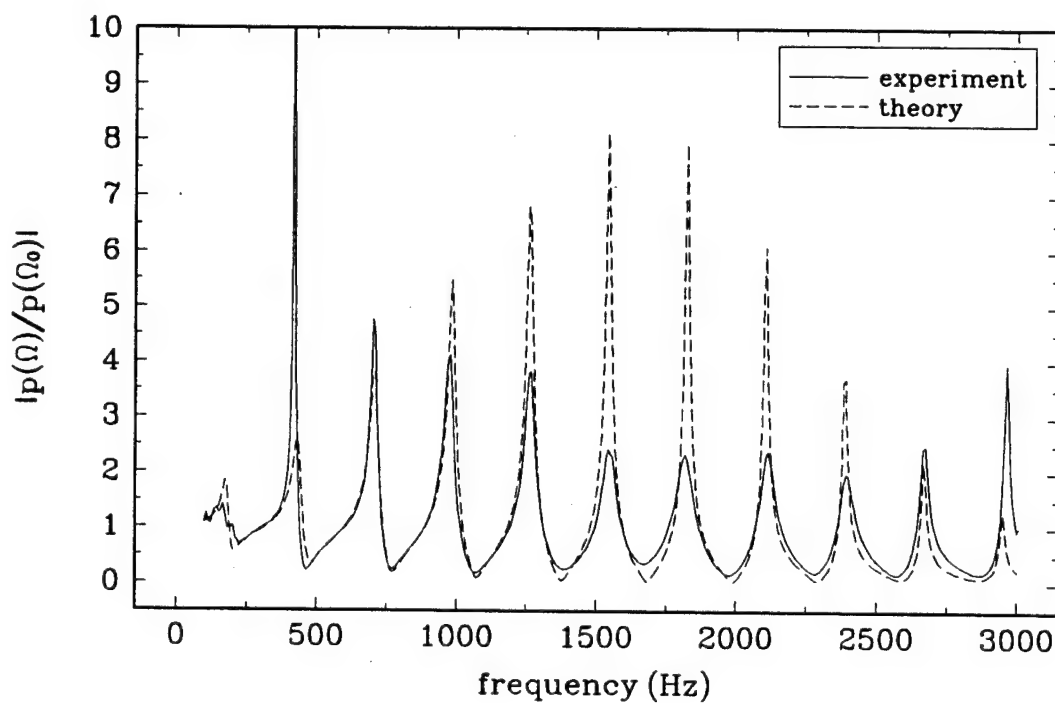


Figure 3.24: Comparison of theoretical and experimental values of the normalized pressure amplitude as a function of frequency for  $\Omega/\Omega_0 = 1.20$ . The normalization pressure is that for  $\Omega = \Omega_0$ .

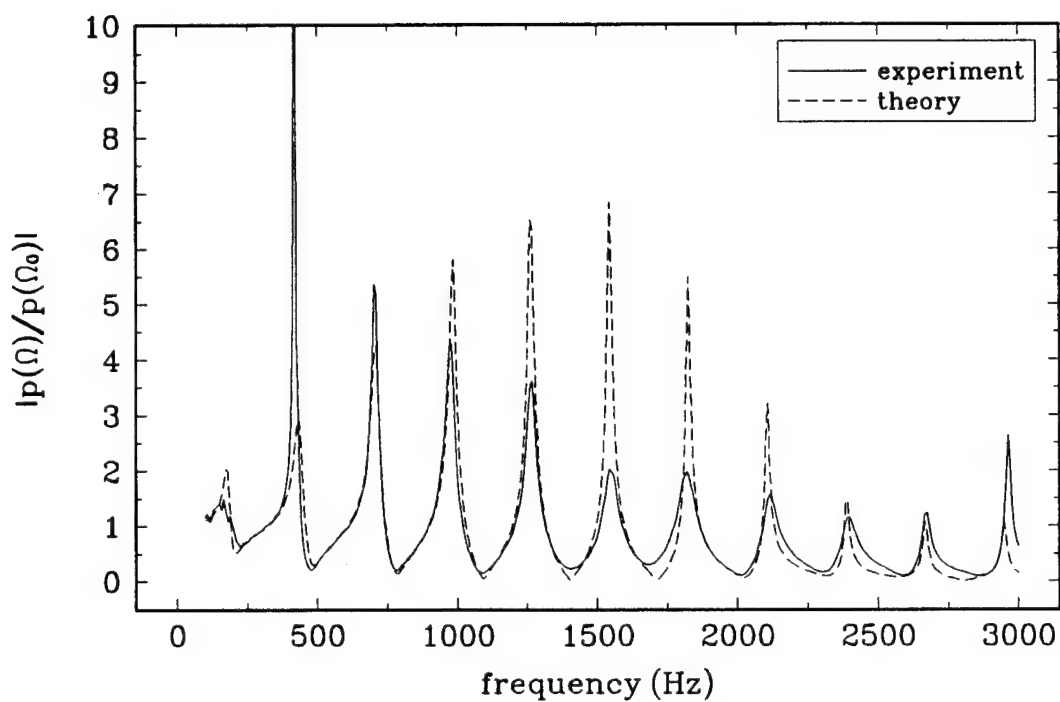


Figure 3.25: Comparison of theoretical and experimental values of the normalized pressure amplitude as a function of frequency for  $\Omega/\Omega_0 = 1.25$ . The normalization pressure is that for  $\Omega = \Omega_0$ .

The resulting SPLs as functions of frequency for the values of  $\Omega$  already considered are shown in Figs. 3.26–3.36. For  $\Omega \geq \Omega_0$ , the predicted SPL matches the measured SPL quite well for all frequencies. For  $\Omega < \Omega_0$ , theoretical and experimental data match well for low frequencies, but deviations are apparent at higher frequencies; the lower the  $\Omega$ , the more the deviation. The reason for this is as follows. Recall that the boundary condition used in the theoretical case was that of a continuously driven wall where the wave number in the fluid was equal to the wave number in the wall. In the experimental tube, however, driving elements are spaced a finite distance apart. As  $\Omega$  decreases, the speed of the wave in the wall decreases, and for a fixed frequency, the wavelength decreases. This means that there are fewer elements per wavelength so that the wall appears more like a series of point drivers separated by passive walls instead of a continuously driven wall derived in theory. If the minimum number of elements that could represent a sine wave is considered, it would be four elements per wavelength. Therefore, frequencies that correspond to three or fewer elements per wavelength in the acoustitron, would not be well represented by theory. In Table 3.4, frequencies at which there are only three elements per wavelength corresponding to the angular phase velocity of the driven wall are given. Comparing these values to the results shown in Figs. 3.26–3.31, it can be seen that the experimental measurements do seem to deviate more above these frequencies.

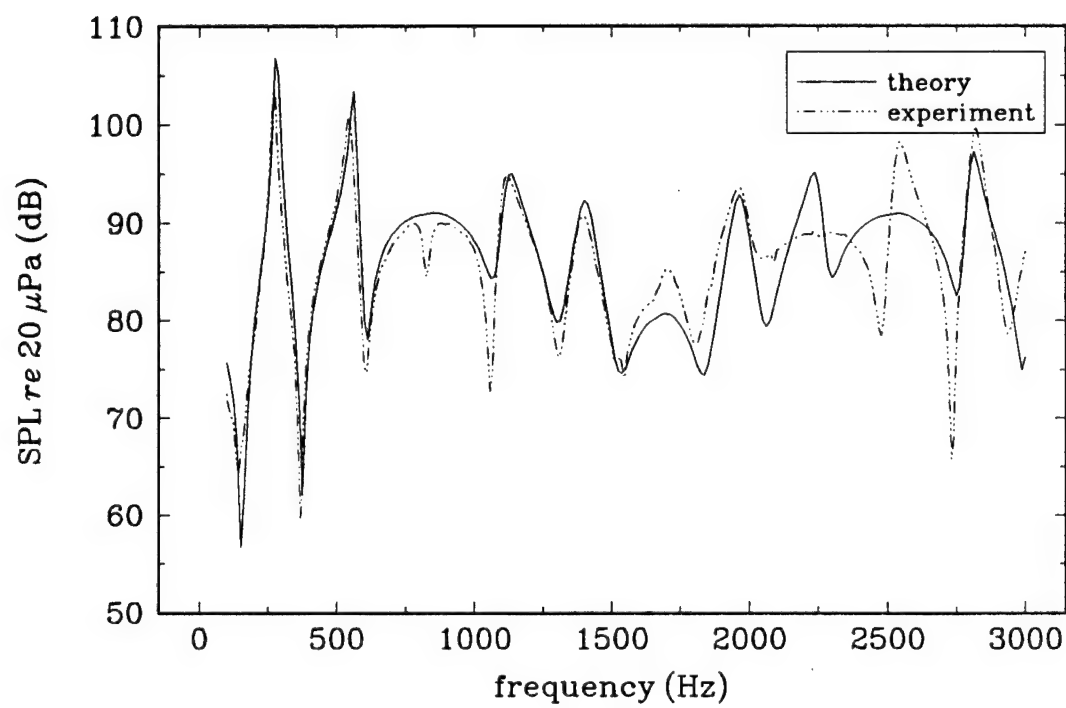


Figure 3.26: Comparison of predicted to measured values of the sound pressure level inside the acoustitron for  $\Omega/\Omega_0 = 0.75$ .

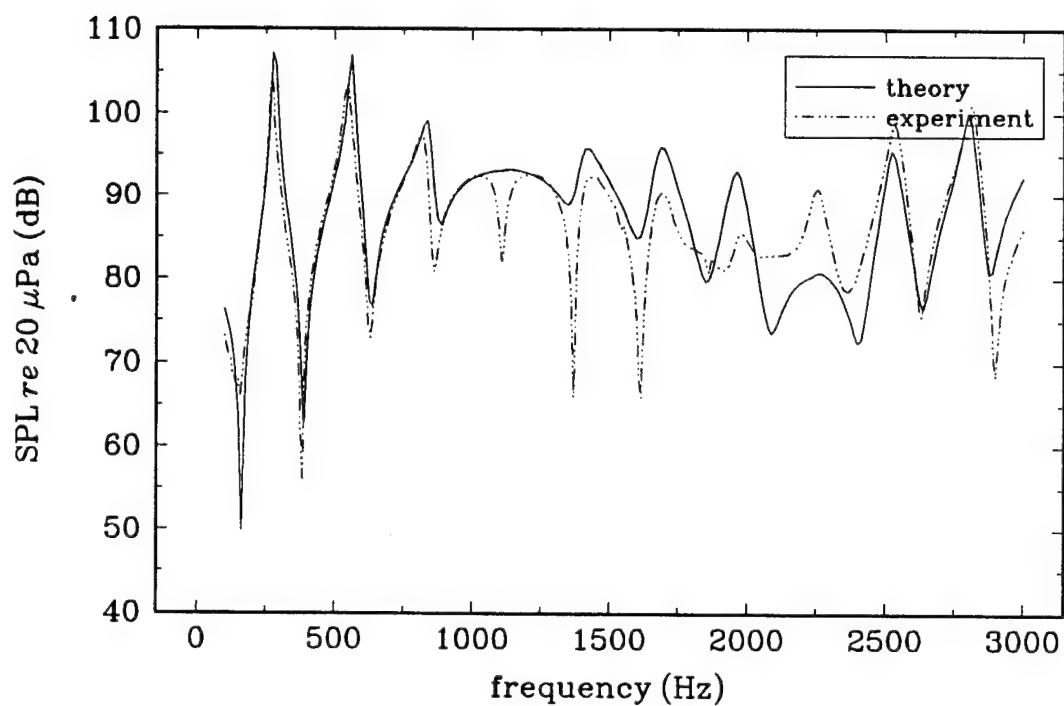


Figure 3.27: Comparison of predicted to measured values of the sound pressure level inside the acoustitron for  $\Omega/\Omega_0 = 0.80$ .

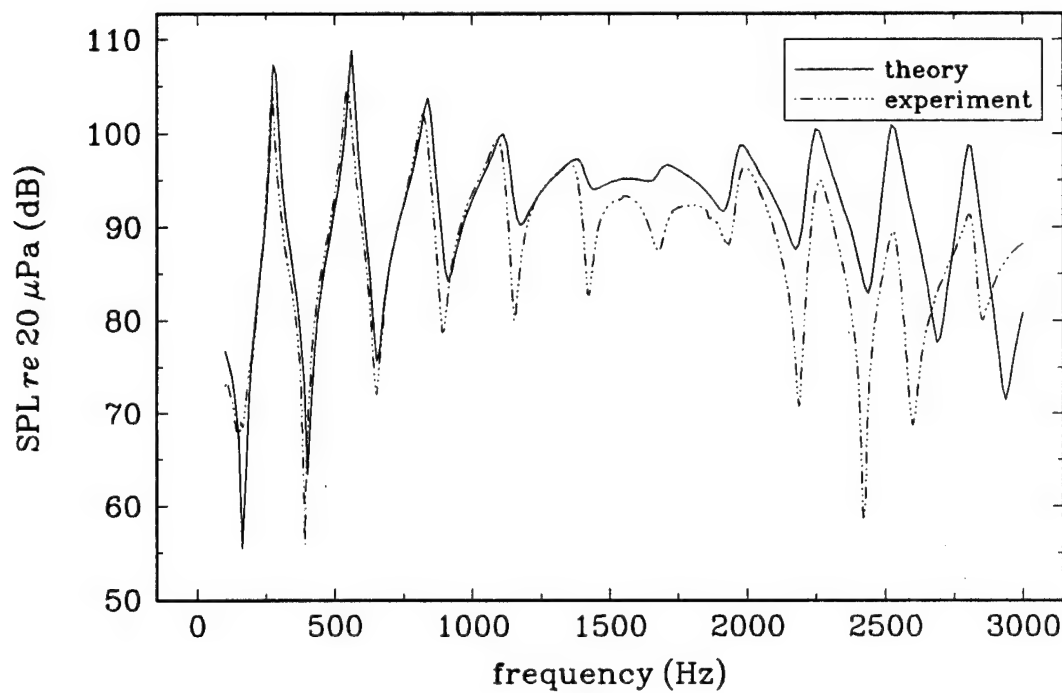


Figure 3.28: Comparison of predicted to measured values of the sound pressure level inside the acoustitron for  $\Omega/\Omega_0 = 0.85$ .

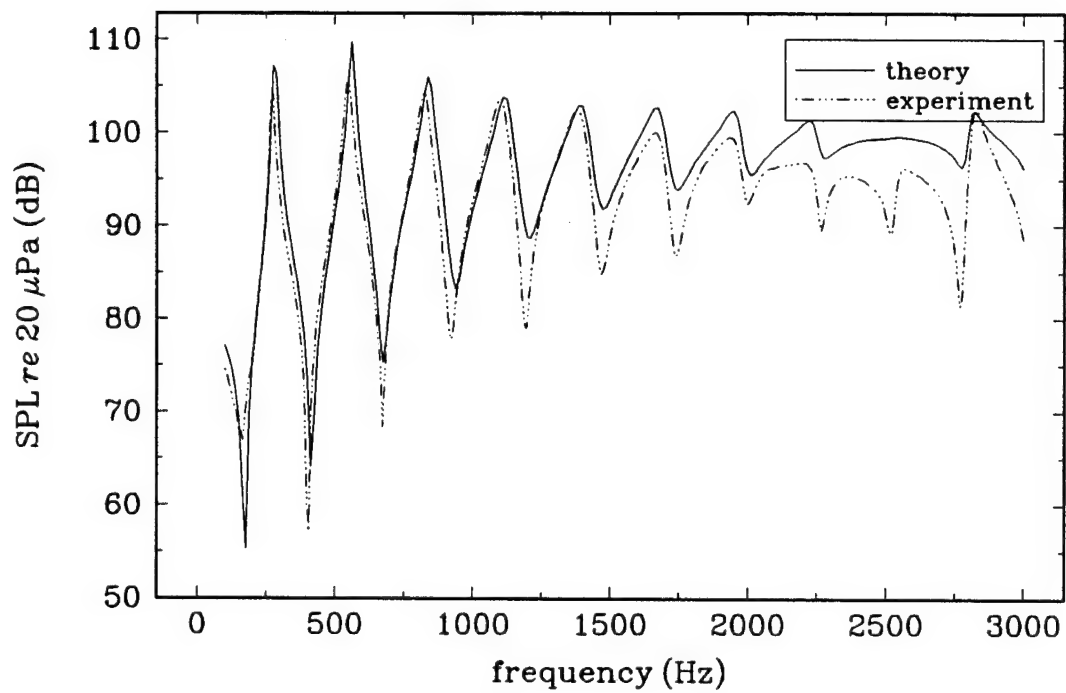


Figure 3.29: Comparison of predicted to measured values of the sound pressure level inside the acoustitron for  $\Omega/\Omega_0 = 0.90$ .

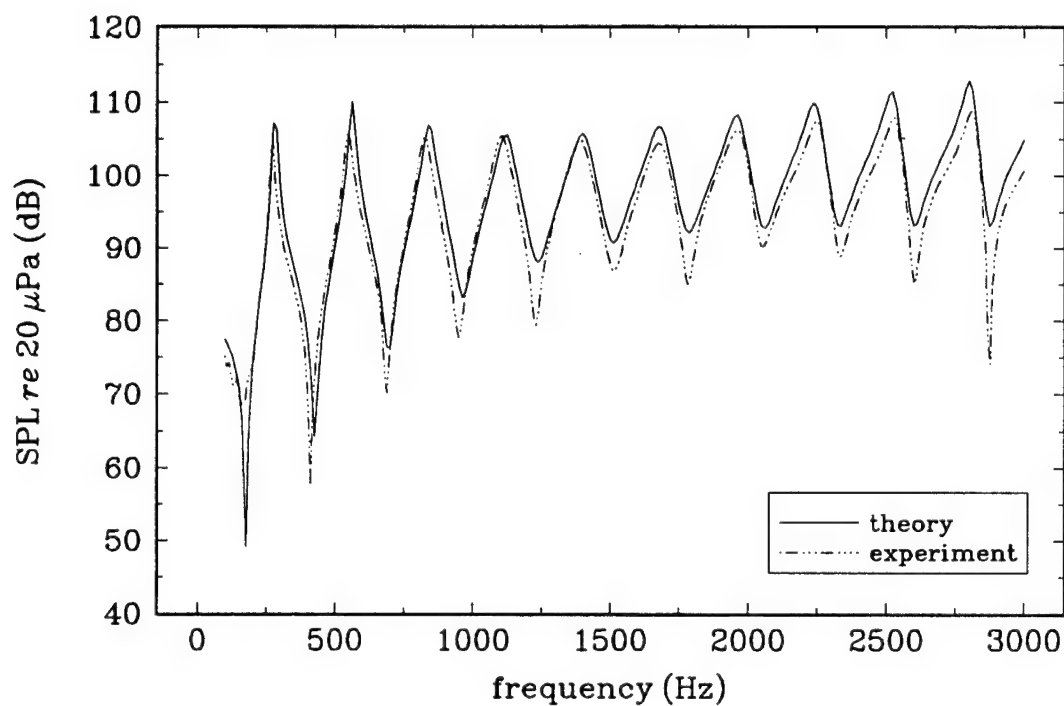


Figure 3.30: Comparison of predicted to measured values of the sound pressure level inside the acoustitron for  $\Omega/\Omega_0 = 0.95$ .

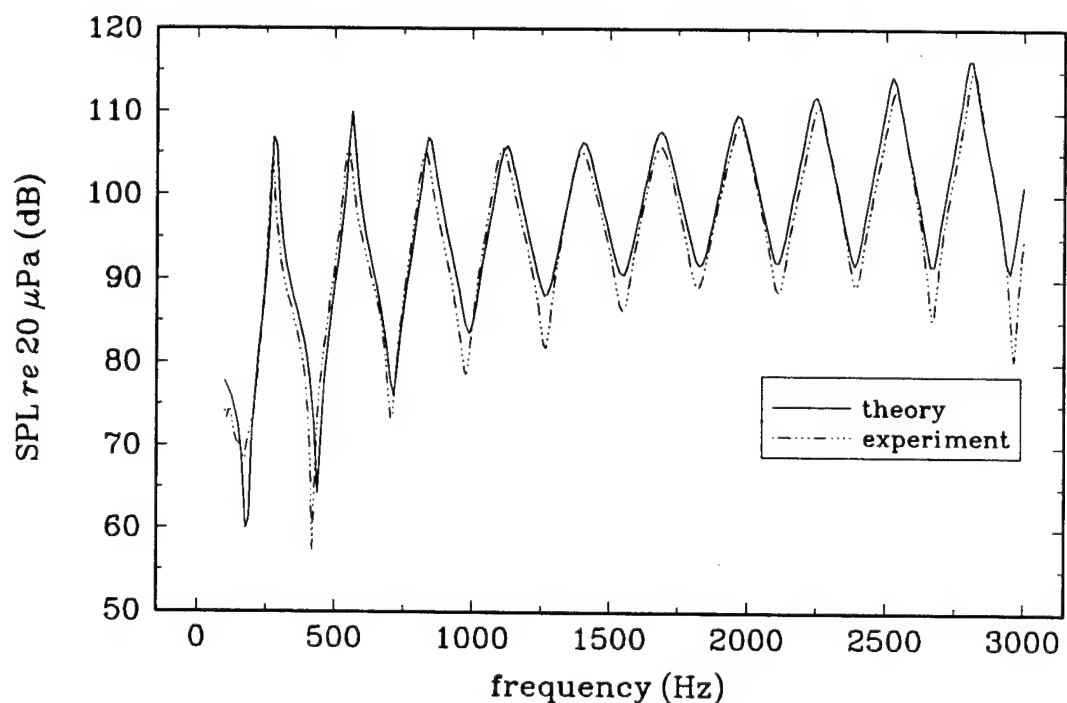


Figure 3.31: Comparison of predicted to measured values of the sound pressure level inside the acoustitron for  $\Omega/\Omega_0 = 1.00$ .

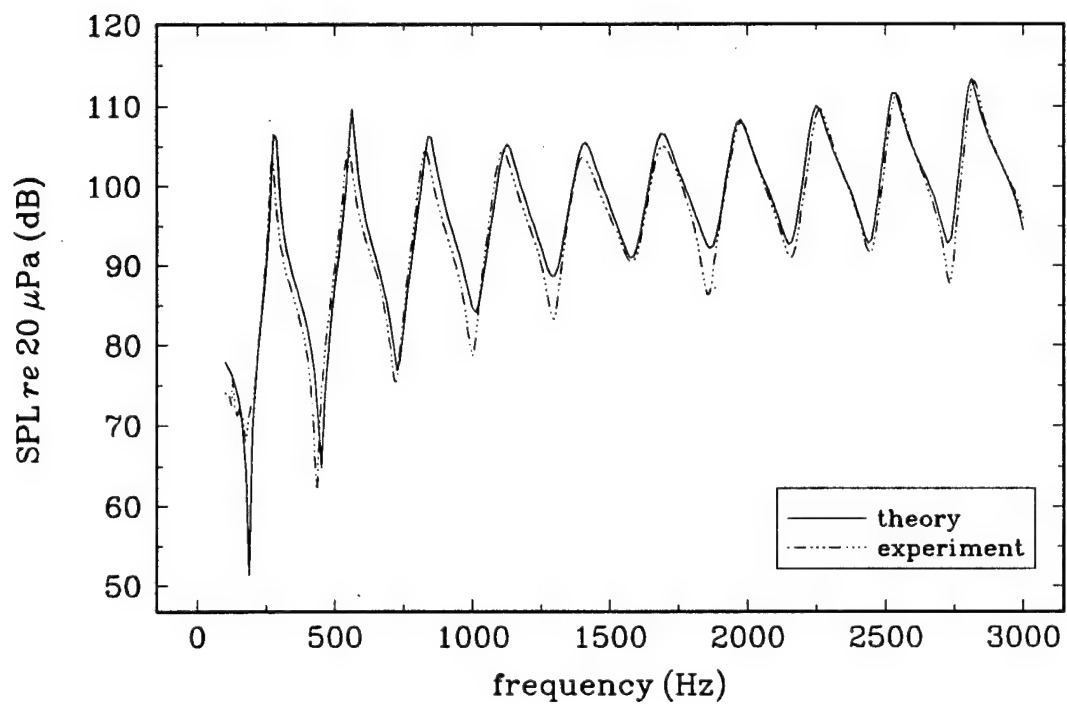


Figure 3.32: Comparison of predicted to measured values of the sound pressure level inside the acoustitron for  $\Omega/\Omega_0 = 1.05$ .

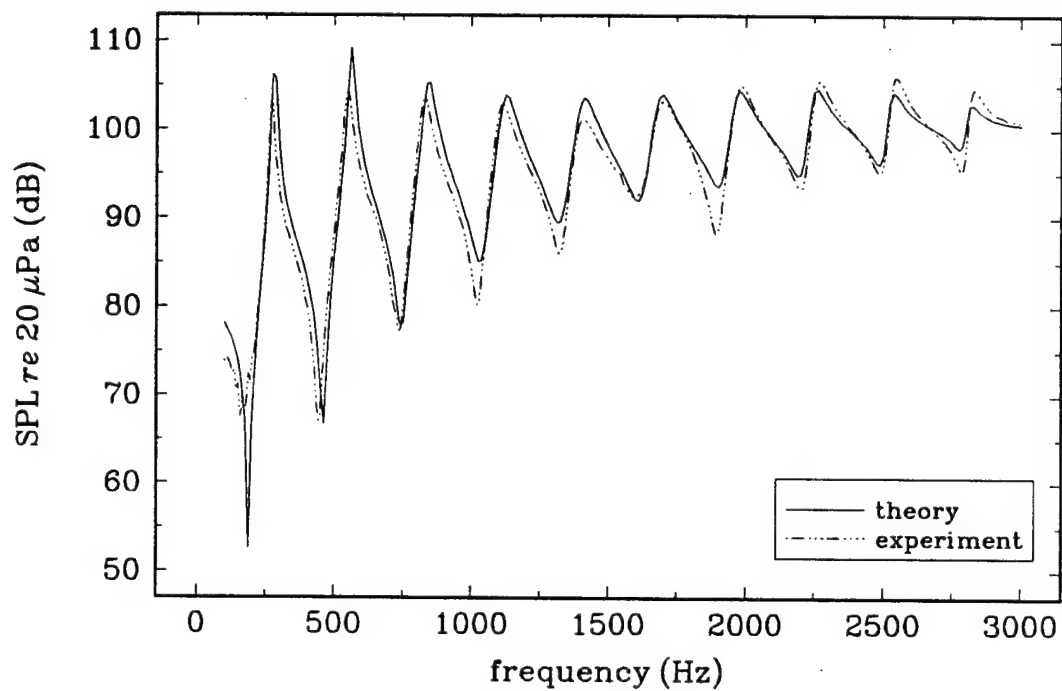


Figure 3.33: Comparison of predicted to measured values of the sound pressure level inside the acoustitron for  $\Omega/\Omega_0 = 1.10$ .

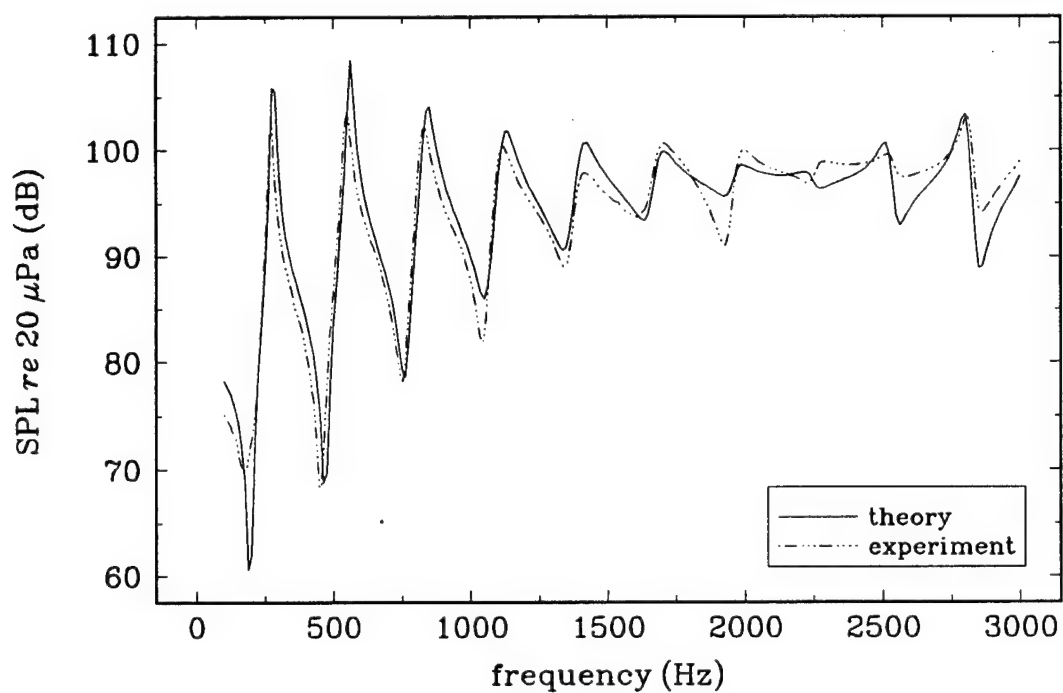


Figure 3.34: Comparison of predicted to measured values of the sound pressure level inside the acoustitron for  $\Omega/\Omega_0 = 1.15$ .

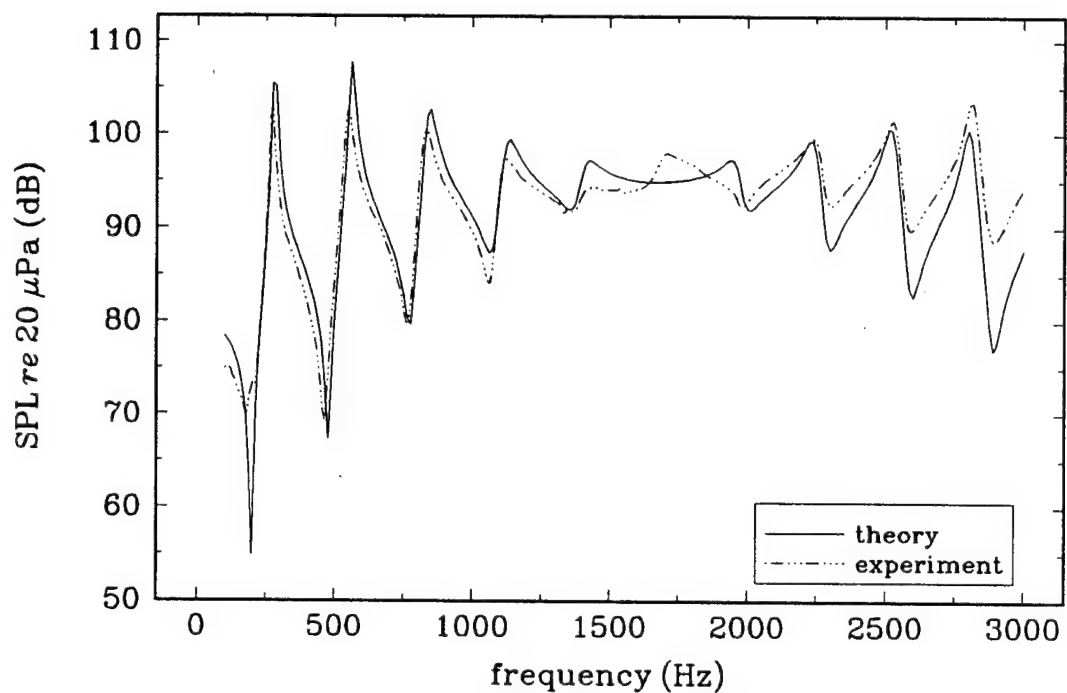


Figure 3.35: Comparison of predicted to measured values of the sound pressure level inside the acoustitron for  $\Omega/\Omega_0 = 1.20$ .

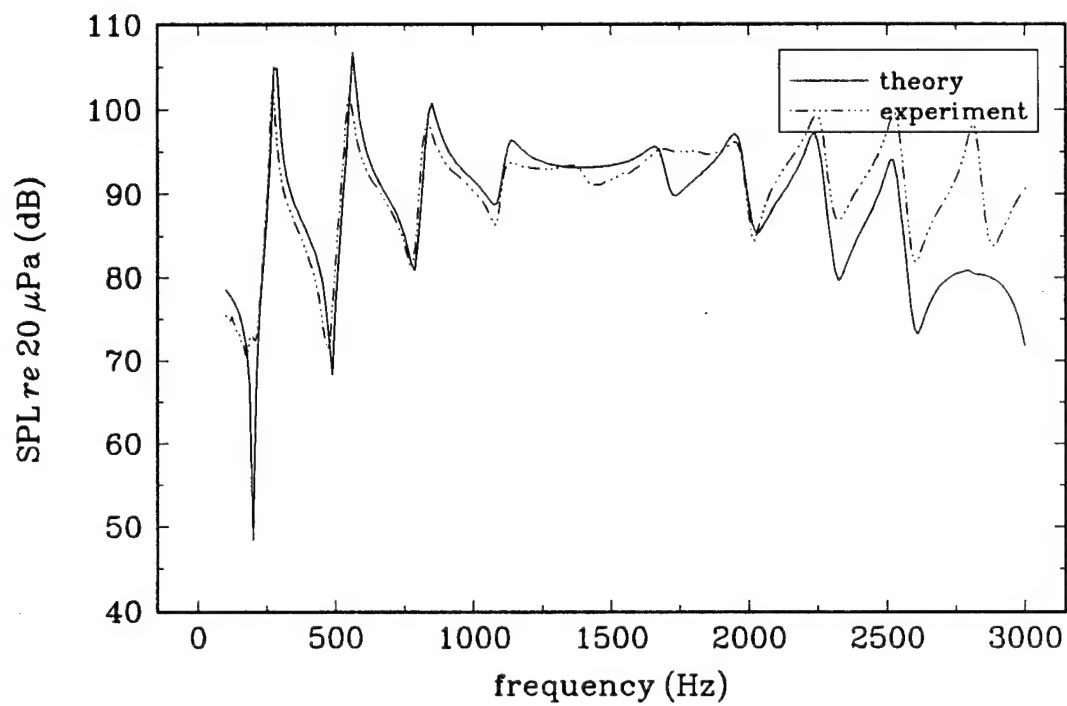


Figure 3.36: Comparison of predicted to measured values of the sound pressure level inside the acoustitron for  $\Omega/\Omega_0 = 1.25$ .

Table 3.4: Frequencies at which there are only three elements per wavelength in the acoustitron for a given value of  $\Omega/\Omega_0$ .

Angular Phase Velocity	Frequency
0.75	2240 Hz
0.80	2390 Hz
0.85	2540 Hz
0.90	2690 Hz
0.95	2840 Hz
1.00	2990 Hz

### 3.3.5 Traveling Waves in the Acoustitron

The theoretical solution for the sound pressure in a toroid with driven walls shows that if the ratio of the angular phase velocity  $\Omega$  and the angular frequency  $\omega$  of the driven wall is an integer, the resulting sound wave will be a traveling wave. This is equivalent to saying that there are an integral number of wavelengths along the circumference of the toroid. In a traveling wave, (1) the amplitude of the sound wave is independent of position and (2) the phase shift measured between two locations in the tube corresponds to the propagation time between them. The requirement for such a situation is given by Eq. (2.58) which says that  $\omega/\Omega$  must be an integer.

There are two straightforward methods for experimentally finding combinations of  $\omega$  and  $\Omega$  that yield traveling waves in the acoustitron. One method is to record the complex pressure at two different positions in the acoustitron at a given frequency as a function of angular phase velocity. The traveling waves can then be determined by looking for values of  $\Omega/\Omega_0$  that produce identical amplitudes and a phase difference equal to the propagation time for the speed of the wave in the wall. An example of such a measurement is shown in Fig. 3.37 which consists of the theoretical complex

pressure at two different positions inside the acoustitron. These plots were generated using Eq. (2.57).

A second method of detecting traveling waves is to record the frequency dependence of the magnitude of the pressure at different positions in the acoustitron for a given angular phase velocity. The traveling waves can then be determined by looking for values of frequency that produce identical amplitudes at all positions. As shown in Fig. 3.37, it is possible to match pressure amplitudes at two different positions, yet not have a traveling wave. By taking measurements at unevenly spaced angular positions, the need to check for the proper phase is eliminated. An example of such a measurement has already been shown in Fig. 2.9, which consists of the theoretical magnitude of the pressure at four different positions inside the acoustitron.

Both of these methods are suitable for making the desired measurements. In practice, however, it is easier to sweep frequencies than to sweep angular phase velocities.

The signal analyzer operating in swept sine mode was again used to record the output of the microphone as a function of frequency. In order to make measurements at different positions inside the acoustitron, the element designated as the first in the output sequence was varied, effectively "moving" the microphone around the tube. An example of the sound pressure in the acoustitron for various microphone positions is shown in Fig. 3.38.

Experimentally determined combinations of  $\Omega$  and  $w$  that produced traveling wave in the acoustitron are shown in Fig. 3.39. (Error bars are about the size of the symbols used in the plot.) Theoretical values determined from  $\Omega = \omega n$ , where  $n$  is an integer, are indicated by the solid lines.

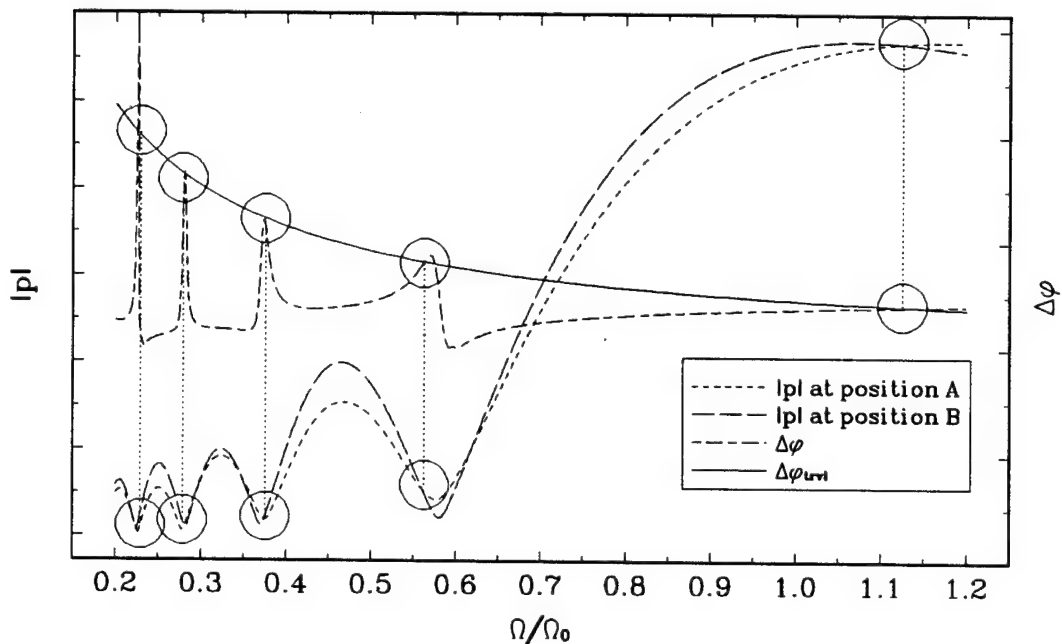


Figure 3.37: Theoretical comparison of the complex pressure at two arbitrary positions (labeled A and B) inside the acoustitron. The graph shows the magnitude  $|p|$  and the phase difference  $\Delta\varphi_{trvl}$  of the pressure at both positions as functions of angular phase velocity. The line labeled as  $\Delta\varphi_{trvl}$  is the phase difference corresponding to the propagation time determined by  $\Omega$ . The values of  $\Omega/\Omega_0$  that yield traveling waves are indicated by circles.

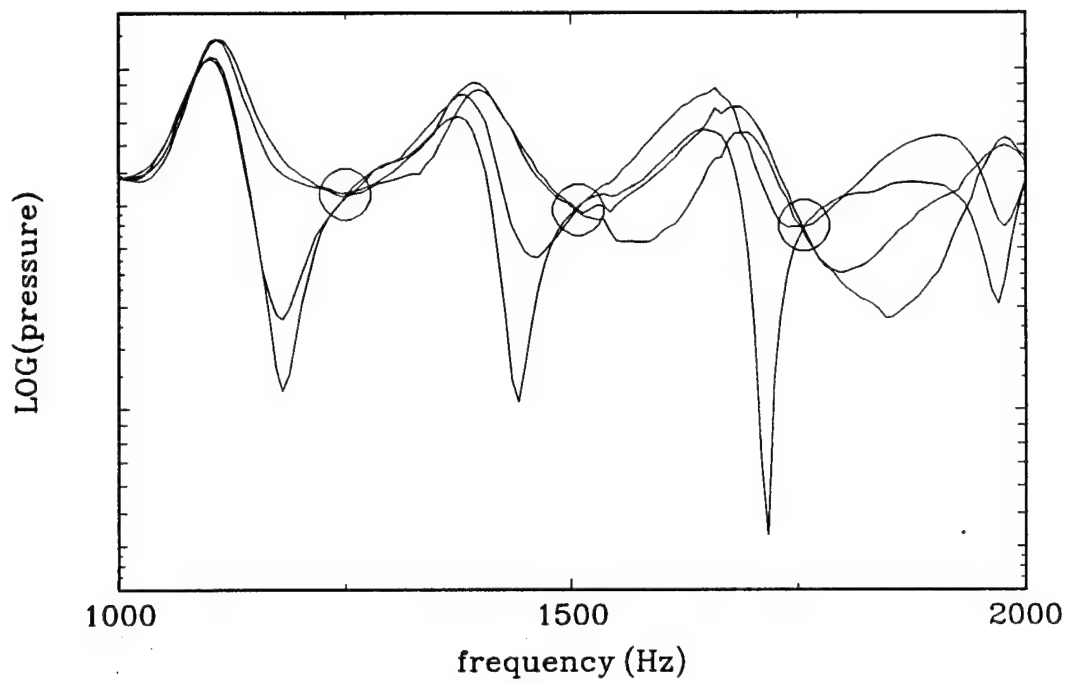


Figure 3.38: Experimental values of the magnitude of the pressure at four different positions inside the acoustitron. The frequencies that yield traveling waves are indicated by circles, where  $\Omega/\Omega_0 = 0.9$ .

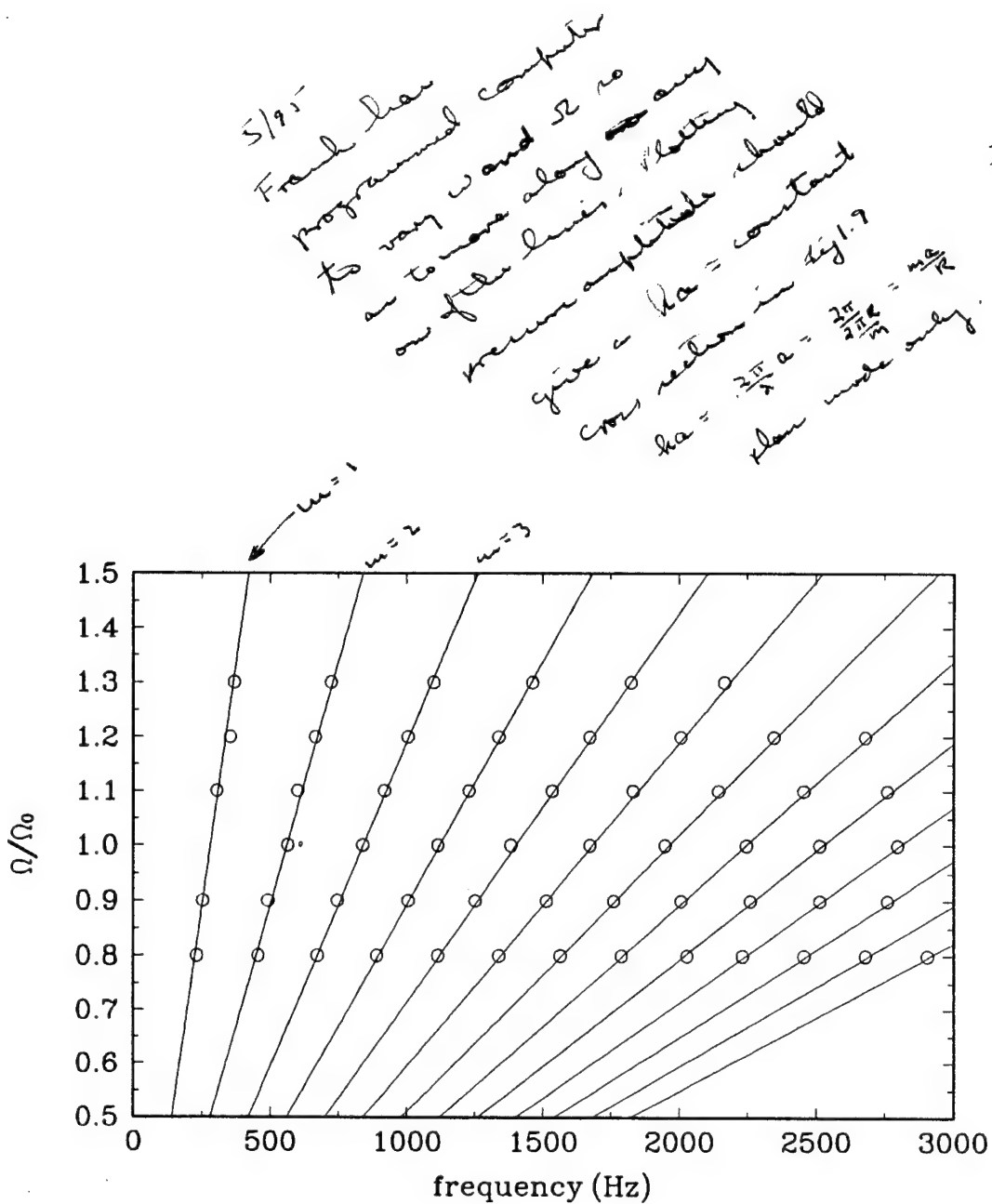


Figure 3.39: Comparison of theoretical (solid lines) and experimental (empty circles) results for combinations of frequency and angular phase velocity that yield traveling waves in the acoustitron.

# Chapter 4

## Conclusions

### 4.0.6 Summary

The solution for sound propagation in cylindrical straight tubes and toroidal waveguides for the case of a driven wall has been presented. For the cylindrical straight tube, the effects of the viscosity and thermal conductivity of the fluid medium on the propagation of sound were considered. The following results were obtained:

- When the lossless fluid filled tube is driven with a combination of frequency and wave number that corresponds to a mode of propagation in a tube with rigid walls, the amplitude of the particle velocity is infinite. For the case of the air filled tube, the velocity amplitude is no longer infinite, just very large compared to the driving amplitude.
- When the viscous and thermally conducting fluid filled tube is driven with a wall speed corresponding to the intrinsic speed of sound in the medium ( $c_w = c$ ), the radial velocity amplitude of the acoustic mode is zero, while for the lossless

fluid filled tube it is proportional to  $r/a$ .

Also presented was the solution for sound propagation in a toroidal waveguide with the following boundary at the wall: (1) rigid walls, (2) rigid walls except for a single driving element in the wall, and (3) driven walls with a given wave number and angular phase velocity. The following results were obtained:

- In the low frequency limit, the characteristic frequencies of the rigid wall toroid correspond to wavelengths that fit with an integral length along the circumference. This means that the curvature of the waveguide will not affect the sound propagating in the tube.
- For the case of a tube with a single driving element driven at a characteristic frequency of the rigid toroid, the result is a standing wave of infinite amplitude.
- For the case of driven walls with a given wave number and angular phase velocity:
  - When the driving frequency is that of a characteristic frequency of the rigid toroid, the response of the system is infinite (lossless case).
  - When the ratio of the angular phase velocity and the angular frequency is an integer value, the result is a traveling wave inside the toroid.

The results of experiments performed indicate that sound propagation in a toroid with driven walls is well understood in terms of the theory presented.

In order to include losses in the solution of sound in a toroid with driven walls, a theoretical value for the attenuation due to compliant tube walls was presented.

Theory indicated the presence of a resonant frequency corresponding to the material properties of the tube wall. Measurements were made verifying this behavior in the toroid.

#### 4.0.7 Extensions of this Work

An acoustitron is currently under construction that consists of a square channel cut into an acrylic block to form a square waveguide. Piezoceramic disks will be mounted in the bottom of the groove and in the plate that forms the top. An advantage of this design over that used in this paper is that the absorption of sound will be less because of the rigid walls between the driving elements. The purpose of this device is to allow measurements to be made in liquids. It can also be modified by the addition of vertical plates along the inside circumference to form a *stack* for a traveling wave thermoacoustic engine. In thermoacoustics, it is desirable to place the stack at a position where the pressure and velocity are large, as well as out of phase by  $\pi/2$  radians. In an acoustitron containing a traveling wave, the pressure and velocity meet this condition at all points along the circumference. This would allow a thermoacoustic effect to be produced along the entire toroid, as opposed to a single position in a standing wave tube.

The following is a list of possible extensions to this work:

- Consideration of nonlinear effects present for large driving amplitudes, such as finite amplitude sound and acoustic streaming.
- Use of the acoustitron to measure the bulk speed of sound in a liquid or sediment.

## **BIBLIOGRAPHY**

# Bibliography

- [1] G. Kirchhoff, Ann. Phys. Chem. **134**, 177 (1868).
- [2] F. D. Shields and R. T. Lagemann, J. Acoust. Soc. Am. **29**, 470 (1957).
- [3] J. W. Strutt (Lord Rayleigh), *The Theory of Sound*, 2nd ed. (Dover Publications, New York, 1945).
- [4] D. E. Weston, Proc. Roy. Soc. **B66**, 695 (1953).
- [5] H. Tijdeman, J. Sound Vib. **39**, 1 (1975).
- [6] M. J. Anderson, Ph.D. thesis, Washington State University, 1989.
- [7] W. J. Jacobi, J. Acoust. Soc. Am. **21**, 120 (1949).
- [8] T. C. Lin and G. W. Morgan, J. Acoust. Soc. Am. **28**, 1165 (1956).
- [9] M. El-Raheb, J. Acoust. Soc. Am. **71**, 296 (1982).
- [10] M. El-Raheb, J. Acoust. Soc. Am. **71**, 307 (1982).
- [11] R. D. Fay, J. Acoust. Soc. Am. **24**, 459 (1952).

- [12] V. A. Del Grosso, Report 6852, Naval Research Laboratory, Washington, D.C. (unpublished).
- [13] R. Kumar, *Acustica* **27**, 317 (1972).
- [14] T. H. Ruppel, Ph.D. thesis, The University of Mississippi, 1992.
- [15] P. M. Morse, *Vibration and Sound* (American Institute of Physics, Woodbury, New York, 1981).
- [16] L. L. Beranek, *J. Acoust. Soc. Am.* **12**, 228 (1940).
- [17] R. A. Scott, *Proc. Phys. Soc.* **58**, 350 (1946).
- [18] A. Bokor, *J. Sound Vib.* **10**, 390 (1969).
- [19] A. S. Hersh and I. Catton, *J. Acoust. Soc. Am.* **50**, 992 (1971).
- [20] U. J. Kurze and C. H. Allen, *J. Acoust. Soc. Am.* **49**, 1643 (1971).
- [21] D. H. Tack and R. F. Lambert, *J. Acoust. Soc. Am.* **38**, 655 (1965).
- [22] S. D. Savkar, *J. Sound Vib.* **19**, 355 (1971).
- [23] C. T. Molloy and E. Honigman, *J. Acoust. Soc. Am.* **16**, 267 (1945).
- [24] S. H. Ko, *J. Sound Vib.* **22**, 193 (1972).
- [25] P. E. Doak and P. G. Vaidya, *J. Sound Vib.* **12**, 201 (1970).
- [26] P. Harel and M. Perulli, *J. Sound Vib.* **15**, 455 (1971).
- [27] L. J. Sivian, *J. Acoust. Soc. Am.* **9**, 135 (1937).

- [28] W. Eversman, J. Acoust. Soc. Am. **49**, 1372 (1971).
- [29] W. C. Osborne, J. Sound Vib. **45**, 39 (1976).
- [30] M. El-Raheb, J. Acoust. Soc. Am. **67**, 1924 (1980).
- [31] W. Rostafinski, J. Acoust. Soc. Am. **52**, 1411 (1972).
- [32] W. Rostafinski, J. Acoust. Soc. Am. **56**, 11 (1974).
- [33] F. E. Grigor'yan, Sov. Phys.-Acoust. **14**, 315 (1969).
- [34] F. E. Grigor'yan, Sov. Phys.-Acoust. **16**, 192 (1970).
- [35] S. H. Ko and L. T. Ho, J. Sound Vib. **53**, 189 (1977).
- [36] A. Cummings, J. Sound Vib. **35**, 451 (1974).
- [37] M. El-Raheb and P. Wagner, J. Acoust. Soc. Am. **71**, 1335 (1982).
- [38] A. D. Pierce, *Acoustics: An Introduction to Its Physical Principles and Applications* (The Acoustical Society of America, Woodbury, New York, 1989).
- [39] R. Raspot, (Lecture presentation on October 9, 1992) (unpublished).
- [40] P. E. Krasnushkin, Uch. Zap. Mosk. Gos. Univ., No. 75, Bk. 2, Pt. 2, 9 (1945).
- [41] G. N. Watson, *A Treatise on The Theory of Bessel Functions* (University Press, Cambridge, 1962).
- [42] L. E. Kinsler and A. R. Frey, *Fundamentals of Acoustics*, 2nd ed. (John Wiley and Sons, New York, 1962).

- [43] W. P. Arnott, H. E. Bass, and R. Raspet, *J. Acoust. Soc. Am.* **90**, 3228 (1991).
- [44] M. R. Stinson, *J. Acoust. Soc. Am.* **89**, 550 (1991).
- [45] *Guide to Modern Piezoelectric Ceramics*, Morgan Matroc, Inc., Electro Ceramics Division, Bedford, Ohio.
- [46] L. E. Reichl, *A Modern Course in Statistical Physics* (University of Texas Press, Austin, Texas, 1980).

## **APPENDIX**

# Appendix A

## Useful Relations of State Variables

(The following is taken from Reichl [46].) Variables that specify a thermodynamic state are referred to as *state variables*. Examples of some state variables are  $\rho$  (density),  $p$  (pressure),  $T$  (temperature), and  $s$  (entropy). In general, given a function  $F = F(x_1, x_2)$ , the differential of this function is defined as

$$dF = \left( \frac{\partial F}{\partial x_1} \right)_{x_2} dx_1 + \left( \frac{\partial F}{\partial x_2} \right)_{x_1} dx_x, \quad (\text{A.1})$$

which is sometimes referred to as the *chain rule*. If  $F$  is analytic and

$$\left[ \frac{\partial}{\partial x_1} \left( \frac{\partial F}{\partial x_2} \right)_{x_1} \right]_{x_2} = \left[ \frac{\partial}{\partial x_2} \left( \frac{\partial F}{\partial x_1} \right)_{x_2} \right]_{x_1}, \quad (\text{A.2})$$

then  $dF$  is an exact differential. Differentials of all state variables are exact.

Given four state variables  $w$ ,  $x$ ,  $y$ , and  $z$ , such that  $F(x, y, z) = 0$  and  $w$  is a function of any two of the variables  $x$ ,  $y$ ,  $z$ , using the properties given above one can

obtain the following relations:

$$\left( \frac{\partial x}{\partial y} \right)_z = \frac{1}{\left( \frac{\partial y}{\partial x} \right)_z}, \quad (\text{A.3})$$

$$\left( \frac{\partial x}{\partial y} \right)_z \left( \frac{\partial y}{\partial z} \right)_x \left( \frac{\partial z}{\partial x} \right)_y = -1, \quad (\text{A.4})$$

$$\left( \frac{\partial x}{\partial w} \right)_z = \left( \frac{\partial x}{\partial y} \right)_z \left( \frac{\partial y}{\partial w} \right)_z, \quad (\text{A.5})$$

$$\left( \frac{\partial x}{\partial y} \right)_z = \left( \frac{\partial x}{\partial y} \right)_w + \left( \frac{\partial x}{\partial w} \right)_y \left( \frac{\partial w}{\partial y} \right)_z. \quad (\text{A.6})$$

These relations are used in Section 1.3

## Appendix B

### Digital Delay Circuit Diagrams

Analog signals used to drive the acoustitron are passed through the analog-to-digital converter shown in Fig. B.1 which takes the digital equivalent of the analog signal and feeds it into the digital signal processor. The main circuit shown in Fig. B.2 contains the interface between the digital signal processor and the thirty-two digital-to-analog converters (labeled DBDAC). Figure B.3 is a single channel of digital-to-analog output. The voltage range for each channel of output is 5 volts peak with a resolution of approximately  $2 \times 10^{-2}$  volts (corresponding to 1 LSB). The sample frequency of the circuit is approximately 30 kHz. Each output is passed through an amplifier, designed for the specific capacitance of the piezoceramic drivers, shown in Fig. B.4. The net gain of this circuit is  $\times 10$ , yielding a maximum driving signal of 50 volts peak (17.7 volts rms).

**Figure B.1:** Analog-to-digital circuit.

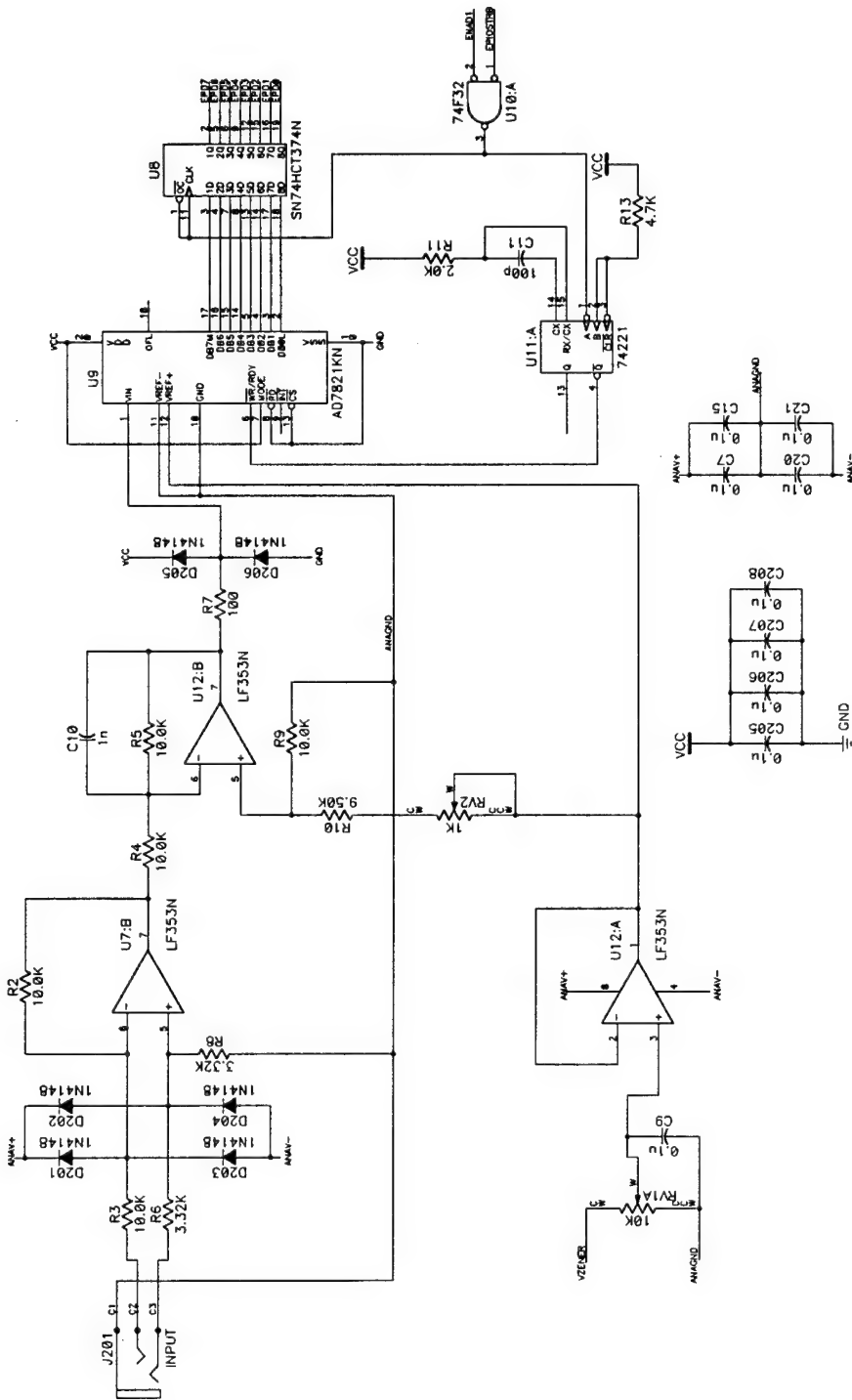


Figure B.2: Main circuit.

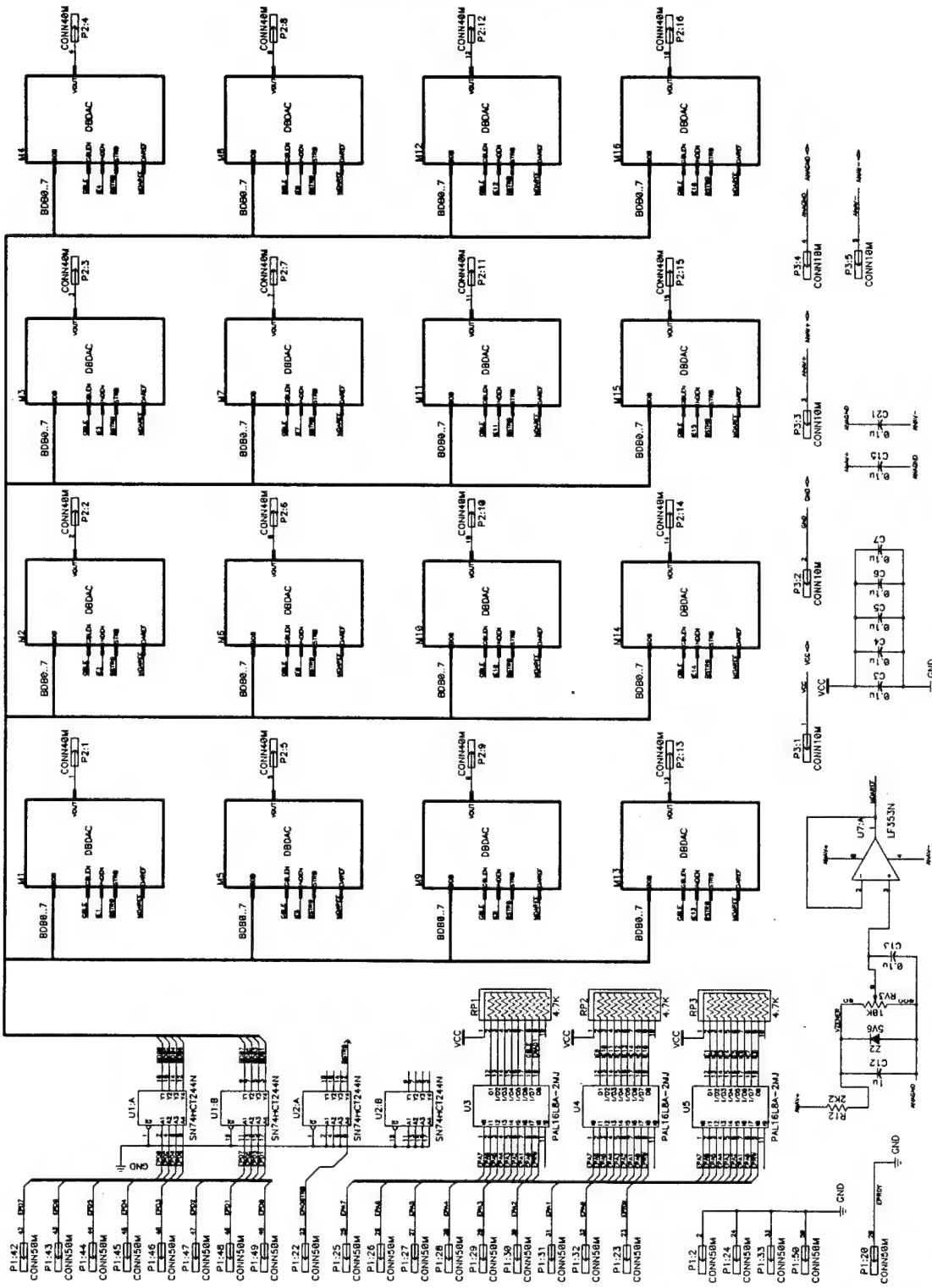
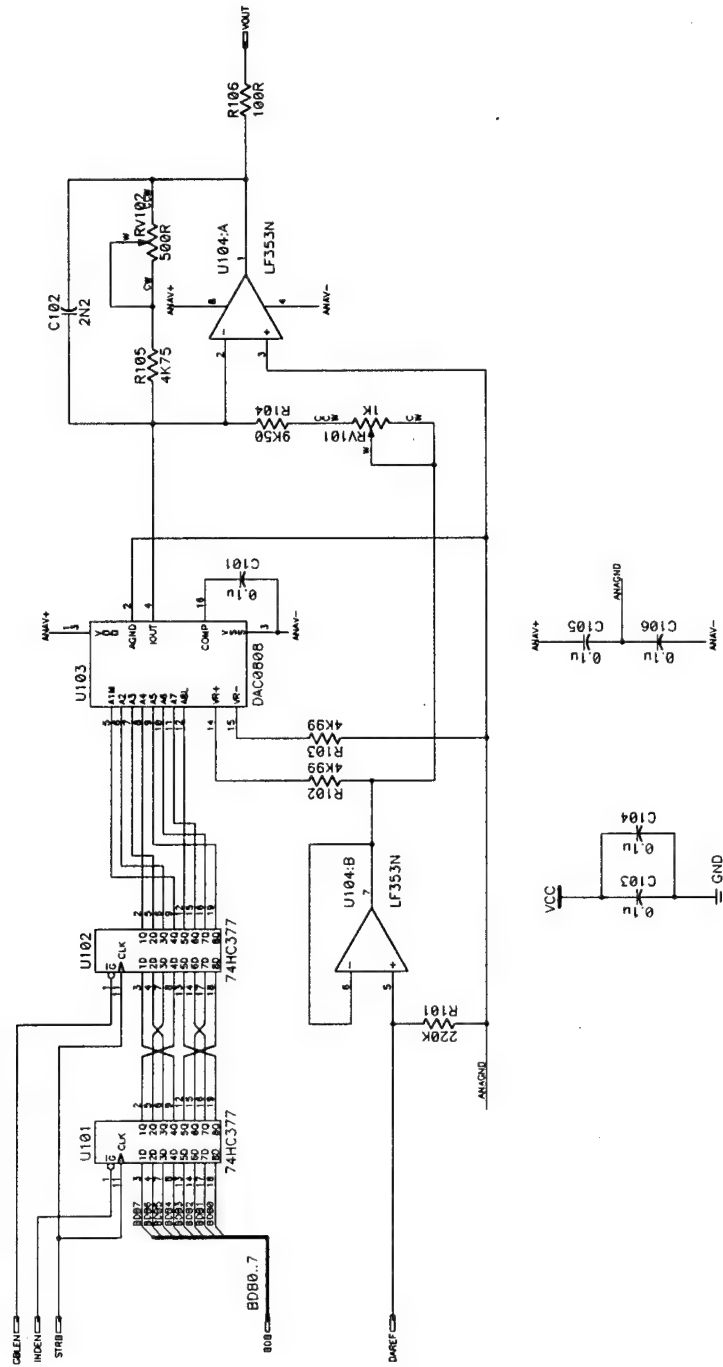


Figure B.3: Digital-to-analog circuit.



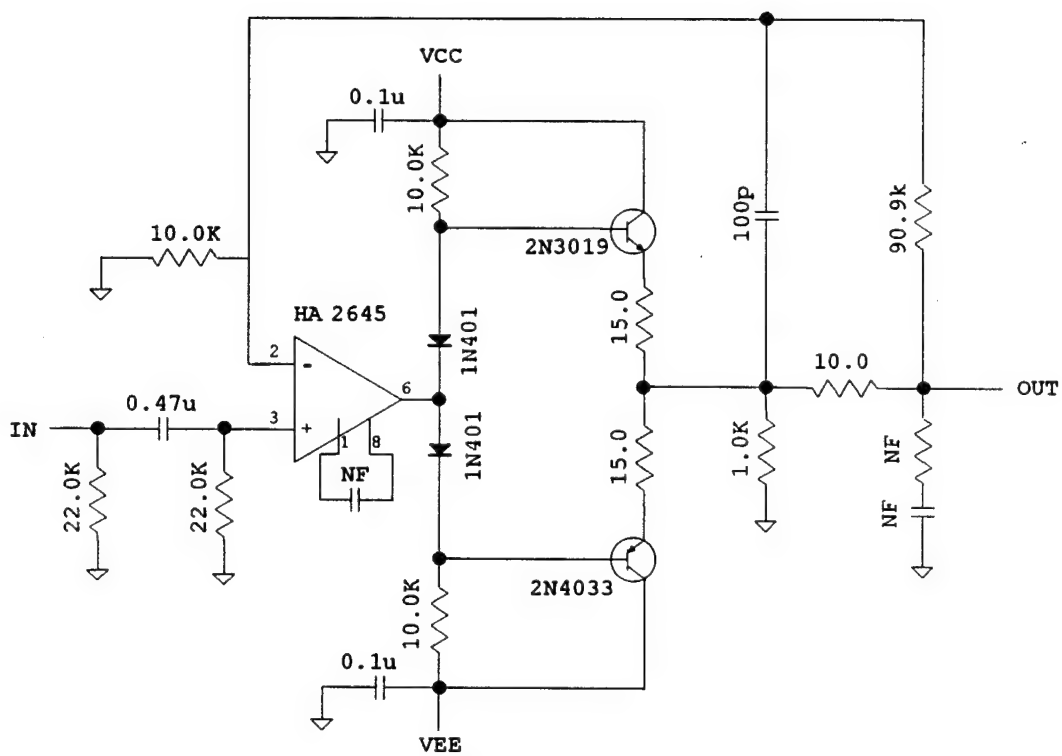


Figure B.4: Amplifier circuit.

## **Appendix C**

### **Software and Hardware Information**

All computer work done for this dissertation, was done with an IBM-PC compatible 486-DX computer. Information about specific tasks performed are as follows:

- The Texas Instruments TMS320C30 Digital Signal Processor used in the digital delay circuit was located on a Sonitech International Inc. SPIRIT-30 card plugged into a 16-bit slot located inside the computer.
- Theoretical plots shown in this work were calculated using FORTRAN 77 code compiled by a Lahey Computer Systems, Inc. compiler. Calculations of the Bessel and Neumann functions were carried out using library subroutines written by Donald E. Amos, of Sandia National Laboratories, available via anonymous FTP from the INTERNET.
- All plots were generated using Axum<sup>®</sup>.

- The solution for the roots of Eq. (2.10), as well as the linear curve fits to determine  $m$  in Eq. (3.6), were done using Mathcad<sup>®</sup> PLUS 5.0.
- This document was produced by TeX using the LATEX macro package.
- All graphics were produced using Aldus<sup>®</sup> IntelliDraw.

## Vita

Christopher Charles Lawrenson was born on May 22, 1968, the first of two children of C.E. (Buddy) and Jeannie Lawrenson. After moving from place to place, including Florida, Texas, and Cape Town, South Africa, he ended up in Martinsburg, Indiana. He attended Eastern High School in the nearby town of Pekin. He graduated in 1986 receiving the Most Promising Student in Science award. That same year, he started his undergraduate work at Harding University in Searcy, Arkansas. It was there that he met and married the former Leigh Traisci. After completing his degree in Physics, he enrolled in graduate school at the University of Mississippi, under the tutelage of Dr. F. Douglas Shields. While at Ole Miss, he worked at the National Center for Physical Acoustics as a Graduate Research Assistant. He was fortunate to receive an EPSCoR grant from the Office of Naval Research, which funded his research. During this time he became affiliated with the Mississippi Academy of Sciences (MAS), and the Acoustical Society of America (ASA). He was awarded best student paper in Physics and Engineering at the 1991 meeting of the MAS, and best student paper in Engineering Acoustics at the 127th meeting of the ASA in 1994. In the summer of 1994, he received an ASA fellowship to attend the Physical Acoustics Summer School in Monterey, California. He received his Ph.D. in Physics in December of 1994. His

present address is Rt. 6, Box 246, Oxford, Mississippi, 38655.